Silje Kjærnes Øen

PET/MRI – Towards clinical use in the brain

NTNU
Norwegian University of
Science and Technology

Silje Kjærnes Øen

PET/MRI – Towards clinical use in the brain

Thesis for the Degree of Philosophiae Doctor

Trondheim, September 2022

Norwegian University of Science and Technology
Faculty of Medicine and Health Sciences
Department of Circulation and Medical Imaging

Norsk sammendrag

Det første positronemisjonstomografi (PET)/magnetisk resonans (MR) systemet i Norge ble installert på St. Olavs Hospital i Trondheim i 2013 og var en generøs gave fra Trond Mohn. Denne avbildningsmodaliteten muliggjør simultan PET- og MR-avbildning og gir dermed både metabolsk og anatomisk informasjon i en og samme undersøkelse. PET er en mye brukt bildemodalitet innen onkologi, men brukes også stadig mer innen nevrologi og kardiologi. De første kliniske PET/MR systemene ble introdusert i 2010 og var et spennende tilskudd til PET/computed tomograohy (CT) som ble lansert i 2001. MR-bilder gir en utmerket bløtvevskontrast og benyttes ofte fremfor CT i kroppsregioner hvor dette er spesielt viktig, som i hjernen. Når PET/MR ble lansert var det fremdeles ikke klart hvilke bruksområder denne modaliteten var spesielt egnet for. I tillegg førte unøyaktig MR-basert attenuasjonskorreksjon (MRAC) av PET-bildene til at denne modaliteten ikke ble brukt i klinisk praksis. Hensikten med arbeidet knyttet til denne avhandlingen var derfor å vurdere PET-bildekvaliteten for PET/MR sammenlignet med PET/CT og hvorvidt modaliteten kan brukes ved kliniske hjerneundersøkelser.

Først ble klinisk tilgjengelige og forsknings MRAC-metoder evaluert og sammenlignet med CT-basert AC. Dette ble gjort for [18F]FDG PET-undersøkelser av pasienter med mistanke om demens, en undersøkelse som i økende grad brukes i tillegg til MR i denne pasientgruppen. Resultatene viste at nøyaktigheten for en nylig implementert klinisk MRAC metode var akseptabel, men at forskningsmetoder ga økt nøyaktighet.

Videre ble PET-bildekvaliteten for PET/MR vurdert basert på kontrast og deteksjon av små lesjoner. Dette ble utført som en fantomstudie representativ for hjerneundersøkelser. Kontrasten og detekterbarheten var noe redusert for PET/MR sammenlignet med PET/CT, men tilsvarende detekterbarhet ble oppnådd med økt innsamlingstid for PET/MR.

Resultatene i de to første studiene viste at PET/MR kan brukes ved kliniske hjerneundersøkelser, som f.eks. ved demens. Potensialet til PET og PET/MR innen nevrodegenerative sykdommer øker med ny forskning og utvikling av nye tracere. Innen nevroonkologi har det blitt utført mye forskning på gliom, og aminosyre PET anbefales nå for å komplementere MR for denne pasientgruppen. Mindre forskning har blitt utført for hjernemetastaser og den diagnostiske verdien av aminosyre PET har ikke blitt avklart. I den siste studien ble det derfor undersøkt hvorvidt en lovende aminosyretracer ([18F]FACBC) ville

gi diagnostisk verdi utover en MR-undersøkelse av hjernemetastaser. Hjernemetastasene viste generelt høyt opptak av [18F]FACBC sammenlignet med friskt vev i hjernen, men [18F]FACBC PET var ikke i stand til å detektere små hjernemetastaser i samme grad som MR. [18F]FACBC PET viste dog tendens til å avdekke tumorvev utenfor området definert med MR. Det ble også undersøkt hvorvidt [18F]FACBC PET kan skille mellom tilbakefall av tumorvev og skader fra strålebehandling, noe som er utfordrende med MR, men det kreves mer forskning for å bestemme den diagnostiske verdien av [18F]FACBC PET ved denne problemstillingen.

Dette forskningsarbeidet er et viktig skritt for videre forskning på potensialet og bruksområdene for PET/MR i hjernen. I tillegg har denne forskningen ført til at PET/MR nå brukes klinisk ved undersøkelser av pasienter med demens ved St. Olavs Hospital.

Kandidat: Silje Kjærnes Øen

Institutt: Institutt for sirkulasjon og bildediagnostikk, NTNU

Hovedveileder: Live Eikenes, Professor, NTNU

Biveileder: Anna Karlberg, PhD, NTNU/St. Olavs Hospital

Acknowledgements

Table of Contents

English summary

The first positron emission tomography (PET)/magnetic resonance imaging (MRI) system in Norway was installed at St. Olavs Hospital in Trondheim in 2013 as a generous gift from Trond Mohn. This hybrid imaging modality enables simultaneous PET and MRI examinations, providing metabolic and anatomic images in one examination. PET is widely used in oncology, but also increasingly applied in neurology and cardiology. The first clinical PET/MRI systems were introduced in 2010 and this was an exciting extension to PET/computed tomography (CT) systems available from 2001. MRI provides excellent soft tissue contrast and is preferred over CT in body regions where this is of high importance, like the brain. However, no key applications for the system were announced and PET/MRI was hampered by inaccurate MR-based attenuation correction (MRAC) of PET images. Consequently, the system was not used in clinical routine. The aim of this thesis was therefore to evaluate the PET image quality of PET/MRI compared to PET/CT and whether PET/MRI is applicable for clinical brain examinations.

First, clinically available and research MRAC methods were evaluated and compared to CT-based AC. This was done for [^{18}F]FDG PET evaluations of patients with suspected dementia, examinations that is increasingly used to support MRI for this patient group. The results showed that the accuracy of a recently implemented clinically MRAC method was acceptable, but the performance was further improved with research MRAC methods.

Subsequently, the PET image quality of the PET/MRI system was evaluated in terms of contrast and detectability of small lesions in a phantom study representative for brain imaging. The contrast and detectability were slightly decreased for PET/MRI compared to PET/CT, but the same detectability was obtained for an increased acquisition time for PET/MRI.

The results of the two first papers showed that PET/MRI is applicable for brain examinations in clinical routine, like dementia. The potential of PET and hence PET/MRI in neurodegenerative diseases is increasing with recent research and tracer development. In neuro-oncology, a lot of research has been done on glioma and amino acid PET is now recommended to complement MRI for this patient group. For brain metastasis, the literature is still limited, and the diagnostic value of amino acid PET is not yet clear. The last study was therefore conducted to assess whether a promising amino acid PET tracer ([^{18}F]FACBC) would add diagnostic value to MRI in evaluation of brain metastases. The brain metastases showed in general high [^{18}F]FACBC uptake compared to normal brain tissue, but detection of small

metastases was limited and inferior to MRI. However, [^{18}F]FACBC PET might detect tumor tissue beyond the tumor volume defined on MRI. The potential for [^{18}F]FACBC PET to differentiation tumor recurrence from radiation-related changes was also investigated, which may be challenging based on MRI, but further studies are required to determine the diagnostic value of [^{18}F]FACBC PET in this situation.

The work of this thesis is an important step to further investigations of the potential and applications of brain PET/MRI. Furthermore, PET/MRI is now used in clinical routine for examination of patients with dementia at St. Olavs Hospital based on the results of this thesis.

List of abbreviations

^{68}Ga	Gallium-68
^{68}Ge	Germanium-68
^{18}F	Fluorine-18
^{177}Lu	Lutetium-177
[^{11}C]MET	L-[methyl-carbon-11]-methionine
[^{11}C]PiB	[Carbon-11]-labelled Pittsburgh Compound-B
[^{18}F]FACBC	Anti-1-amino-3-[fluorine-18]fluorocyclobutane-L-carboxylic acid
[^{18}F]FDG	2-deoxy-2-[fluorine-18]fluoro-D-glucose
[^{18}F]FDOPA	L-3,4-dihydroxy-6-[fluorine-18]fluorophenylalanine
[^{18}F]FET	O-(2-[fluorine-18]Fluoroethyl)-L-tyrosine
[^{68}Ga]PSMA	[Gallium-68]-prostate-specific membrane antigen
[^{177}Lu]PSMA	[Lutetium-177]-prostate-specific membrane antigen
AA	Amino acid
AC	Attenuation correction
ACF	Attenuation correction factor
AD	Alzheimer's disease
ALARA	As Low As Reasonably Achievable
aMRI	Advanced MRI
APD	Avalanche photodiode
BBB	Blood-brain barrier
BPL	Bayesian penalized likelihood
ce-MRI	Contrast-enhanced MRI
CNR	Contrast-to-noise ratio
CNS	Central nervous system
CRC	Contrast recovery coefficient
CT	Computed tomography
CTAC	CT-based attenuation correction
DLB	Dementia with Lewy bodies
DSC	Dice similarity coefficient
DWI	Diffusion-weighted imaging
EANM	European Association of Nuclear Medicine
EANO	European Association for Neuro-Oncology

FBP	Filtered backprojection
FID	Free induction decay
FLAIR	Fluid attenuated inversion recovery
fMRI	Functional MRI
FOV	Field of view
FTD	Frontotemporal dementia
FWHM	Full width at half-maximum
GE	General Electric
LAC	Linear attenuation coefficient
LAT	L-amino acid transporters
LOR	Line of response
LSO	Lutetium oxyorthosilicate
LYSO	Lutetium-yttrium oxyorthosilicate
MCI	Mild cognitive impairment
MRAC	MR-based attenuation correction
MRI	Magnetic resonance imaging
MRS	Magnetic resonance spectroscopy
NEMA	National Electrical Manufacturers Association
NMV	Net magnetization vector
OSEM	Ordered Subset Expectation Maximization
PD	Parkinson's disease
PET	Positron emission tomography
PET-RANO	Response Assessment in Neuro-Oncology with PET
PMT	Photomultiplier tube
PSF	Point spread function
PSMA	Prostate-specific membrane antigen
PVE	Partial volume effects
PWI	Perfusion-weighted imaging
RD	Relative difference
REC	Regional Committee for Ethics in Medical Research
RF	Radiofrequency
ROI	Region of interest
SiPM	Silicon photomultiplier
SNR	Signal-to-noise ratio

SUV	Standardized uptake value
TAC	Time activity curve
TB	Total body
TBR	Tumor-to-background ratio
TE	Echo time
TOF	Time-of-flight
TR	Repetition time
UCL	University College London
UTE	Ultrashort echo-time
VOI	Volume of interest
ZTE	Zero-echo time

List of publications

Paper I

Øen SK, Keil TM, Berntsen EM, Aanerud JF, Schwarzlmüller T, Ladefoged CN, Karlberg AM, Eikenes L. «*Quantitative and clinical impact of MRI-based attenuation correction methods in [^{18}F]FDG evaluation of dementia.*» European Journal of Nuclear Medicine & Molecular Imaging Research. 2019 Aug 24;9(1):83.

Paper II

Øen SK, Aasheim LB, Eikenes L, Karlberg AM. «*Image quality and detectability in Siemens Biograph PET/MRI and PET/CT systems-a phantom study.*» European Journal of Nuclear Medicine & Molecular Imaging Physics. 2019 Aug 5;6(1):16.

Paper III

Øen SK, Johannessen K, Pedersen LK, Berntsen EM, Totland JA, Johansen H, Bogsrud T, Solheim TS, Karlberg A, Eikenes L. «*Diagnostic value of [^{18}F]FACBC PET/MRI in brain metastases.*» Submitted to Clinical Nuclear Medicine, May 2022.

Other publications

Kuttner S, Lassen ML, **Øen SK**, Sundset R, Beyer T, Eikenes L. «*Quantitative PET/MR imaging of lung cancer in the presence of artifacts in the MR-based attenuation correction maps*.» Acta Radiologica. 2020 Jan;61(1):11-20.

Ladefoged CN, Hansen AE, Henriksen OM, Bruun FJ, Eikenes L, **Øen SK**, Karlberg A, Højgaard L, Law I, Andersen FL. «*AI-driven attenuation correction for brain PET/MRI: Clinical evaluation of a dementia cohort and importance of the training group size.*» Neuroimage. 2020 Nov 15;222:117221.

Hansen S, Kuttner S, Kampffmeyer M, Markussen TV, Sundset R, **Øen SK**, Eikenes L, Jenssen R. «*Unsupervised supervoxel-based lung tumor segmentation across patient scans in hybrid PET/MRI*» Expert Systems with Applications. 2021 April, 167:114244.

1 Introduction

Positron emission tomography (PET) is a nuclear imaging technique representing molecular processes and the first commercial PET scanner was introduced in 1976 (1). In 2001, the first hybrid PET/computed tomography (CT) system was introduced and successfully spread around the world (2). Standalone PET systems were replaced by PET/CT, and by 2016 more than 5000 hybrid systems had been installed worldwide (3, 4). This hybrid imaging technology provided functional and anatomical information from PET and CT, respectively, in a single examination and decreased the PET imaging time. PET/CT is now well-established in the clinical routine for oncological applications, and is increasingly used within other fields, such as neurology and cardiology.

Magnetic resonance imaging (MRI) provides superior soft tissue contrast compared to CT, and the combination of PET and MRI in a hybrid system was already discussed in the early 1990s (5). However, the interference between the magnetic field and PET detectors required major technological advancements and clinical whole-body PET/MRI systems were not introduced until 2010 (6, 7). Furthermore, quantitative attenuation corrections of the PET images were now based on MR images instead of CT images which caused inaccurate PET images, especially in the brain. In addition to the high cost of the system, this caused limited number of installations of the modality. The clinical benefits for this novel system were still unknown at the time, and users worldwide requested information about clinical key applications. Today, around 200 PET/MRI systems are installed worldwide (4) (Holger Schmidt, personal communication 2022.03.31).

Nevertheless, the first PET/MRI system in Norway was installed at St. Olavs Hospital in Trondheim in 2013 as a generous gift from business leader Trond Mohn. Although this was an exciting system, the knowledge and confidence in the system was not in place and the PET/MRI system was not widely used for clinical applications, neither in Trondheim nor worldwide. Research projects were started to initiate implementation of PET/MRI in clinical routine, also by our research group at the integrated university hospital in Trondheim. As a part of this thesis, the impact of MR-based attenuation correction (MRAC) and the PET image quality of PET/MRI was evaluated and compared to the well-established PET/CT for brain examinations. As MRI is the main imaging modality in neurological and neuro-oncological applications, PET/MRI may play an interesting role in brain diagnostics where PET can add

complementary information to MRI. Therefore, we further investigated the potential of PET/MRI in dementia and brain tumors.

1.1 PET

1.1.1 Positron emission and annihilation

The signal acquired in PET imaging originates from proton-rich radionuclides that decay by positron emission, hence the name positron emission tomography. The positron emitting isotopes are labelled to a pharmaceutical, called tracer, which is injected into the bloodstream of the patient and brings the radioactive molecules to the sites of interest. The most widely used radiopharmaceutical is a glucose analogue (2-deoxy-2-[fluorine-18]fluoro-D-glucose, [^{18}F]FDG), as it guides the [^{18}F]FDG molecules to cancer cells due to their high glucose metabolism. Other tracers can be used to label other molecular processes. In this way, the positrons are emitted from the sites we want to visualize, and the resulting PET image demonstrates the distribution of the tracer.

The emitted positron travels a short distance in tissue, losing its kinetic energy by inelastic interactions with electrons in the tissue (8). When almost at rest the positron combines with an electron and annihilates, a process converting the mass of the positron and electron into electromagnetic energy in the form of two high-energy γ photons, as illustrated in Figure 1. The annihilation photons are emitted in opposite directions ($180° \pm 0.25°$), each with an energy of 511 keV. The PET detectors surrounding the patient can detect these annihilation photons. If both photons from an annihilation is detected within a certain timeframe, the position of the annihilation is known to be along a line between the two detectors involved. The tracer is hence assumed to be located along this line, called the line of response (LOR). This information is used to reconstruct an image of the distribution of the tracer in the body of the patient, which is further described in section 1.1.4.
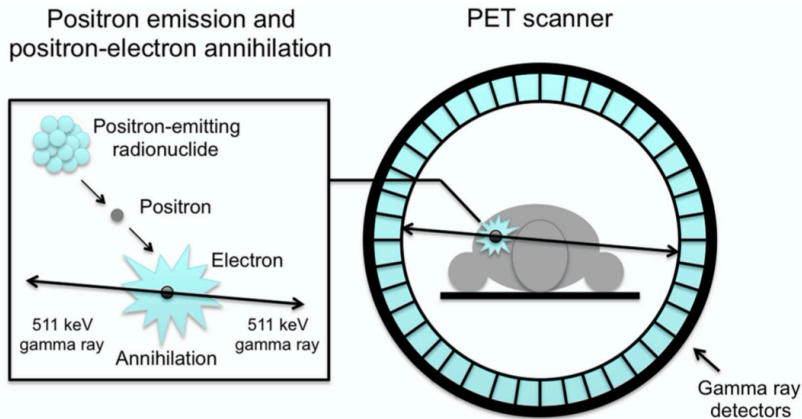
Figure 1 When a positron is emitted from a radionuclide, it travels a short distance in tissue before it interacts with an electron and an annihilation process takes place, where two 511 keV gamma photons are created. The annihilation photons are emitted in opposite directions and may be detected by the PET detectors. Illustration from van der Veldt et al. (9), published under creative commons license CC BY 3.0 (https://creativecommons.org/licenses/by/3.0/).

1.1.2 PET detectors

PET detectors surrounding the patient shall efficiently detect the 511 keV photons that escape the body (8), and provide information about the spatial location and energy of the incoming photons and the time of interaction (10). The PET detectors consist of two components: the scintillator and the photodetector. The scintillator converts the 511 keV photons to light photons that are transformed to an electrical pulse by the photodetector. The scintillator consists of a dense scintillation crystal, today usually LSO (lutetium oxyorthosilicate) or LYSO (lutetium-yttrium oxyorthosilicate), that have a high probability of stopping the incoming photons, fast timing resolution, reasonable energy resolution, and low dead time (10). Some or all the photon energy is deposited in the crystal, which produces light photons proportional to the amount of energy deposited. The light photons are subsequently converted to electrons and amplified by the photodetector (photomultiplier tube (PMT), avalanche photodiode (APD), or silicon photomultiplier (SiPM)) producing an electronic signal that represents a detection of an event. If two photons are detected within a time window (e.g., within 4 ns) in two distinct detectors within an acceptance angle it represents a coincidence event (10).

Historically, PMTs have been the photodetectors used in PET systems due to their fast response, high sensitivity and relatively low noise (10). However, in the development of

integrated PET/MRI systems, solid-state photodetectors were proposed as they are insensitive to high magnetic fields. APDs were first used, which have a compact size and very high photon detection efficiency compared to PMTs, but much lower gain and a limited timing resolution (11). Further development led to the introduction of SiPM that are APDs tightly packed on a common silicon substrate (12). SiPMs combines the advantages of PMTs and APDs, providing high gain and photon detection efficiency, as well as very good timing resolution and compact size. SiPM is now the most used photodetector in modern PET systems, both PET/MRI and PET/CT (10).

1.1.3 Photon interactions in matter and scattering

The annihilation photons may be scattered or attenuated in tissue or hardware (e.g., patient table, coils) before reaching the detectors. γ photons interact with matter by three mechanisms: photoelectric effect, Compton scattering and pair production. The latter process requires a photon energy above 1,022 keV and is not possible for the annihilation photons with an energy of 511 keV. In the case of photoelectric effect the photon is completely absorbed in an interaction with an atom, and its energy is transferred to an orbital electron that is ejected (8). During Compton scattering the photon interacts with a free or loosely bound electron in the medium, transferring some of its energy to the electron and the photon's direction is changed. Compton scattering is the dominating interaction in tissue. The loss in photon flux, or attenuation, through a medium is described by

$$I(x) = I(0)e^{-\mu x} \tag{1}$$

where $I(0)$ is the incoming photon flux and $I(x)$ is the photon flux after passing through a medium of thickness x. μ is the probability per unit distance that an interaction will occur and is called the linear attenuation coefficient (LAC). For the 511 keV photons $\mu \approx \mu_{photoelectric} + \mu_{compton}$.

Scattered events cause incorrect location of annihilations and background noise (Figure 2). In the case where two photons from different annihilations are detected within a coincidence timing window, it is called a random event, which also produce noise in the image. To provide a quantitative correct PET image, correction methods are developed to exclude scattered and random coincidence events (briefly described in section 1.1.6 and 1.1.7), and the loss of 511

keV photons due to interactions in tissue and hardware are compensated by attenuation correction (section 1.1.5).
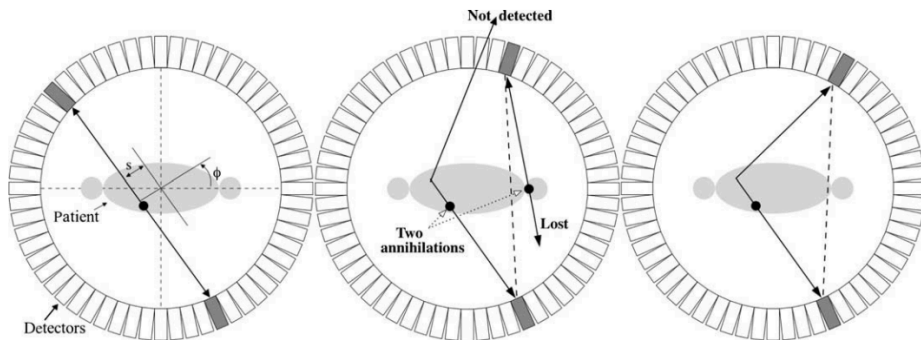
Figure 2 *Types of coincidence events. Left: True coincidence event, Middle: Random coincidence event – two photons from distinct annihilations are detected as a coincidence causing an incorrect LOR, Right: Scattered coincidence event – scatter of an annihilation photon cause an incorrect LOR. Illustration from Alessio et al. (13), published under creative commons license CC BY 3.0 (*https://creativecommons.org/licenses/by/3.0/*).*

1.1.4   Image reconstruction

When two annihilation photons are detected within the coincidence window and both photons have an energy within the energy window (e.g. 350-650 keV (14)) it is registered as an event. This raw data is stored in a sinogram in static acquisitions, where each LOR has a memory location that is incremented by 1. For dynamic scans, both time and location of each event is stored and written to a file (8). This is called listmode acquisition. The raw data is used to reconstruct static or dynamic PET images. Earlier filtered backprojection (FBP) was the standard reconstruction algorithm, but now iterative reconstruction, like Ordered Subset Expectation Maximization (OSEM), is widely used (15). In expectation maximization (EM) reconstruction an initial image is suggested and the corresponding sinogram data are compared to the collected sinogram data (16). The initial image is then updated based on the differences in the data in an iterative process to converge to the true image. More iterations will generate an image closer to the true image but will also introduce more noise. To speed up the iteration process, only subsets of the sinogram data are used in each iteration of OSEM reconstructions.

As mentioned, several corrections are required to provide quantitatively accurate PET images and proper image contrast, like attenuation correction (section 1.1.5), scatter correction (section 1.1.6) and random correction (section 1.1.7), which will be further described. Other corrections

include normalization (accounting for count rate variability among detectors) (17), dead time correction and decay correction, which will not be further discussed in this thesis.

1.1.5   Attenuation correction

Attenuation correction (AC) is the most important correction of PET images and compensates for the loss of annihilation photons due to interactions in tissue or hardware inside the detector ring. Bone has the highest electron density in the body and attenuates the most, followed by soft tissue, fat and lung tissue. Activity in deeper tissue will be more attenuated than tissue closer to the surface of the body and will appear to have lower activity without attenuation correction, as shown in Figure 3.
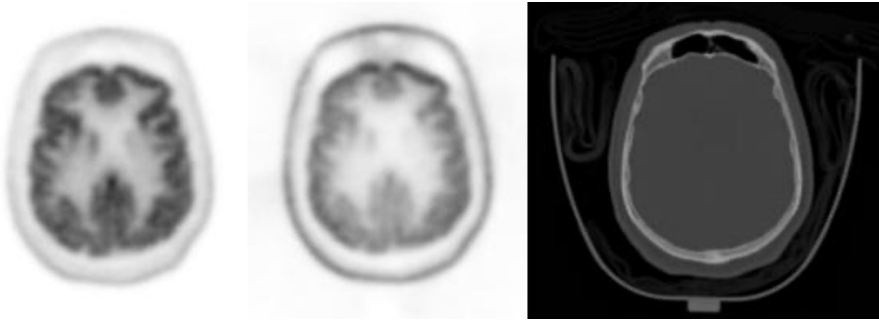
Figure 3 Left: [¹⁸F]FDG brain attenuation corrected (AC) PET image, Middle: not attenuation corrected (NAC) PET image, Right: corresponding CT image used for attenuation correction. The images are from one of the patients included in Paper I.

The probability that an annihilation photon from depth a in tissue (Figure 4) will escape the body and be available for detection is (8)

$$p_1 = \frac{I(a)}{I(0)} = e^{-\mu a} \tag{2}$$

The probability that both annihilation photons will escape the body is then,

$$P = p_1 \times p_2 = e^{-\mu a} \times e^{-\mu b} = e^{-\mu(a+b)} = e^{-\mu D}$$

where *D* is thickness of the body along the given LOR. The attenuation correction factor (ACF) applied to each LOR is the inverse of the probability *P*. As the µ-value vary with different tissue it must be integrated over the distance *D* and ACF becomes,

$$ACF = \frac{I(0)}{I(D)} = e^{\int_0^D \mu(x)dx} \qquad (3)$$

which is multiplied with each LOR in sinogram space.
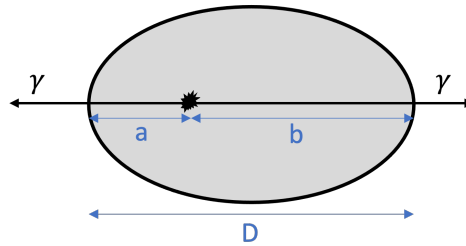
Figure 4 *The attenuation of the two annihilation photons, γ, is dependent on the patient thickness, D.*

For PET only scanners, attenuation is usually measured by rotating Germanium-68 ([68]Ge) rod sources inside the scanner. A blank scan without the patient (*I(0)*) and a transmission scan with the patient inside the scanner (*I(D)*) is then acquired and ACFs for each LOR can be calculated according to Equation 3 (14).

When PET/CT systems were introduced, attenuation correction was instead obtained by CT transmission scans, which is proportional to the attenuation of annihilation photons in tissue and is fast and noiseless compared to the [68]Ge transmission scan. The µ-values are dependent on the photon energy, which is around 70 keV in CT imaging and therefore must be scaled to correspond to the 511 keV photons in PET imaging. This is performed by a bilinear scaling method that converts the CT images to attenuation correction maps (AC maps) (18).

Attenuation correction was one of the big challenges when introducing the clinical PET/MRI systems, which are further described in section 1.3.1.

1.1.6 Scatter correction

As the annihilation photons pass through the body, they may undergo Compton scattering. The direction of the photon is then changed, and the event is assigned to an incorrect LOR (Figure 2). Most scattered photons have a small change in direction and a low loss of energy due to the high energy of the annihilation photons. The energy resolution of PET detectors is not very good, and a wide energy window is normally used (e.g., 350-650 keV) to provide reasonable detection efficacy. Hence the probability for scattered events of being within the energy window is quite high and these events will produce background noise in the image (14). The probability of scattered events increases with tissue density and the size of the patient, the activity and the width of the energy window. The scatter fraction can be more than 40 % in 3D PET and requires correction (8).

Three main categories of scatter corrections exists: analytical, dual energy window, and simulation methods (8). Simulation methods are probably most accurate and simulates scatter based on emission and transmission data. A commonly used method in 3D PET is the single scatter simulation algorithm (19-21). This iterative process simulates scatter based on the radioactive distribution in the emission image and the scattering medium from the AC map. Only single Compton scatter of one of the two annihilation photons is considered, but it has been shown that this method also provides reasonable compensation for multiple scatter as well (20). Although the scatter estimation is based on an uncorrected emission image and no scaling to the scatter contributions outside the object being imaged is performed.

1.1.7 Random correction

Random events occur when two photons from different annihilations are registered as an event and cause degraded image contrast, inaccurate quantification and may produce image artifacts (8, 14). The rate of random events can be estimated by the single correction method, as

$$R = 2\tau \cdot C_1 \cdot C_2 \tag{4}$$

where 2τ is the coincidence timing window and C_i is the count rate of detector i in counts per second. Another frequently used approach to estimate the randoms rate is by applying a delayed coincidence window in addition to the standard coincidence window. The delayed sinogram will only contain random events as no true or scattered events can occur in the

delayed coincidence window. The estimate of the delayed events can then be subtracted from the prompt coincidence sinogram obtained from the standard coincidence window. The delayed coincidence method cause a noisier estimate of random events than the single correction method, but do not introduce systematic errors that may occur in determination of the coincidence timing window in Equation 4 (8).

1.1.8 Time-of-flight

The localization of the annihilation along the LOR can be determined to some degree by the difference in arrival times at the detectors of the two annihilation photons ($t_2 - t_1$). This method is called time-of-flight (TOF) and improves the signal-to-noise ratio (SNR). The position of the annihilation can be restricted to a distance along the LOR (Δx) dependent on the timing resolution (Δt) of the system,

$$\Delta x = \frac{\Delta t \cdot c}{2}$$

(5)

where c is the speed of light (22). TOF requires a high luminosity and fast decay time of the scintillation crystal (like LSO) and photo-detectors with good response time (like PMT or SiPM) (23). Hence TOF is not possible in the Siemens PET/MRI system (Biograph mMR, Siemens Healthineers, Erlangen, Germany) with APD photo-detectors, due to slow response time and low gain requiring amplification prior to processing (23). With TOF the localization of the annihilation along the LOR will be improved, but the accuracy is limited by the time resolution of PET detectors. For the Siemens Biograph mCT PET/CT system with a time resolution of 540 ps, the events are constrained to a segment of 8.1 cm along the LOR (24). TOF cause an increase in SNR compared to conventional PET that is proportional to the diameter (D) of the object being imaged and the timing resolution Δt (25)

$$\frac{SNR_{TOF}}{SNR_{PET}} = \sqrt{D/\Delta t}$$

(6)

Hence TOF provides an increased benefit in imaging of larger patients as they generate more attenuation and scatter.

1.1.9 Spatial resolution and point spread modeling

The spatial resolution is the ability of the system to distinguish two radioactive sources with a defined size at a relatively small distance. A best-case comparison of the spatial resolution between systems can be performed by imaging radioactive point sources in air and measuring the width of the point spread function (PSF) of the sources in reconstructed images. The width of the PSF is measured by the full width at half-maximum (FWHM) and full width at tenth-maximum (FWTM) (26).

The spatial resolution is dependent on several parameters, including both physical limitations related to the radioactive decay and issues related to detector design and image reconstruction. The fact that the emitted positron moves a distance before annihilation and the annihilation photons are not emitted exactly 180° apart, causes a mispositioning of the event and degrades the spatial resolution (8). The positron range is dependent on the kinetic energy of the emitted positron, which differs with radionuclides and tissue density. The degradation of the final spatial resolution by positron range for the most commonly used radioisotope, ^{18}F, is 0.2 mm (14). The noncolinearity is independent of the radionuclide and is due to the remaining kinetic energy of the positron at the time of annihilation. The blurring due to noncolinearity, Δ_{nc}, is proportional to the diameter (D) of the detector ring as

$$\Delta_{nc} = 0.0022 \times D. \tag{7}$$

For the Siemens PET/MRI (mMR) and PET/CT (mCT) systems, Δ_{nc} is 1.44 mm and 1.85 mm, respectively.

The width of the scintillator elements, d, is one of the main factors affecting the spatial resolution (14). The intrinsic resolution of the scintillation detectors is dependent on the distance to the detector and is best at the center of field of view (FOV) and is normally given as $d/2$ in the center of the detector ring and as d at the face of the detector. The width d is typically ~4 mm in clinical PET systems.

The depth of interaction in the detector elements may also degrade the spatial resolution (14). When the annihilation photons are emitted from the center of the detector ring, they will enter perpendicular to the detector elements. However, when the annihilation is located at a radial offset, the photons enter with an angle and may cross one or two detectors before they are deposited. Hence, the event will be assigned to an incorrect LOR towards the center of FOV,

broadening the PSF in the radial direction (27). This effect is dependent on the width and thickness of the scintillator elements, the scintillator material and the distance between the detectors. Most clinical scanners do not have any depth-of-interaction capabilities and the spatial resolution is spatially variable within the FOV (10).

The finite spatial resolution of the PET imaging systems caused by the detector design and the reconstruction process leads to image blurring. This is one of the main two reasons for partial volume effects (PVE), causing the image intensities to be different from what an ideal imaging system would provide (28). The image blurring causes spill out from small lesions and makes them appear larger and with lower tracer uptake than what is real. The second reason for PVE is the image sampling on a voxel grid. The voxel can consist of a mixture of tissues with different tracer uptake but will be represented with the mean intensity in the voxel. Furthermore, motion can also cause PVE due to image blurring. PVE can affect PET images both quantitatively and qualitatively, and typically occurs for tumor sizes smaller than 3 times the FWHM of the reconstructed image resolution (28).

The spatial resolution may improve and become more uniform throughout the FOV with PSF modeling incorporated in the reconstruction algorithm (14, 16), which leads to higher activity recovery and improved lesion detectability (27, 29). However, it should be noted that PSF modeling may cause edge artifacts (Gibbs artifacts) that can affect quantification of sub-centimeter lesions and therefore should be used with care (30, 31).

Reconstructed PET images are usually quite noisy due to the low tracer dosage to minimize radiation dose to the patient and the limited acquisition time in clinical imaging (32). Post-reconstruction filtering, such as Gaussian filter, is therefore usually applied to smooth the image and improve the signal-to-noise ratio (8). Consequently, the spatial resolution is degraded as high frequencies containing the detailed information are removed and the image is blurred.

1.1.10 Image quality and detectability

The PET image quality is dependent on spatial resolution, contrast and noise (33). Spatial resolution is the sharpness of the image, while contrast is the difference in image intensity of regions with different activity concentration. Noise can be statistical noise originating from

random fluctuations in radioactive decay or structured noise caused by for example imaging system artifacts. Random noise will always be present in nuclear medicine images, due to the random nature of radioactive decay causing statistical variations in counting rates. Especially for low activity concentrations this will degrade the image quality. Change in one of the three image quality factors will affect the others. For instance, increase in noise will deteriorate the contrast. To detect a lesion in an image, it must be distinguishable from the surrounding tissue and high noise levels makes this difficult. In oncology, the possibility to detect small lesions at an early stage is of high importance.

The *detectability* of an object being imaged is found to be dependent on the contrast-to-noise ratio (CNR) (33). CNR of a lesion/uptake volume can be measured as (33),

$$CNR = \frac{|C_H - C_B|}{SD_B} \qquad (8)$$

where C_H and C_B are the average counts in regions of interest (ROIs) covering the lesion/uptake volume and the background, respectively. SD_B is the standard deviation of the counts in the background ROI. Studies have concluded that an object's CNR must exceed a factor of 3-5, called the Rose criterion, to be detectable (33). The exact value depends on parameters like the object's size and shape, edge sharpness, experience of the observer and viewing distance.

The ability of the PET system to recover the activity concentration of an object is also important for detectability, and can be measured in phantom studies by the *contrast recovery coefficient* (CRC) as (26, 34)

$$CRC = \frac{\left(C_H/C_B\right) - 1}{\left(a_H/a_B\right) - 1} \qquad (9)$$

where a_H and a_B are the true activity concentration in a hot sphere and the background of the phantom. The activity in small spheres is poorly recovered by PET systems due to the limited spatial resolution that cause partial volume effects. Recovery coefficients measured by phantom studies for different uptake sizes can be used clinically to adjust for the underestimation of activity in small lesions.

In addition to the ability of the system to represent the object being imaged, the contrast and detectability is highly dependent on the radiopharmaceutical and the difference in uptake between a lesion and normal surrounding tissue. Therefore, a tracer with as high tumor-to-background ratio (TBR) as possible is desired, which is dependent on the uptake mechanisms of the radiopharmaceutical.

1.1.11 Radiopharmaceuticals

The radiopharmaceutical injected into the bloodstream of the patient prior to a PET examination consists of a positron-emitting nuclide labelled to a tracer. The radionuclide emits the signals, while the tracer determines the fate of the molecule inside the body. Nuclides suitable for PET imaging must have a half-life long enough for the imaging procedure and should not substantially alter the biological behavior of the tracer. The tracers can for example be markers for glucose or amino acid metabolism, cell proliferation, tumor hypoxia or specific targets like transporters or receptors (35).

As mentioned, [^{18}F]FDG is the most widely used radiopharmaceutical in PET imaging as ^{18}F has an appropriate half-life (110 min) and [^{18}F]FDG mimics glucose metabolism. The energy demand is altered in many diseases and [^{18}F]FDG has been shown to be a sensitive marker for both neurodegenerative diseases, epilepsy, cardiac diseases, and most cancers (36). [^{18}F]FDG is transported into cells by glucose transporters and phosphorylated to [^{18}F]FDG-6-phosphate that cannot enter the glycolysis and hence accumulates in the cells (37). Organs like the heart and brain have a high glucose metabolism and hence a physiological [^{18}F]FDG uptake. The increased [^{18}F]FDG uptake in healthy brain parenchyma is exploited for imaging of neurodegenerative diseases while it degrades the contrast in neuro-oncology.

For neurodegenerative diseases, [^{18}F]FDG PET is recommended as a clinical tool to differentiate normal age-related alterations of glucose metabolism from early stages of dementia and other neurodegenerative diseases (38). Reduced glucose metabolism (hypometabolism) in specific brain regions can help identify subtypes of dementia and may be present prior to morphological changes visible on MRI. [^{18}F]FDG PET shows unspecific alterations in glucose metabolism, but more specific tracers for neurodegenerative conditions have become clinically available and is a potential tool for even earlier diagnosis (39). These tracers targets amyloid-β (Aβ) aggregates and tau neurofibrillary tangles, which are hallmarks

of Alzheimer's disease (AD) that can be present already in the presymptomatic phase (39). The most studied amyloid tracer is the [carbon-11]-labelled Pittsburgh Compound-B ([^{11}C]PiB), but three [^{18}F]-labelled tracers are now FDA approved ([^{18}F]-florbetapir, [^{18}F]-florbetaben, and [^{18}F]-flutemetamol). [^{18}F]-flortaucipir is the only FDA-approved tau tracer, but many tracers are under development and rapid progression is done in this field (39). Still [^{18}F]FDG PET is advantageous due to the high availability, and is complementary to amyloid and tau PET imaging.

In oncology, the increased [^{18}F]FDG uptake in most tumor cells compared to healthy tissue gives a good contrast for detection of tumors, but inflammation may cause false positive findings. In the brain, the high physiological uptake of [^{18}F]FDG cause a poor contrast between normal and pathological tissue. [^{18}F]FDG PET can be used for differentiation of tumor recurrence and radiation necrosis, or to distinguish glioma from central nervous system (CNS) lymphoma or opportunistic infection (40). However, more specific tracers with low uptake in normal tissue are preferred, especially for tumor detection and delineation. Tumors often show increased protein synthesis and hence overexpression of L-amino acid transporters (LAT) and enhanced amino acid (AA) uptake (35). AA tracers have therefore been developed and provide better tumor contrast for brain tumors compared to [^{18}F]FDG (41, 42). Some AA tracers are now recommended in glioma imaging, including L-[methyl-^{11}C]-methionine ([^{11}C]MET), O-(2-[^{18}F]Fluoroethyl)-L-tyrosine ([^{18}F]FET) and L-3,4-dihydroxy-6-[^{18}F]fluorophenylalanine ([^{18}F]FDOPA) (43).

[^{18}F]FET is probably the most frequently used of the three recommended AA tracers, due to the short half-life of [^{11}C]MET and physiological uptake of [^{18}F]FDOPA in striatum that can cause difficulties for detection and delineation of tumors in this area. Unlike [^{11}C]MET and [^{18}F]FDOPA, [^{18}F]FET are not metabolized or incorporated into proteins after transportation into cells (44). Hence the uptake primarily measures AA transport, which simplifies and enables tracer kinetic analysis. Kinetic analysis of [^{18}F]FET can improve differentiation of low-grade and high-grade glioma (45-47), and tumor recurrence from treatment-related changes for both glioma (48, 49) and brain metastases (50-52). AA PET is not recommended in primary evaluations of brain metastases and the literature of recurrence evaluations is still limited.

An artificial AA tracer, anti-1-amino-3-[^{18}F]fluorocyclobutane-L-carboxylic acid ([^{18}F]FACBC), has been found to exhibit an even better tumor contrast compared to [^{11}C]MET for gliomas due to lower uptake in healthy brain parenchyma (53-55). [^{18}F]FACBC has also

shown potential to differentiate high- and low-grade glioma based on TBRs (53, 56, 57). Only a case report (58) and a study of 8 patients (59) are conducted with [^{18}F]FACBC in patients with brain metastases. Relatively high TBRs compared to studies on [^{11}C]MET and [^{18}F]FET were found, as well as the ability to differentiate tumor recurrence from radiation necrosis. Furthermore, the case report showed increasing [^{18}F]FACBC uptake with tumor progression. [^{18}F]FACBC is a promising tracer for brain tumors and is further studied in patients with brain metastases in the current thesis.

1.1.12 Clinical evaluation of PET images

Clinical evaluation of PET images differs between different diagnostic applications. In addition to visual interpretation of the images, different quantitative measurements can be helpful tools to set the clinical diagnose or to evaluate treatment response.

In the evaluation of patients with suspected dementia, detection of hypometabolism in specific brain regions can help diagnose different subtypes of dementia, like AD, frontotemporal dementia or dementia with Lewy bodies (60). In addition to visual inspection of hypometabolism, the [^{18}F]FDG uptake of a patient can be quantitatively compared to age-matched databases of healthy controls, either in volumes of interest (VOIs) or at voxel-level (61). Z-scores are then calculated, representing the number of standard deviations that separates the [^{18}F]FDG uptake of the patient compared to the healthy controls. A z-score between -2 σ and -3 σ is defined as moderate hypometabolism, while a z-score below -3 σ represents severe hypometabolism (62). The z-scores are based on small differences in activity concentrations and quantitatively accurate PET images is of particular importance for this purpose.

In oncology, the PET images are inspected for lesions with increased tracer uptake compared to normal tissue. To quantitatively evaluate the tracer accumulation in tissue the standardized uptake value (SUV) is widely used in oncology. SUV is the activity concentration in tissue compensated for variations in injected activity and patient size, defined as

$$SUV = \frac{c}{A/w} \qquad (10)$$

where c is the activity concentration measured in a ROI (e.g., maximum or mean) in the PET image [kBq/ml], A is decay-corrected injected activity [kBq] and w is the patient's body weight [g] (63). Body surface area or lean body mass can be used as a measure of patient size instead of body weight and have shown to be less weight-dependent for obese patients in [^{18}F]FDG examinations (64). SUV is often measured in the lesion and in a reference tissue for calculation of TBR, which can be used as a complement to SUV that also considers the uptake in the surrounding tissue. In the brain, the contralateral hemisphere is commonly used as reference and a crescent-shaped VOI has been found to minimize intra- and inter-reader variability (65).

The use of SUV is controversial as it is affected by many factors that are not controlled for, like length of the uptake period, plasma glucose level and partial volume effects (66). Hence, it must not be used as an exact quantitative measure of tracer uptake and the length of the uptake period should be kept as stable as possible and the plasma glucose level should be below values recommended by guidelines.

1.1.13 Dynamic PET

Dynamic PET uptake acquired in listmode can be used to investigate the tracer uptake over time. In this case the radiopharmaceutical is usually injected at the same time as the PET acquisition is started. The activity in a ROI can then be plotted as a function of time, called time activity curves (TAC), to visualize tracer kinetics in that region.

Dynamic [^{18}F]FET PET imaging can provide valuable information in assessments of glioma and brain metastases, for instance by improving the accuracy of differentiation between recurrence of tumor tissue and treatment-induced changes based on the TAC characteristics, like the slope of the curve and the time-to-peak (48, 50-52). Radiation necrosis and low-grade gliomas have in general shown a slowly increasing curve pattern without a definite peak, while recurrent metastatic tissue and high-grade glioma as well as low-grade glioma with shorter progression free survival tends to have an early peak followed by a plateau or constant decrease (45, 50, 67, 68).

Furthermore, dynamic [^{18}F]FET PET imaging improves differential diagnosis between low-grade and high-grade gliomas and provides prognostic information within all grades of glioma prior to treatment (43).

1.2 MRI

MRI provides both anatomical and functional images of the body, with an excellent soft tissue contrast and a high spatial resolution compared to PET. The first whole-body MRI system was constructed in 1977 and was FDA approved in 1984. Today MRI is widely used in neurology, oncology, cardiology, imaging of joints and more.

1.2.1 Basics of MRI

MR imaging is exploiting the spin of hydrogen nuclei present in the body. The spin and the positive charge of the hydrogen nucleus cause a small magnetic field, called magnetic moment (Figure 5A) (69). Other atoms in the body also possess a magnetic moment, but the very high abundance of water and hence hydrogen atoms in the body and the relatively large magnetic moment makes hydrogen the best suited atom for MR imaging.
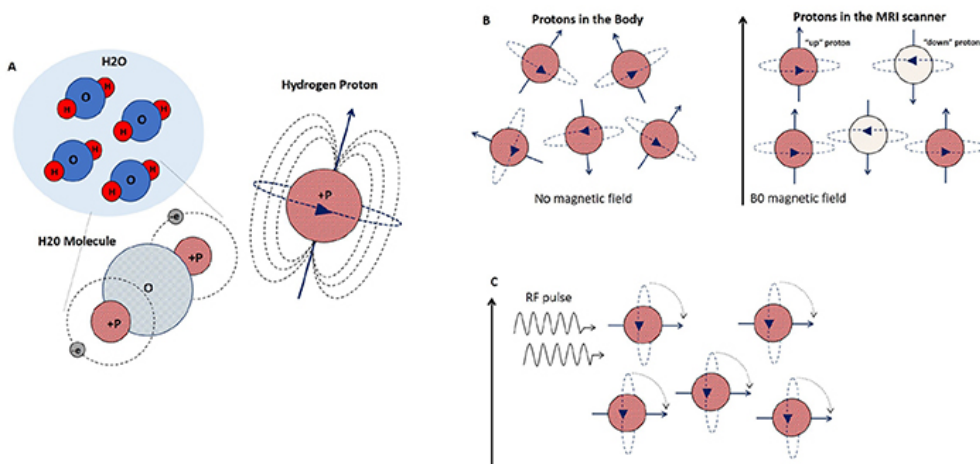
Figure 5 *A) The water molecule (H20) consists of one oxygen atom and two hydrogen atoms. The hydrogen atoms have a single positive charge in their nucleus, a proton, spinning around its own axis (precessing) and producing a small magnetic field, called magnetic moment. B) When the magnetic moments are placed in a static magnetic field (B_0) they will align with the field, both in the same ("up") and the opposite ("down") direction but with an access of "up" protons. C) An RF pulse with a flip angle of 90° is applied orthogonal to the B_0 field flipping the spinning protons to the transverse plane as they absorb the RF energy. Illustration from Broadhouse (70), published under creative commons license CC BY 4.0 (https://creativecommons.org/licenses/by/4.0/).*

When the patient is placed inside a static magnetic field (B_0) in the MRI scanner, the magnetic moments of the hydrogen nuclei in the body will align with B_0, parallel or anti-parallel (Figure

5B). More spins will align parallel than anti-parallel and hence cause a net magnetization vector (NMV) in the direction of B_0 (z-axis). The magnetic moments then circle, or precess, around B_0 at a frequency called the Larmor frequency, which is proportional to B_0.

To generate MR signals from the body, a radiofrequency (RF) pulse (at the Larmor frequency of hydrogen) that produces an oscillating magnetic field (B_1) at 90° to B_0 is transmitted from a transmit coil. A RF excitation pulse with a flip angle of 90° causes the magnetic moments of the hydrogen nuclei to precess coherently in the transverse plane instead of the longitudinal plane and the NMV is flipped to the transverse plane (Figure 5C).

Before the RF pulse is applied, there exist no transverse component of the NMV as the magnetic moments are out of phase. When B_1 is present, the magnetic moments align with this field and results in a coherent magnetization that precesses in the transverse plane.

A receiver coil is placed orthogonal to the transverse component of the NMV to measure the MRI signal. The changing magnetic field by the precessing NMV induces a current and hence a voltage in the coil, which is the MRI signal. When the RF pulse is turned off, NMV realigns with B_0, a process called relaxation. Relaxation both results in recovery of the longitudinal magnetization (T1 recovery) and decay of the coherent transverse magnetization (T2 decay). The voltage in the receiver coil then decreases and this is called the free induction decay (FID) signal.

The FID signal is affected by the T1 recovery time (the time it takes for 63% of the longitudinal magnetization to recover) and the T2 decay time (the time it takes for 63% of the transverse magnetization to dephase), both which differ for different tissue. RF pulses can be combined in pulse sequences with optimal timing and magnitude to emphasize the differences in T1 recovery, T2 decay or proton density to obtain the intended image contrast in anatomical images. For instance, a T1-weighted image (Figure 6A) will show a high intensity for fat that has a short T1 recovery time and a low intensity for water with a long T1 recovery time. While the contrast for fat and water is the opposite in a T2-weighted image (Figure 6B).
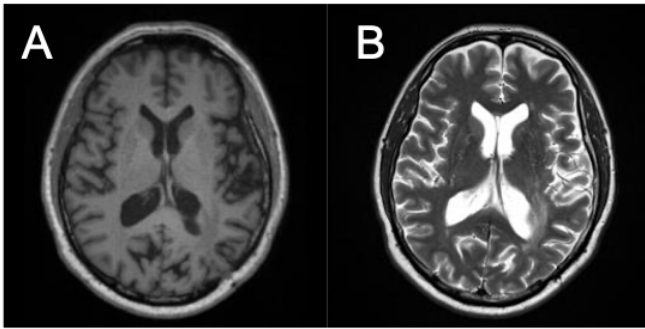
Figure 6 A T1-weighted image, B T2-weighted image. The images are from a glioma patient included in an ongoing study at St. Olavs Hospital.

The FID signal decays really fast and to be able to measure the signal the magnetic moments are rephased to produce an echo at a later timepoint that can be collected (Figure 7). The rephasing can be achieved either by applying a 180° RF pulse or graded magnetic fields (gradients). Such sequences are called spin-echo and gradient echo pulse sequences, respectively.
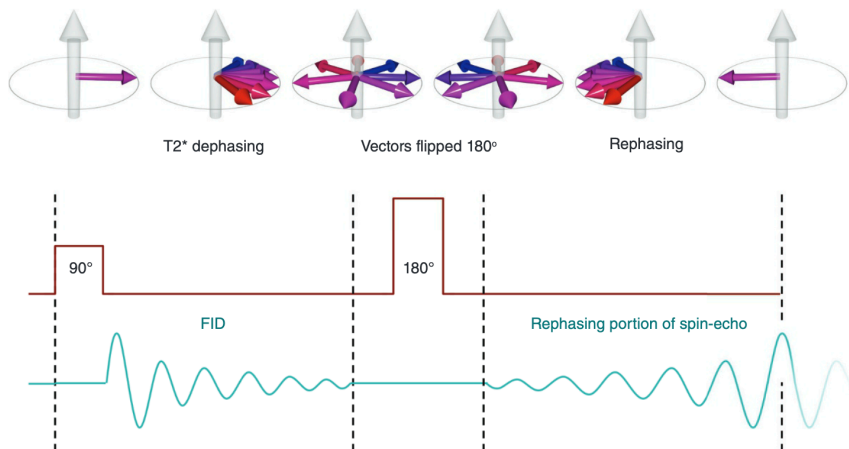
Figure 7 Rephasing in a spin-echo pulse sequence. The pulse sequence diagram shows the application of a 90° pulse that cause the NMV vector to lay in the transverse plane, and the 180° pulse that rephase the dephasing magnetic moments and hence generating the spin-echo. Copyright (2021) Wiley. Used with permission from Catherine Westbrook and John Talbot, MRI in practice, 2018, John Wiley and Sons, p. 62.

To be able to spatially locate the MRI signals gradients must be applied in the x, y and z-direction. Gradients are spatially varying magnetic fields with a linear slope superimposed onto the main magnetic field (B_0). The precessional frecency of the magnetic moments depends on the magnetic field strength they experience. The gradients cause the spins to process at slightly different frequency at spatially different locations, making it possible to locate the signal originating from a small 3D volume based on their precessional frequency.

The first gradient applied during a pulse sequence is called the slice-select gradient and is applied in either x (for sagittal images), y (coronal) or z (axial) direction (Figure 8). This gradient is applied during the RF excitation pulse, and also during the RF rephasing pulse in a spin-echo sequence. Only magnetic moments with the precessional frequency of the RF excitation pulse (within a bandwidth) are excited and a slice (2D plane) is selected.

In the spatial encoding of the two remaining orientations, the difference in precessional phase and frequency of the magnetic moments along the gradient is utilized. The phase-encoding gradient is usually applied after the RF excitation pulse and in the shortest axis of the anatomy (e.g., from the left to the right of a patient (x-axis) in coronal images). This gradient induces phase differences along the direction of the gradient, while nuclei in slices perpendicular to the gradient will have the same phase. When the gradient is switched of, the phase differences still remain and are present during readout of the signal. The amplitude of the phase-encoding gradient is altered for every RF excitation pulse, and the difference in phase for each excitation is used to determine the spatial location of the signal.

Eventually, the frequency encoding gradient is applied during the readout of the signal, and usually along the long axis of the anatomy (e.g., z-direction in coronal and sagittal images). This gradient cause frequency differences along the direction of the gradient, while nuclei in slices perpendicular to the gradient will have the same frequency. The spatial locations of the nuclei along gradient are hence differentiated based on the difference in precessional frequency. Multiple repetitions of the RF pulse excitation with different center frequency and varying phase-encoding gradients are required to sample data for a 3D image.
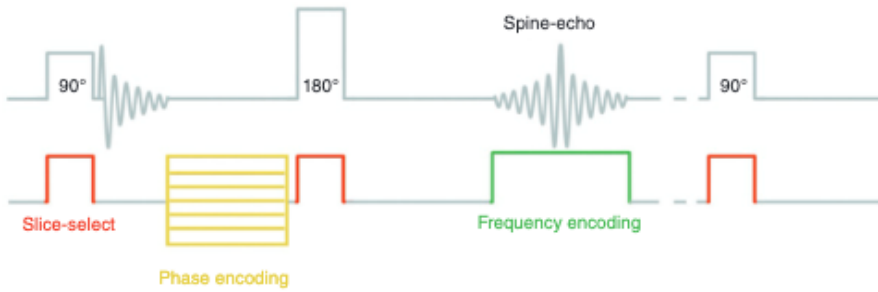
Figure 8 Application of gradients for spatial location in a spin-echo sequence. Copyright (2022) Wiley. Used with permission from Catherine Westbrook and John Talbot, MRI in practice, 2018, John Wiley and Sons, p. 153.

The acquired MR data is stored in *k*-space, which is a spatial frequency domain with one frequency axis (k_x) and one phase axis (k_y) as seen in Figure 9 (69). *k*-space data contains information about where frequencies within a slice are located and can be converted to an image by inverse Fourier Transform. One line along k_x is sampled during readout of the signal while the frequency encoding gradient is applied. The position along k_y is determined by the amplitude of the phase encoding gradient, hence varying amplitudes are required to fill k-space. How *k*-space is filled is determined by the polarity and amplitude of the gradients and RF pulses.
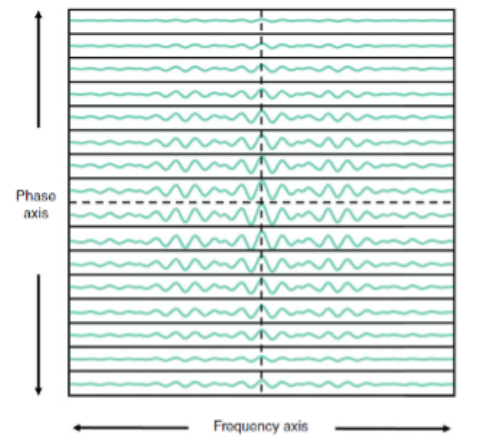
Figure 9 The axes of k-space. Copyright (2022) Wiley. Used with permission from Catherine Westbrook and John Talbot, MRI in practice, 2018, John Wiley and Sons, p. 160.

The time from the application of one RF pulse to the next RF pulse in a pulse sequence is called the repetition time (TR) and determines the amount of T1 recovery in tissue. While the time from the application of the pulse to the collection of the signal is the echo time (TE) and determines the amount of T2 relaxation when measuring the signal.

The repetition time, echo time and the flip angle of the RF pulse are some of the most important contrast parameters that determines the image contrast in MRI. Furthermore, contrast agents can be administered orally or intravenously to improve the contrast of pathology as they shorten the T1 or T2 relaxation times. Gadolinium is the most frequently used contrast agent and shortens the T1 relaxation time. In brain tumor imaging gadolinium are often used for tumor enhancement as the contrast agent will leak into the tumor if the blood-brain barrier (BBB) is disrupted and cause hyperintense areas in T1-weighted images. Contrast-enhanced MRI (ce-MRI) is the recommended imaging modality in detection of brain metastasis (71), as seen in Figure 10.
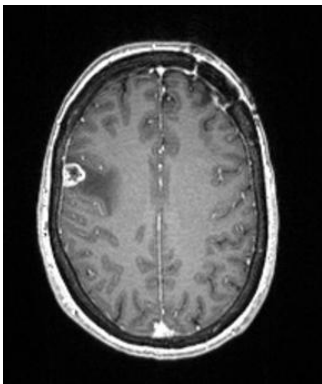
Figure 10 *A T1-weighted image with contrast enhancement after gadolinium administration of a patient with a brain metastasis included in the study of Paper III.*

Other advanced MRI techniques also exists, like functional MRI (fMRI) to investigate regional brain activation, diffusion-weighted imaging (DWI) that measures water mobility that is an imaging biomarker of tissue pathology, perfusion-weighted imaging (PWI) for imaging of blood flow and vascularity, and MR spectroscopy (MRS) for assessment of metabolites (72).

1.3 PET/MRI

As mentioned, PET was earlier stand-alone systems, while PET/CT systems are now the new standard in PET imaging. PET and CT are integrated in one modality but acquired sequentially. The CT image can provide anatomical information for localization of abnormalities in the PET image and is used for attenuation correction.

MRI provides an excellent soft tissue contrast compared to CT, which is especially important in brain and pelvis imaging. MRI may also include diffusion, perfusion, functional and spectroscopy data. However, new challenges were faced when combining PET with the magnetic field of MRI. The light photons in the PMT detectors and the front-end electronics of the PET system interfered with the magnetic field (7). Furthermore, the PET detectors potentially affected the MR image quality due to inhomogeneities in the magnetic field, eddy currents and electromagnetic interference (7). The first simultaneous PET/MRI system was a single-slice preclinical PET system placed inside the receiver coil of a MRI scanner (73). The PMTs were placed outside the main magnetic field and connected with long optical fibers. This configuration caused degraded PET signal due to optical loss in the fibers. A prototype PET brain insert with APD detectors constructed to fit inside a clinical MR system was developed in the late 2000s as the first human system (74, 75). While the first clinical whole-body PET/MRI systems were introduced in 2010, a sequential system by Philips and an integrated system by Siemens Healthcare. The sequential system was equipped with separated PET and MRI gantries, but with shared examination table and magnetic shielding for the PMTs and removal of PET gantry electronics to an equipment room (6). In the integrated system the PET detectors were placed in between coils in the MRI system and was equipped with APD photodetectors (76). In 2016 a second integrated clinical PET/MRI system was introduced by GE Healthcare with SiPM detectors, capable of TOF PET imaging (77), followed by a third system introduced in 2018 by United Imaging Healthcare, also with SiPM detectors (78).

1.3.1 Attenuation correction

Although the issues with operating PET detectors in magnetic fields were solved for PET/MRI systems, attenuation correction based on MR images was another big challenge. MR images are not proportional to electron density like CT images and does not inherently provide attenuation properties of tissue. Several MRAC approaches have been developed and the

methods are often categorized as segmentation-based or atlas-based (79). Reconstruction-based methods using PET emission data has also been proposed (80).

In segmentation-based approaches tissue are segmented into tissue classes based on a T1-weighted sequence or a dual-echo Dixon sequence (81, 82). The tissue classes have constant and predefined LACs. With the Dixon sequence, in- and opposed-phased images are acquired from which fat and water images are generated (82). Based on these images the patient's body can be segmented into the tissue classes air, lung tissue, fat, fat/soft tissue mix and soft tissue ($\mu_{air} = 0$ cm^{-1}, μ_{lung}=0.022 cm^{-1}, μ_{fat}=0.085 cm^{-1}, $\mu_{fat/soft\ tissue}$=0.0927 cm^{-1}, $\mu_{soft\ tissue} = 0.100$ cm^{-1} on the Siemens system). Atlas-based methods requires databases of CT images or CT and MRI pairs, and a pseudo-CT image are generated after co-registration between the MR image of the patient and the database-subjects (83-85). Reconstruction-based methods simultaneously reconstruct activity and attenuation based on maximum-likelihood (86).

In clinical PET/MRI systems, segmentation-based approaches are most frequently used for attenuation correction because of short processing time. Initially, bone was not included in MRAC maps but assigned as soft tissue, although it attenuates photons the most among the tissues in the body. This led to underestimations of the tracer uptake of about 25% in bony tissue and 7-11% in bone lesions, and 3% in soft tissue adjacent to bones (85, 87). Especially for the brain that contains a lot of bone, inclusion of bone in the MRAC map is crucial for accurate quantification (87). Underestimations of 25% have been shown in cortical regions when omitting bone, decreasing with distance from the skull (88). Bone should therefore be included in brain MRAC maps. However, the very short relaxation time of bone leads to rapid decay of the MRI signal that cannot be measured with conventional MRI sequences.

Various methods have therefore been developed to incorporate bone in the MRAC maps, but mainly for the brain as the rigidity of the body region ease the process. Specific MRI sequences with ultrashort echo-time (UTE) (89) and zero-echo time (ZTE) (90, 91) have been implemented on the Siemens and GE systems, respectively, to measure bone signal and generate segmentation-based MRAC maps with bone. In the UTE method, two echo times are used – one immediately after the excitation pulse (TE$_1$) when bone signal exists and the second after refocusing the spins (TE$_2$) when the bone signal has fully decayed. The segmentation is based on the difference in bone signal at the two echo times. The MRAC map is segmented into the tissue classes air, soft tissue and bone ($\mu_{air} = 0$, $\mu_{soft\ tissue} = 0.1000$ cm^{-1}, μ_{bone}=0.1510

cm^{-1}). The UTE method improves the quantitative accuracy compared to MRAC methods omitting bone but underestimates the PET activity in the brain (79, 92, 93). A global average bias in [^{18}F]FDG uptake in the brain of -5.7% compared to CT-based AC (CTAC) was found by Ladefoged et al. (79), and underestimation of up to 17.3% in cerebellum was shown by Dickson et al. (93). Aasheim et al. (92) concluded that the UTE method performed acceptable in the brain, but not in the neck and facial regions due to misclassification in air/tissue interfaces and overestimation of bone in the neck region. With the ZTE method, tissue is classified as air, soft tissue and bone by thresholding (91). Followed by implementation of continuous bone information based on linear correlation between CT and ZTE values. No global bias (-0.09%) was found for the ZTE method but over- and underestimations of up to 8% was found in some regions (91). For instance, due to misclassification of air and bone in mastoid and nasal areas. More accurate segmentation is therefore warranted.

Atlas-based approaches have also been implemented at the clinical PET/MRI systems. On the Siemens system, an atlas-based approach was implemented in the latest software upgrade to include a selection of bones (upper femur, hip, spine, skull) into the Dixon MRAC map (85, 94). Continuous LACs for bone (μ=0.1000-0.2485 cm^{-1}) are then included based on a database of more than 200 Dixon images and bone mask pairs. The MR image of the model is registered to the MR image of the subject for each major bone in several steps. Subsequently the same transformation is performed on the bone masks and bone information is added to the segmented Dixon MRAC map of the subject. A prototype of this method showed a global average bias in [^{18}F]FDG uptake of -1.7% and has a short processing time compared to other promising MRAC methods in the literature, which is important in clinical routine (79). GE also offers an atlas-based approach for the brain, generating a pseudo-CT with continuous LACs from a T1-weighted image as input (84, 95). The database consists of CT images of 50 subjects. The average [^{18}F]FDG uptake in the whole-brain was found to be underestimated of about 2% by this atlas-based method, with larger underestimations (<8 %) in regions near the skull base. The performance of the atlas-based method was inferior to the ZTE method (91, 95).

Several atlas-based methods proposed in the literature show improved results compared to clinically implemented methods (79), like the UCL (University College London) method by Burgos et al. (83). This method is based on a database of T1-weighted MRI and CT data sets. All MRI data sets of the database are registered to the MRI data of the patient. Based on correlation coefficients between the MRI data at each voxel, a pseudo-CT is generated. The

UCL method has shown an average global bias in [^{18}F]FDG brain uptake of 0.8% and regional average errors within $\pm$ 3% (79).

Deep learning algorithms have been increasingly used in research MRAC methods in recent years, and in the newest PET/MRI system by United Imaging Healthcare it has been clinically implemented (96). The in-phase and out-of-phase images of a Dixon sequence are used as input in a deep neural network to provide segmented brain MRAC maps including air, fat, soft tissue and cortical bone (μ_{air} = 0 cm^{-1}, μ_{fat} = 0.080 cm^{-1}, $\mu_{soft\ tissue}$ = 0.096 cm^{-1}, μ_{bone} = 0.161 cm^{-1}). For the body, lung tissue is also included (μ_{lung}=0.020 cm^{-1}) and continuous bone LACs. This method is yet to be evaluated for the brain, but large deviations in SUV compared to CTAC has been found, especially for bone tissue (-18.8%) and bone lesions (-18.1%) (97).

Nevertheless, several deep learning methods in the literature generating pseudo-CT images from MR images have shown promising results for attenuation correction in the brain. A method by Ladefoged et al. provides average errors compared to CT below 1% in any brain region (98). Both Dixon (DeepDixon), T1 weighted (DeepT1) or UTE (DeepUTE) images can be used as input in this deep learning-based method with comparable results. Another method by Blanc-Durand et al. using ZTE images as input, provided an average error of -0.2% compared to CTAC and below 2% in any brain region (99). This deep learning method have shown better performance compared to the atlas-based and the ZTE methods implemented on the GE system.

For attenuation correction of the whole body, deep learning methods for generating attenuation corrected PET images from non-attenuation corrected PET images are under development (100-104). This is more challenging than for the brain, especially in the chest and diaphragm regions due to high heterogeneity of tissue and respiratory motion (100-102).

1.3.2   Clinical applications of PET/MRI

The main advantages of PET/MRI over PET/CT are the reduction in ionizing radiation, the improved soft tissue contrast and the possibility of simultaneous imaging (105). Simultaneous imaging provides equal positioning and size of organs, like the urinary bladder in prostate imaging. The other factors make PET/MRI favorable in applications where soft tissue contrast

is important for the diagnostic accuracy and when minimization of radiation exposure is of high importance, namely in pediatric imaging. Oncology is the main application for PET/MRI but there is increasing interest for non-oncology applications like neurodegenerative diseases, cardiology, and Crohn's disease (105, 106).

MRI examinations are most often focused on one body region and the protocols are designed to do multi-sequence MRI to take advantage of the different MRI techniques. A whole-body PET/MRI examination may therefore take more than an hour and for this reason PET/MRI is probably better suited for focus on smaller body regions than PET/CT, which usually cover the head to thigh of the patient (whole-body) in 15-20 min. However, more efficient MRI protocols are possible and whole-body PET/MRI examinations of less than 30 min has been purposed in lymphoma and pediatric imaging (107, 108).

In pediatric imaging, PET/MRI may be preferred over PET/CT if available because of the reduced radiation exposure to the patient as MRI does not produce ionizing radiation. Low dose CT scans can reduce the radiation exposure at the expense of image quality but still cause a radiation dose of about 2 mSv, compared to around 5 mSv for a PET examination (107). Children are more sensitive to radiation exposure than adults and have a long life expectancy (109). The As Low As Reasonably Achievable (ALARA) principle of radiation safety is therefore especially important in pediatric protocols. Additionally, they may undergo many examinations.

PET/MRI provide diagnostic information comparable to PET/CT for most cancer types but may be superior to PET/CT in prostate cancer and in malignant bone disease and inferior in detection of small lung nodules (110, 111). Despite the difference in attenuation correction and decreased SUV in bone for PET/MRI, the PET images of the two modalities provide similar performance in visual lesion detection and correlating SUVs in the mentioned applications (112-114). Hence the differences in performance are mainly based on the anatomical imaging. MRI provides better anatomical allocation of lesions of prostate cancer and bone metastases compared to CT (113-115), but is inferior in detection of pulmonary lesions, especially for lesions less than 1 cm (112). The limited spatial resolution of MRI in lung imaging is due to respiratory motion, low proton density and fast transverse magnetization decay (111, 112).

PET/MRI is probably best suited for body regions where MRI already is the standard imaging modality, like in the head and pelvis, and for applications where PET can add complementary

information to MRI. PET/MRI has shown superior diagnostic accuracy compared to MRI alone for, but not limited to, gliomas (43), neurodegenerative diseases (116), head and neck cancers (117-119), gynecological malignancies (120, 121), and prostate cancer (122).

In neurology, PET/MRI can play an important role in both oncology, neurodegenerative diseases and epilepsy. In neuro-oncology, MRI is used for evaluating primary and metastatic brain tumors at all disease stages, meaning primary evaluation, presurgical planning, postsurgical evaluation, radiotherapy planning, surveillance during chemotherapy, and in evaluation of recurrence. However, MRI abnormalities including contrast enhancement, T2 or fluid attenuated inversion recovery (FLAIR) hyperintensities, are unspecific and can originate from infection, inflammation, ischemia, demyelination, and treatment-related effects (71). Hence conventional MRI has limitations in tumor delineation, detection of treatment-induced changes and evaluation of treatment response, as well as glioma grading (40, 71). Advanced MRI techniques, such as PWI, DWI and MRS show potential in improving the shortcomings of conventional MRI (123). For instance, the combination of PWI and MRS has shown high accuracy in differentiation of neoplastic and non-neoplastic tissue (124). However, the literature is still limited and controversial (125).

AA PET is increasingly used and recommended to support MRI in the clinical management of gliomas jointly by the European Association of Nuclear Medicine (EANM), the Society of Nuclear Medicine and Molecular Imaging (SNMMI), the Response Assessment in Neuro-Oncology with PET (PET-RANO) working group, and the European Association for Neuro-Oncology (EANO) (40, 43). AA PET has shown higher diagnostic accuracy compared to MRI in differentiation of glioma and non-neoplastic lesions or treatment-related changes, in glioma grading, and in assessment of treatment response (43). Furthermore, AA PET has detected tumor tissue beyond contrast enhancement on MRI and metabolically active tumor volume defined by PET are larger than contrast enhancement on MRI. Delineation of tumor borders by AA PET is superior to MRI both in non-contrast enhancing and contrast enhancing gliomas (43). Additionally, AA PET is well suited for biopsy and resection planning.

Less literature is available for AA PET on brain metastases. Ce-MRI is the recommended imaging modality for detection of brain metastases and has a high sensitivity also for small metastases (71). Due to the inferior spatial resolution, PET has limited sensitivity for metastases with diameter less than 1 cm. Brain metastases are usually well delineated on ce-MRI and there is lacking evidence that amino acid PET improves biopsy or treatment planning

(71). However, contrast-enhancement represents blood-brain barrier breakdown that is not specific for tumor tissue but can be caused by treatment like radiotherapy, the main treatment for brain metastases in addition to surgery. [18F]FET PET has been found useful for differentiation of relapsing brain metastases and radiation-induced changes, and probably with highest accuracy for a combination of static and dynamic evaluation (50-52, 71). Furthermore, [18F]FET PET shows promising results in detecting pseudoprogression and evaluation of treatment response of newer treatment options for brain metastases, immunotherapy and targeted therapy, which is difficult with MRI and is important for not terminating effective treatment (126-128).

Neurodegenerative diseases are characterized by loss of neuronal tissue, and the most common are AD, Parkinson's disease (PD), frontotemporal dementia (FTD), and dementia with Lewy bodies (DLB) (39). MRI is used to demonstrate specific atrophy patterns of distinct neurodegenerative diseases and to exclude other pathologies (129). PET is increasingly being used to support the MRI findings as PET can detect pathology at a molecular level that occurs at an earlier timepoint than morphological changes visible with MRI (129). The combination of [18F]FDG PET and MRI data improves the detection and differentiation of dementia (116). Characteristic uptake patterns of [18F]FDG can differentiate AD from other dementias, and primary Parkinson from atypical parkinsonian syndromes. [18F]FDG PET can also be used for imaging of Huntington disease (HD), amytrophic lateral sclerosis (ALS) and Creutzfeldt-Jakob disease (CJD).

Amyloid PET imaging has been introduced in clinical routine of AD diagnosis and can potentially detect AD pathology earlier than [18F]FDG PET (129, 130). Patients with amyloid positive findings have shown faster cognitive decline, greater likelihood of mild cognitive impairment progression (MCI) to AD, and faster rates of brain atrophy compared to subjects with amyloid-negative findings (106). Amyloid PET has been implemented into the diagnostic criteria of MCI and AD related dementia by the National Institute on Aging-Alzheimer's Association (NIA-AA) (131), and included as a diagnostic AD biomarker by the International Working Group 2 (IWG-2) (132). Tau PET is so far only a research tool, but this may change with the development of tracers (39).

The rapid development of new PET tracers and MRI techniques has the potential to further improve and broaden the diagnostic capabilities of combined PET/MRI in neurology and

establish PET/MRI as a first-line imaging modality in the clinical routine of brain imaging (129).

2 Aims for the thesis

The **overall aim** of this thesis was

> *to evaluate the accuracy of PET/MRI in clinical brain examinations and the potential of this system in the clinical evaluation of dementia and brain metastases.*

Two fulfill this overall aim, three studies were conducted with the following aims.

Paper I

The first study investigated if MRAC is acceptable for clinical brain examinations. This was evaluated in [18F]FDG PET images of patients with suspected dementia. The quantitative accuracy and clinical impact of MRAC were evaluated, with CTAC as reference.

Paper II

The second study was initiated to evaluate if the PET image quality was comparable between PET/MRI and PET/CT. The image quality was evaluated in terms of image contrast and the ability to detect small uptake volumes in a phantom study.

Paper III

The third study evaluated whether amino acid PET can add diagnostic value to MRI in evaluation of brain metastases. The promising AA tracer [18F]FACBC was used and static PET images were evaluated with regards to detection and volume delineation, while uptake characteristics were assessed based on dynamic PET images.

3 Materials and methods

3.1 PET/MRI and PET/CT systems

PET acquisitions in the current thesis were performed on a PET/CT system (Siemens Biograph mCT, Siemens Healthcare, Erlangen, Germany) at St. Olavs Hospital and two PET/MRI systems (Siemens Biograph mMR), one at St. Olavs Hospital, Trondheim University Hospital, and one at the University Hospital of Northern Norway in Tromsø. System specifications are provided Table 1. The PET/MRI and PET/CT system in Trondheim were used for dementia acquisitions in Paper I and for the phantom acquisitions in Paper II. The PET/MRI systems in both Trondheim and Tromsø were used for acquisition of data for the brain metastasis study in Paper III.

Table 1 *System specifications.*

	PET/MRI	PET/CT
System	Siemens Biograph mMR	Siemens Biograph mCT
Software versions	VE11P	Syngo MI.PET/CT 2012A, VG51C
Detector ring diameter	65.6 cm	84.2 cm
Number of PET detector rings	8	4
Number of detector blocks per ring	56	48
Scintillator crystal	LSO	LSO
Crystal size	4x4x20 mm^3	4x4x20 mm^3
Photodetector	APD	PMT
Transaxial FOV	58.8 cm	70 cm
Axial FOV	25.8 cm	22.1 cm
Coincidence window	5.86 ns	4.1 ns
TOF	No	Yes

3.2 Paper I

3.2.1 Image acquisition and reconstruction

Eighteen patients with suspected dementia were included in this study at St. Olavs Hospital in the period May 2017 to June 2018. All patients gave written informed consent, and the study was approved by the Regional Committee for Ethics in Medical Research (REC) (ref. number: 2013/1371). All patients underwent a PET/CT brain examination followed by a PET/MRI brain examination, at 35 ± 1 min and 64 ± 9 min post injection of [^{18}F]FDG, respectively.

The PET and MRI acquisitions were performed simultaneously at the PET/MRI system. The acquired MRI sequences were the same as in the clinical MRI protocol for patients with suspicion of dementia, in addition to sequences for attenuation correction purposes (Dixon VIBE, UTE). PET data from PET/MRI was used for all PET reconstructions and only the CTAC map was utilized from the PET/CT acquisition.

Six PET reconstructions were performed on the PET/MRI system, one with CTAC and five with different MRAC methods, of which three are implemented at the PET/MRI system (1-3) and two are research methods presented in the literature (4-5):

1. $Dixon_{NoBone}$: Segmentation-based MRAC map generated from the Dixon VIBE sequence with four tissue classes: air, fat, fat/soft tissue mix and soft tissue.
2. $Dixon_{Bone}$: In addition to the tissue classes of $Dixon_{NoBone}$, continuous bone information is included from a bone atlas.
3. UTE: Segmentation-based MRAC map generated from the UTE images with three tissue classes: air, soft tissue and bone.
4. UCL: Atlas-based method that generates a pseudo-CT based on a T1-weighted image.
5. DeepUTE: Deep learning-based method to generate pseudo-CT based on UTE images.
6. CT: CTAC map from the PET/CT system imported into the PET/MRI system.

The CTAC map did not cover the neck sufficiently for correction of the PET data from PET/MRI with larger axial FOV. The region with missing attenuation data was therefore substituted with data from the $Dixon_{Bone}$ MRAC map after rigid co-registration. The same substitution was also performed in the other MRAC maps to achieve an equal comparison.

3.2.2 Image analysis

3.2.2.1 Bone artifacts

The Dixon$_{Bone}$ and UTE MRAC maps were visually inspected for bone artifacts as this has been observed after software upgrade of the system.

3.2.2.2 [^{18}F]FDG uptake

The [^{18}F]FDG uptake in the five PET reconstructions with MRAC (PET$_{MRAC}$) was measured in 15 brain regions and compared to the reconstruction with CTAC (PET$_{CTAC}$). The brain regions utilized were taken from a brain atlas in MNI (Montreal Neurological Institute) space and the PET images were transferred to MNI space by registrations to a dementia-specific [^{18}F]FDG PET template. In each brain region, the relative difference was calculated as

$$RD(\%) = \frac{\overline{PET}_{MRAC} - \overline{PET}_{CTAC}}{\overline{PET}_{CTAC}} \times 100, \tag{11}$$

where $\overline{PET}_{MRAC}$ and $\overline{PET}_{CTAC}$ is the average measured activity in the brain region in PET$_{MRAC}$ and PET$_{CTAC}$, respectively. Absolute relative difference was also calculated and average over patients and brain regions ($\overline{RD_{abs}}$).

3.2.2.3 Z-scores

Z-scores were calculated by the software Cortex ID (GE Healthcare, Waukesha WI, USA) in 26 brain regions, by comparison of the patient's PET image to a [^{18}F]FDG PET database of 294 healthy controls divided in six age groups (attenuation corrected by ^{68}Ge transmission scans). The PET uptake is normalized to a reference region not affected by the disease before comparison to the healthy controls. Z-scores both with pons and cerebellum as reference region were exported from Cortex ID for all PET reconstructions. The z-scores obtained from PET$_{MRAC}$ (Z_{MRAC}) were compared to the z-scores from PET$_{CTAC}$ (Z_{CTAC}) by calculating the difference, D, and the absolute difference, D_{abs}, in each brain region as

$$D = Z_{MRAC} - Z_{CTAC} \tag{12}$$

$$D_{abs} = |Z_{MRAC} - Z_{CTAC}|, \tag{13}$$

both for pons and cerebellum as reference regions. D_{abs} was averaged over patients and brain regions ($\overline{D_{abs}}$).

3.2.2.4 Visual evaluation

PET images and z-score maps were clinically evaluated by three nuclear medicine physicians individually in Cortex ID, for a selection of the PET reconstructions. The best and the worst of the clinically implemented MRAC methods based on the z-score analysis were included, in addition to the best of the research MRAC methods, and PET$_{CTAC}$ served as reference. The patients were categorized either as normal or diagnosed with AD, FTD or non-specific pathology based on the PET uptake and z-scores. The physicians were blinded for the AC method and had no MR images or patient history at hand.

A second visual assessment was done by one of the nuclear medicine physicians and a neuroradiologist in conjunction, 2 months after the first visual evaluation. The best of the clinically implemented MRAC methods in the z-score analysis was chosen for this evaluation. MR images were included in addition to PET images and z-score maps in this assessment and was therefore a more clinically relevant setting. Evaluations based on PET$_{CTAC}$ was also performed and served as a reference. Cerebellum was used as reference region for all visual assessments.

3.2.2.5 Statistics

The agreement between PET$_{CTAC}$ and PET$_{MRAC}$ and the inter-reader agreement was calculated by κ-statistics, where a κ value of 0 indicates no agreement better than chance and 1 corresponds to perfect agreement (poor: < 0, slight: 0.00-0.20, fair: 0.21-0.40, moderate: 0.41-0.60, substantial: 0.61-0.80, almost perfect: 0.81-1.00) (133).

3.3 Paper II

3.3.1 Phantom

This study was based on phantom acquisitions with the Esser PET phantom seen in Figure 11. It was equipped with spheres with inner diameters of 4, 5, 6, 8, 12 and 20 mm to represent small uptake volumes. The spheres were filled with radioactivity ($[^{18}F]FDG$) at an activity concentration of 4 and 8 times the background activity in the phantom to simulate different levels of background uptake.
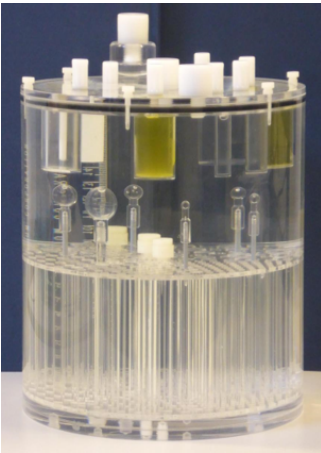
Figure 11 *Esser PET phantom with additional spheres. Image from Øen et al. (134), published under creative commons license CC BY 4.0 (https://creativecommons.org/licenses/by/4.0/).*

3.3.2 Image acquisition and reconstruction

For each activity concentration, a 10 min PET listmode acquisition on PET/MRI was performed prior to a 5 min PET listmode acquisition on PET/CT. CTAC maps from the PET/CT was imported to the PET/MRI and used for attenuation correction on both systems, as MRAC of large water-filled phantoms are prone to artifacts.

Image analyses were performed with PET/MRI and PET/CT reconstructions with the same number of true counts for a balanced comparison of the systems. PET images on the PET/CT were reconstructed from the first 150 s, which is the acquisition time per bed used for clinical applications with this system. An acquisition time of 97 s was used on the PET/MRI system to achieve the same number of true counts. Additionally, for the 8:1 sphere-to-background ratio,

reconstructions with increasing PET acquisition times were performed on both systems to evaluate the contrast and detectability with respect to acquisition time.

PET image reconstructions were done with a range of reconstruction settings to evaluate which settings that provide the best quantitative image quality in terms of contrast, for both PET/CT and PET/MRI. Iterative reconstructions were done with and without PSF, and for PET/CT also with and without TOF. The number of iterations and the pixel size was varied, in addition to the FWHM of the Gaussian post-reconstruction filter.

3.3.3   Image analysis

CRC and CNR were measured for all spheres for the two activity concentrations and for both systems. This was performed with similar pixel size (2×2 mm^2) and 3 iterations on both systems. Furthermore, CNR was evaluated as a function of increasing pixel size, number of iterations and for different filter settings. This was performed for the smallest lesion with CNR > 5 (Rose criterion) in the 8:1 concentration.

For visual evaluation of the detectability, three observers scored all spheres in all reconstructions from 0 to 2. Score 0 was defined as not visible, 1 as visible but comparable to noise and 2 as clearly visible. A sphere was defined as detected if the sum of the scores of the three observers were 3 or higher and no observer set the score 0.

3.4 Paper III

3.4.1 PET/MRI imaging and reconstruction

Eighteen patients in Trondheim (n=11) and Tromsø (n=7) with lesions suspected as brain metastases were included in the [^{18}F]FACBC PET/MRI brain study, a part of the 180ºN (Norwegian Nuclear Medicine Consortium) project, in the period January 2020 to July 2021. All patients gave written informed consent, and the study was approved by REC (ref. number: 2018/2243). The patients' primary cancers were lung cancer (n=9), gastrointestinal cancer (n=5), malignant melanoma (n=2), breast cancer (n=1), and thyroid cancer (n=1). Four patients (4 lesions) had prior surgical resection and four patients (6 lesions) had prior stereotactic radiotherapy in the same location as the suspected lesion.

A 35 min (30 min for two patients) PET brain listmode acquisition was acquired from the time of [^{18}F]FACBC injection, simultaneously with MRI acquisitions, including ce-MRI. Due to technical problems with the PET/MRI system, one patient was examined with PET/CT and had a separate MRI examination the same day.

Static (last 15 min) and dynamic PET images were reconstructed with DeepUTE MRAC since this was the best MRAC method in Paper I (CTAC on the PET/CT).

3.4.2 Image analysis

The PET and MRI images were evaluated by a nuclear medicine physician and a neuroradiologist at each hospital and brain lesions were identified. The lesions were divided in two groups based on previous treatment with SRS (SRS group) or not (noSRS group). The MRI interpretation differed for the two groups as radiation necrosis also show contrast enhancement. In the noSRS group, lesions were categorized as "MRI positive" if they showed contrast enhancement and were not present on previous MRIs (or if no previous MRI was available). In the SRS group, the lesions were categorized as "MRI positive" if showing contrast enhancement and progressive enlargement compared to previous MRIs. If the lesions were stable or decreased in size, they were categorized as "MRI negative". A follow-up status of the lesions in the SRS group was assessed based on MRI scans subsequent to the PET/MRI examination. Lesions were defined as detected on PET if the [^{18}F]FACBC uptake was distinctly different from surrounding tissue.

Maximum SUV was measured in the lesions (SUV_{max}) and mean SUV in crescent-shaped VOIs in normal brain parenchyma (SUV_{mean}). TBR was also calculated and defined as SUV_{max} divided by SUV_{mean}.

Tumor volumes were defined in ce-MRI (V_{MRI}) and PET (V_{PET}) images. In MRI, manual delineation of contrast-enhanced regions was performed, with inclusion of necrotic areas inside lesions. PET volumes were defined by a threshold of 41% of maximum tumor uptake, with manual modifications to include necrotic areas inside lesions and to exclude non-tumor tissue (e.g., veins). The maximum diameter ($D_{max\ MR}$) of the MRI volume in any direction was automatically extracted. Furthermore, the spatial similarity of the PET and MRI volumes was determined by the Dice similarity coefficient (DSC)

$$DSC = \frac{2(V_{MRI} \cap V_{PET})}{V_{MRI} + V_{PET}} \tag{14}$$

In the dynamic analyses, only PET detected lesions with $D_{max\ MR}$ larger than 10 mm were included due to poor recovery of small lesions in PET images. Time-activity curves were generated for SUV_{max} and SUV_{mean}. The curve for SUV_{max} was assigned to one of the following slopes: (I) constantly increasing uptake without identifiable peak, (II) uptake peaking early followed by a plateau, and (III) uptake peaking early followed by a constant decrease.

3.4.3 Statistics

The Wilcoxon rank sum test was used to test differences between PET and MRI volumes. Spearman's rho (r_s) was calculated to investigate the correlation between the volumes.

4 Results

4.1 Paper I

4.1.1 Bone artifacts

Bone artifacts were observed in 4 of 18 of the $Dixon_{Bone}$ MRAC maps. In two cases where large bone segments from other parts of the body were present in the MRAC map of the brain, an additional Dixon sequence was acquired, resulting in artifact-free MRAC maps. In the two other cases the artifacts were positioned outside the head and was removed manually.

In 16 of 18 UTE MRAC maps, minor bone artifacts were present inside the brain close to the anterior ventricles and was not removed since they are not possible to remove in clinical routine.

4.1.2 [^{18}F]FDG uptake

The [^{18}F]FDG brain uptake with the five different MRAC methods was evaluated and compared to CTAC. The average absolute difference in [^{18}F]FDG uptake between PET_{MRAC} and PET_{CTAC} was smallest for the research method DeepUTE ($\overline{RD_{abs}} = 2.2 \pm 1.5$ %). $Dixon_{NoBone}$, the only MRAC method without bone information, produced the largest deviations from CTAC ($\overline{RD_{abs}} = 7.1 \pm 3.7$ %). $Dixon_{Bone}$ had the smallest difference to CTAC among the clinically implemented MRAC methods ($\overline{RD_{abs}} = 2.5 \pm 2.4$ %). The result for $Dixon_{Bone}$ were comparable to the research methods, but with increased variation.

4.1.3 Z-scores

Z-scores based on PET images with the five different MRAC methods were also compared to z-scores based on PET_{CTAC}. Using cerebellum as reference region caused decreased differences between Z_{MRAC} and Z_{CTAC} compared to using pons. The research MRAC methods produced z-scores close to those obtained with CTAC (DeepUTE: $\overline{D_{abs}} = 0.15 \pm 0.11 \ \sigma$, $\overline{D_{abs}}$ = UCL: $0.15 \pm 0.12 \ \sigma$). Among the clinically implemented MRAC methods, DixonBone provided the smallest difference to CTAC in z-scores ($\overline{D_{abs}} = 0.23 \pm 0.20 \ \sigma$) and PET_{UTE} the largest difference ($\overline{D_{abs}} = 0.54 \pm 0.40 \ \sigma$).

4.1.4 Visual evaluation

In the first visual evaluation based on PET images and z-scores, the included reconstructions were $PET_{DeepUTE}$, $PET_{DixonBone}$, PET_{UTE} and PET_{CTAC}. The agreement in diagnosis between PET_{CTAC} and $PET_{DeepUTE}$, $PET_{DixonBone}$, and PET_{UTE} was 74%, 67% and 70% in average for the three readers, respectively. PET_{MRAC} agreed *moderately* with PET_{CTAC} according to κ-statistics for most MRAC methods and readers. The inter-reader agreement was low (*fair* for PET_{CTAC} and *slight* for PET_{MRAC}), indicating that [18F]FDG PET evaluations of dementia without MRI and clinical information are highly subjective.

A second visual evaluation including MRI was therefore included, and $PET_{DixonBone}$ was chosen since it was the best of the clinically implemented MRAC methods in the z-score analysis. The agreement in diagnosis between PET_{CTAC}+MRI and $PET_{DixonBone}$+MRI increased to 89% and *almost perfect* agreement according to the κ-statistics.

The quantitative accuracy and clinical impact of one of the clinically implemented MRAC ($Dixon_{Bone}$) was found to be acceptable for clinical brain examinations, although the performance was improved for the research MRAC methods in the z-score calculations.

4.2 Paper II

In general, a slightly higher contrast was found for PET/CT compared to PET/MRI quantitatively. For both systems 2 iterations, the smallest pixel size (<2 mm) and the postfilter with 4 mm FWHM provided the highest contrast in terms of CRC and CNR.

For the reconstructions with similar number of true counts for the two systems, the 5 mm and the 6 mm spheres were the smallest detected spheres in the 8:1 activity ratio for the PET/CT and PET/MRI, respectively. With higher background activity (4:1), the 8 mm sphere was the smallest detected sphere for both systems. For an increased acquisition time (3 min) the 5 mm sphere was also detected with PET/MRI for the lowest background ratio, while for PET/CT a 2 min acquisition time was required.

The PET image quality for PET/MRI in terms of contrast and detectability was comparable to that of PET/CT, although for an increased acquisition time.

4.3 Paper III

In the noSRS group, twenty-nine lesions were categorized as "MRI positive" of which 19 (66%) were detected with PET. The PET detected lesions had in general high $[^{18}F]$FACBC uptake and TBR (mean SUV_{max}: 4.2 ± 2.2, mean TBR: 12.0 ± 6.5), and a diameter equal to or larger than 7 mm. The PET undetected lesions showed low $[^{18}F]$FACBC uptake (mean SUV_{max}: 0.6 ± 0.3, mean TBR: 1.6 ± 0.6) and had a diameter equal to or smaller than 8 mm.

Six lesions were identified in the SRS group, 4 lesions categorized as "MRI positive" and 2 lesions as "MRI negative". All six lesions had $[^{18}F]$FACBC uptake and were detected with PET (mean SUV_{max}: 3.2 ± 1.1, mean TBR: 8.4 ± 3.2). The two patients with "MRI positive" lesions deceased 5 months after the PET/MRI examination. The "MRI negative" lesions remained stable at follow-up (10 and 7 months after PET/MRI), but one of the patients had 7 new brain lesions.

Lesions from all included primary cancers showed $[^{18}F]$FACBC uptake, and no difference was observed in the uptake between the groups of different primary cancers.

The PET and MRI volumes of the PET detected lesions were not significantly different and correlated significantly, but the spatial localization of the PET and MRI volumes differed to some degree (mean DSC: 0.66 ± 0.18).

In the dynamic analyses of the noSRS group, 6 lesions had a TAC defined as *plateau* (slope II) and 8 lesions had a *decreasing* curve (slope III). In the SRS group, one lesion had a TAC curve categorized as slope III (in a patient who deceased 5 months later) and the remaining five lesions had a slope II. No lesions were assigned with an increasing curve (slope I).

$[^{18}F]$FACBC PET showed in general high contrast for brain metastases, but for small lesions the uptake was low and detection inferior compared to MRI. Whether $[^{18}F]$FACBC PET can differentiate recurrent brain metastases from radiation necrosis should be further evaluated. The results indicate that $[^{18}F]$FACBC may detect tumor tissue beyond the volume defined by ce-MRI, which should be further investigated.

5 Discussion

This thesis has been a part of an initiative to implement PET/MRI in clinical practice in Trondheim and Norway, with focus on brain applications. The quantitative accuracy of brain MRAC methods was evaluated and found to be acceptable for one of the clinically available methods, while further improved with the research methods applied. Additionally, the PET image quality was evaluated experimentally for PET/MRI and compared to the PET/CT system. The contrast and detectability of the PET/MRI system were slightly inferior to the PET/CT system. However, uptake volumes as small as 5 mm in diameter were detected with both systems, but for an increased acquisition time for PET/MRI. Subsequent to assurance of proper image quality and accuracy, the diagnostic value of [18F]FACBC PET in evaluation of brain metastases was assessed. [18F]FACBC uptake was observed in metastases from different origins (lung, malignant melanoma, gastrointestinal tract, breast, thyroid). However, the detectability of small metastases was found to be inferior compared to MRI. The results indicate that [18F]FACBC PET might detect tumor tissue beyond contrast enhancement on MRI, which could improve accuracy of tumor delineation and increase precision of surgical resection and radiotherapy. The accuracy of [18F]FACBC PET to differentiate recurrence of brain metastases from radiation necrosis could not be determined based on our results and should be further investigated.

5.1 MRAC

Uncertainty around the quantitative accuracy of attenuation correction on PET/MRI has been the main reason for limited use of PET/MRI at St. Olavs Hospital and worldwide. The evaluation of the dementia patients in paper I showed that segmented MRAC with atlas-based inclusion of bone (Dixon$_{Bone}$) performed the best among the current clinically implemented methods on the Siemens PET/MRI system when compared to CTAC. Dixon$_{Bone}$ posed a small but acceptable deviation from CTAC on average. However, regional deviations up to 13% in [18F]FDG uptake and 1.4 σ in z-score occurred for single patients, which could impact the clinical evaluation. Furthermore, large bone artifacts occurred for some patients, which means that radiographers must be aware of this and acquire a new Dixon sequence if this is observed. The two research MRAC methods generating a pseudo-CT, based on a database of CT and MRI pairs (UCL) or deep-learning algorithms (DeepUTE), improved the quantitative accuracy

although regional deviations from CTAC up to 10% in [^{18}F]FDG uptake and 0.6 σ in z-score were found for single patients. The number of patients in our study is limited, but the results are comparable to a study by Ladefoged et al. (98) including 104 dementia patients where deviations up to 15% for Dixon$_{Bone}$ and 5% for DeepUTE in [^{18}F]FDG uptake were observed compared to CTAC.

In brain tumor patients, quantitative evaluations of the three clinical MRAC methods at the Siemens PET/MR system (Dixon$_{NoBone}$, Dixon$_{Bone}$ and UTE) showed best agreement with CTAC for Dixon$_{Bone}$ with a mean TBR bias of -3% (135). However, large deviations from CTAC were observed for single lesions for all methods. The atlas-based and ZTE MRAC methods implemented at the GE PET/MRI system have also demonstrated good agreement with CTAC, with mean TBR bias within 2.4% (136). For evaluation of TAC characteristics in dynamic [^{18}F]FET imaging of brain tumors with VOIs centered at SUV$_{max}$, no changes in TAC pattern and minor changes in time to peak were found for the Siemens MRAC methods (137).

Although our results and other studies show that MRAC can cause quantitative local biases due to incorrect tissue classifications both in patients with dementia and brain tumors (79, 135), the diagnosis and clinical impact on brain examinations may not be significantly affected. In the clinical evaluation in paper I, high agreement (89%) between PET$_{CTAC}$+MRI and PET$_{DixonBone}$+MRI was found, and the two cases of discrepancies were caused by different subtypes of dementia. The atlas-based and ZTE MRAC methods implemented at the GE PET/MRI system have also shown diagnostic accuracy similar to CTAC for diagnosis of AD (138-140). When it comes to brain tumor imaging, the diagnostic reading also remained unchanged for the three Siemens MRAC methods (Dixon$_{NoBone}$, Dixon$_{Bone}$ and UTE) compared to CTAC despite quantitative deviations (135).

Summarized, the impact in clinical practice seems to be negligible for the best performing MRAC methods both in dementia and in brain tumors. Guidelines for brain imaging with both [^{18}F]FDG and AA PET now includes PET/MRI and recommends the latest versions of MRAC methods that includes bone (40, 141). But although the problem with attenuation correction for brain PET/MRI imaging can be considered solved, clinical implementation of improved research MRAC methods is still warranted. Siemens is now working on implementation of DeepDixon MRAC on the PET/MRI system. This method is based on the same algorithm as DeepUTE but with Dixon images as input data and has shown comparable results to DeepUTE (98).

5.2 PET image quality

5.2.1 PET/MRI vs PET/CT

In addition to quantitative accuracy, the PET image quality is of high importance, especially for detection of small lesions in oncology. The contrast was in general slightly inferior for PET/MRI compared to PET/CT in Paper II. The small difference in contrast was only partly due to the TOF capability on PET/CT. The remaining difference could be caused by increased scatter (~1 percentage points (pp)) and randoms (~5 pp) for PET/MRI compared to PET/CT, as these events cause noise in the image and reduces the contrast. The difference in scatter and randoms could originate from higher activity (13-14%) in the phantom at scan start at the PET/MRI system, as the same phantom was used at both systems and first scanned at the PET/MRI. However, an increased scatter fraction (~2 pp) for the PET/MRI system was also found in an earlier study by our group, when the activity concentration was higher at the PET/CT (24). Another explanation can be more random events at the PET/MRI due to the longer coincidence window compared to PET/CT.

A 1 minute (50%) increase in acquisition time for PET/MRI compared to PET/CT was required to detect the 5 mm sphere in the low background activity concentration. A smaller time difference could potentially be achieved if smaller time increments than 1 min had been used.

The difference in image quality between the two systems may be increased in body regions with larger diameter, like the abdomen. The amount of scatter and randoms is then increased and the effect of TOF is improved. Nevertheless, the size of the phantom in Paper II is representative for brain imaging and PET image quality comparable to PET/CT was achievable for brain PET/MRI with an increased acquisition time. Increased acquisition time can however be a problem in hospitals with high patient through-put and tight time schedules, but for PET/MRI protocols, which often have a longer scan time compared to PET/CT, this should not be a problem.

5.2.2 Pixel size, noise and filter

CNR increased with decreasing pixel size in our phantom study, with an enhanced effect for PET/CT compared to PET/MRI. This difference may originate from the slightly degraded image quality and increased noise level of PET/MRI. Small voxels may improve detection of

small lesions, but also tends to introduce more false positive results due to low counting statistics and increased noise (142). In nuclear medicine imaging there is always a balance between spatial resolution and noise. Noise also affect SUV values, and especially SUV$_{max}$. Post-reconstruction filtering will reduce noise, but also limits the detectability. It could be that a post-reconstruction filter of 4 mm FWHM hampered detection of the 4 mm sphere in Paper II, but a 2 mm FWHM filter or all-pass filter did not improve visual detection and slightly decreased CNR. Based on these considerations, a 4 mm filter and 2 mm pixel size was used in the clinical study of Paper III.

5.2.3 Detectability

The spatial resolution is limited in PET imaging and inferior to MRI. In Paper III brain metastases as small as 3 mm were detected with ce-MRI and were probably false negative on PET due to the limited spatial resolution. The smallest sphere detected with PET in the phantom study (Paper II) had a diameter of 5 mm. The 4 mm sphere was not detected for increased acquisition times for any of the systems, and the increase in CNR with time was low compared to the 5 mm sphere. This indicate that the 5 mm sphere is the smallest sphere possible to detect visually with the current systems within general clinical scan times and activity concentrations. The detectability of the same PET/CT system has also been investigated in a phantom study by Adler et al. (143). They detected a 4 mm sphere for an 8 min acquisition, but with a 15:1 activity ratio, which is almost twofold of the highest activity ratio used in our study. In neuro-oncology PET such high activity ratios might be achieved for a tracer with high TBR, such as [^{18}F]FACBC in a study of high-grade gliomas (144).

The use of human observers for detection of the spheres in Paper II may have affected the results as visual detection is subjective. However, this is representative for clinical assessments and the inter-reader agreement of the three observers was high. In the study by Adler et al. (143), a 8 min acquisition was required to detect the 5 mm sphere with 7.5:1 activity ratio (not detected for a 1, 2 or 4 min acquisition). In our study the same sphere was detected with a 2 min acquisition in the 8:1 activity ratio. This discrepancy was likely due to their higher threshold for definition of detectability. Our threshold was set to evaluate if the sphere was observable and not whether it would change the course of the treatment if it was a lesion as for Adler et al.

The smallest detected lesion in the clinical study (Paper III) had a maximum diameter of 7 mm. TBR for the 7 mm metastasis was 3.9 and hence equivalent to the 4:1 sphere-to-background ratio in Paper II, where the 8 mm sphere was the smallest detected sphere. A 7 mm sphere was not included in the phantom but could potentially have been detected. These comparable results indicates that the phantom study is representative for clinical PET/MRI imaging and that a higher TBR can improve detection of smaller lesions in clinical imaging. This can be achieved with a tracer with higher difference in uptake between tumor and normal brain, or for improved spatial resolution that will reduce partial volume effects. The low measured [^{18}F]FACBC uptake in small brain metastases ($\leq$ 8 mm) in Paper III was likely low due to partial volume effects, and smaller lesions could probably have been detected with improved spatial resolution.

5.2.4   PET image quality in the future

Physical and technical development of the PET systems can improve the spatial resolution and the detectability. The PET image quality is improved in more recent systems compared to the systems used in our studies and will likely further advance in the future. Mainly due to decreased detector element size, which improves spatial resolution, and increased timing resolution that improves the effect of TOF and hence reduces noise. The most recent PET/MRI system, produced by United Imaging Healthcare, probably have the smallest detector element size of current PET systems, which is 2.76 mm. This results in an axial and transverse spatial resolution of 2.72 mm and 2.84 mm FWHM at 1 cm radial offset (145), compared to 4.1 mm and 4.0 mm FWHM on the Siemens PET/MRI (24). Such an improvement in spatial resolution will likely enable detection of significantly smaller lesions in clinical practice. Partial volume effects will be reduced, which will improve activity recovery and TBRs. PET imaging in neurodegenerative diseases is also biased due to partial volume effects, and will also benefit from improved spatial resolution (146).

In contrast to the Siemens PET/MRI system, the systems by GE and United Imaging Healthcare offer TOF, with timing resolution of < 400 ps and 450 ps, respectively (78, 147). In recent years there have been large improvements in timing resolution with the introduction of fast SiPM detectors. The best coincidence timing resolution in a PET system today is 214 ps and it may be below 100 ps in the future (148). A timing resolution of 214 ps constrains the

annihilation event to a segment of 3.2 cm along the LOR and cause an increase in SNR of 2.5 compared to a system without TOF (25).

A further increase in SNR can be obtained with larger axial FOV. The intrinsic sensitivity is then increased as annihilation photons with a larger angle are detected (142). The Siemens PET/MRI system has an axial FOV of 25.8 cm, while it is increased to 32 cm in the newest PET/MRI system by United Imaging Healthcare (145). For PET/CT, total body (TB) systems have been developed with axial FOV of 1 and 2 m. Combined with great TOF performance this results in excellent effective sensitivity (142). These TB systems have a 13-times higher sensitivity compared to the Siemens PET/MRI system, which cause a 3.6-time increase in SNR (24, 149). This results in reduced background noise and improved contrast. The extended geometry also increases the number of detected events for a single bed position, although not to the same degree as for whole-body imaging (10). A TB PET/MRI system has not yet been announced. A simultaneous TB PET/MRI would require a large homogeneous magnetic field, compared to the typically MR FOV today that is around 50-55 cm (149). Furthermore, MR imaging with a large FOV will be extremely time consuming, hence MRI and PET/MRI are probably best suited for smaller body regions like the brain. But although TB PET/MRI may not be feasible, a larger PET FOV is preferable also for brain PET/MRI examinations.

5.2.5 Improvement of reconstruction algorithms

The number of iterations in iterative reconstruction algorithms also impact the image quality. Noise is increased with the number of iterations and in Paper II we observed that CNR decreased for more than 1-3 iterations (dependent on system and reconstruction algorithm). Three iterations were used in Paper III based on the results of Paper II and prior NEMA performance measurements by our research group (24). Further development of reconstruction methods is likely to further improve the PET image quality. Bayesian penalized likelihood (BPL) algorithms have been introduced in clinical systems, which provides convergence with increasing OSEM iterations without amplifying noise. This is achieved by incorporation of a penalty term with prior knowledge in the iterative updates, like minimizing large intensity differences in neighboring voxels that likely represent noise (142). In a recent brain phantom PET/MRI study, BPL reconstructions showed improved contrast recovery, better spatial resolution and SNR compared to OSEM with TOF (150). However, background variability and

uniformity were inferior for BPL. Nevertheless, BPL reconstructions show promising results for noise reduction and improved lesion detection in clinical PET imaging in general (151-155). BPL algorithms are computational intensive and deep-learning algorithms have been purposed for obtaining faster BPL reconstructions from OSEM images (156). The development of artificial intelligence in image reconstruction will likely also contribute to improved PET image quality in the future (142).

5.2.6 Motion correction

With increased image quality, blurring caused by patient motion will be more prominent (142). Motion correction algorithm was not applied in our studies due to bugs in the software implemented at the systems. This potentially affected the detectability in Paper III, but the results were comparable to the phantom study not affected by motion. A variety of research based motion correction methods for brain PET imaging exists, but clinical use is still hampered by the absence of proper methods on commercial systems (142).

5.2.7 Summary

It will be interesting to see to what degree the combination of recent and future developments in detectors, axial coverage, reconstruction algorithms and motion correction will revolutionize the PET image quality in the future. This will improve both visual detection limits and confidence of physicians, as well as the accuracy of tumor delineation and PET metabolic information when used in stereotactic radiotherapy and surgery planning. Improved image quality can also be exploited for reduced activity or scan time.

5.3 PET/MRI in neurodegenerative diseases

The prevalence of neurodegenerative diseases rise continuously with increasing life expectancies (39). In 2021, 55 million people were affected by dementia worldwide and the number increases by nearly 10 million people every year according to the World Health Organization (157). Dementia is a clinical diagnosis that earlier has been based on clinical history and symptoms, while MRI has been used to exclude other diseases (39). However,

neuroimaging now plays an increasing role for earlier diagnosis and investigating the pathophysiology of the diseases that is not yet fully understood. Development of advanced MRI techniques, such as diffusion tensor imaging (DTI), fMRI, and perfusion imaging, are considered to improve dementia diagnosis (129), but there is also a large potential for PET in this field. The fact that MRAC is acceptable for brain applications makes PET/MRI an excellent imaging modality for this patient group.

[^{18}F]FDG PET is increasingly used to support MRI with metabolic information and differentiation of age-related changes from early stages of dementia or other neurodegenerative processes. Additionally, specific patterns of hypometabolism can diagnose subtypes of dementia (60).

The use of PET is likely to further increase in this patient group with the introduction of amyloid PET in the clinic and further research on tau tracers. Cognitively unimpaired persons with both positive amyloid and tau biomarkers have shown faster cognitive decline than persons with no or only one positive biomarker (39). Amyloid and tau PET imaging can therefore contribute to earlier diagnosis of AD, but also other neurodegenerative diseases, and hopefully contribute to development of therapeutics for this patient group (39, 158).

5.4   PET/MRI in neuro-oncology

PET is also increasingly used in neuro-oncology in combination with MRI. AA PET has improved the visibility of brain tumors compared to [^{18}F]FDG PET and is recommended in international guidelines for imaging of gliomas (40, 43). As mentioned earlier, AA PET has shown higher diagnostic accuracy compared to MRI in differentiation of glioma and non-neoplastic lesions or treatment-related changes, in glioma grading, and in assessment of treatment response, as well as superior tumor delineation (43). For brain metastases ce-MRI is the recommended imaging modality for detection and tumor delineation of metastases, while AA PET is found useful for differentiation between recurrence and radiation necrosis although the literature is still limited (71).

5.4.1.1 Detectability of brain lesions using [18F]FACBC

The low normal brain uptake of [18F]FACBC and increased TBR for brain tumors compared to other AA tracers was expected to improve detection of small brain metastasis studied in Paper III (52, 53, 55, 58, 59, 144, 159-161). However, we did not detect smaller brain metastases with [18F]FACBC than what was detected using [18F]FET in a study by Unterrainer et al (160). They found [18F]FET-positive metastases with a diameter down to 6 mm on ce-MRI, even smaller than in our study. The metastases were defined as [18F]FET-positive based on a threshold of TBR ≥ 1.6, according to guidelines for glioma imaging. No such guideline exist for [18F]FACBC, and visual detection with uptake distinctly different from surrounding tissue was applied in our study. This difference may have caused the detection of smaller metastases by Unterrainer et al. compared to our study.

Lesions smaller than the PET spatial resolution has been detected in a [18F]FACBC study of relapsing and recurrent high-grade glioma by Bogsrud et al. (144). The detected lesions had diameters down to 3 mm measured on PET and estimated lesion sizes to below 2 mm. TBR was high (4-18) and probably the reason for the detection of such small lesions. In AA PET studies including both brain metastases and gliomas, TBR tends to be lower for brain metastases (159, 162). This may explain why we do not detect such small brain metastases with [18F]FACBC PET as detected for gliomas. However, this must be confirmed in larger studies.

Paper III showed that the excellent spatial resolution of MRI and distinct contrast enhancement of brain metastases makes it the preferred modality also over [18F]FACBC PET in detection of brain metastases. Although ce-MRI is the most sensitive modality for detection of brain metastases according to the PET-RANO working group (71), the literature is however limited on the actual sensitivity of ce-MRI for detection of brain metastases. According to mouse model studies, not all brain metastases show contrast enhancement due to nonpermeability of the BBB (163, 164). Based on these observations and the fact that [18F]FACBC can be transported across the BBB by amino acid transporters, brain metastases without contrast enhancement could potentially be present and identified with [18F]FACBC PET only. However, this was not observed in our study and has to my knowledge not been reported in other AA PET studies on brain metastases in humans.

5.4.1.2 Spatial incongruence

The results of Paper III indicated that [^{18}F]FACBC PET might detects tumor tissue beyond the contrast enhancement as only partial spatial congruence was observed between PET and ce-MRI volumes. The validity of this result can however be discussed as no guidelines exists on tumor delineation using [^{18}F]FACBC. A threshold-based delineation (41% of SUV_{max}) was applied in this study based on visual evaluations. This threshold is recommended for defining metabolic tumor volume in [^{18}F]FDG tumor imaging, and may not be valid for [^{18}F]FACBC due to different uptake mechanisms of the two tracers. Studies based on image-localized biopsies should be conducted to determine procedures for tumor delineation with [^{18}F]FACBC. However, a [^{18}F]FET study on brain metastases has also observed spatial incongruence of PET and MRI volumes (165) and further investigations are needed to determine whether AA PET can detect metastatic tissue beyond volumes defined by ce-MRI, as confirmed for gliomas (54, 56, 166-168). AA PET may improve delineation of radiotherapy target volumes of gliomas compared to conventional MRI, but the literature is still limited and the potential benefit for the patients is not yet known (169). If tumor tissue identified by AA PET beyond contrast enhancement is histologically confirmed also for brain metastases, the value of AA PET in radiotherapy planning of brain metastases should be investigated. Improved tumor delineation will increase the tumor dose and reduce the dose exposure of healthy tissue. Dose escalation based on AA PET may also improve the effect of radiotherapy, but the literature is limited and contradictory in this field (170-172).

5.4.1.3 Treatment-related changes vs recurrence

Radiotherapy and chemoradiation (radiotherapy combined with chemotherapy) may cause pseudoprogression or radiation necrosis, which makes recurrence evaluations based on MRI challenging (173). Pseudoprogression mimics tumor progression, but the difference is that the increase in size of contrast-enhancing lesions, or new contrast-enhancing lesions, resolve without additional treatment (174). Radiation necrosis also show contrast enhancement and is difficult to distinguish from true tumor tissue. Pseudoprogression typically occurs within 12 weeks after radiotherapy completion, while radiation necrosis normally occurs more than 6 months after radiotherapy and up to several years later (173). Advanced MRI (aMRI) methods, such as DWI and PWI, have been investigated to overcome the limitations of conventional MRI in identifying such contrast-enhancing treatment-related changes. However, the results

are controversial (125). On the contrary, AA PET ($[^{11}$C]MET, $[^{18}$F]FDOPA, $[^{18}$F]FET) has shown difference in TBR between treatment-related changes and recurrence, which can be exploited for diagnosing recurrence. High and improved diagnostic accuracy has been shown for AA PET compared to aMRI in differentiation of treatment-related changes and recurrence for both gliomas and brain metastases (71, 173, 175). The accuracy may be further increased with $[^{18}$F]FET PET when combining TBR with dynamic TAC parameters like time-to-peak and slope characteristics (48, 51, 52, 125).

In our study of brain metastases, $[^{18}$F]FACBC uptake was present in all six previously radiated lesions, including two lesion indicative of radiation necrosis based on follow-up MRI. SUV_{max} was above 1.3 for all lesions, which was proposed as a threshold for recurrence of brain metastases with $[^{18}$F]FACBC by Parent et al. in a study of 8 patients (59). All lesions had a TAC curve with early peak followed by a plateau or decrease indicative of tumor tissue according to TAC characteristics in dynamic $[^{18}$F]FET imaging. Due to the small group of patients treated with SRS in our study, as well as the lack of histopathology and the limited follow-up time with MRI no conclusions on the role of $[^{18}$F]FACBC PET in evaluation of radiation necrosis and recurrence of brain metastases can be made based on our results. Furthermore, it is not yet known whether TAC curves obtained with $[^{18}$F]FACBC shows the same characteristics as $[^{18}$F]FET and whether dynamic $[^{18}$F]FACBC uptake can differentiate recurrence and treatment-related changes. Larger studies with histopathology or long follow-up are needed to determine the diagnostic accuracy of $[^{18}$F]FACBC PET for this purpose.

5.4.1.4 New tracers

Development of new tracers for neuro-oncology can further improve PET imaging and treatment of brain tumors. Tracers with even higher TBR for brain metastases could provide earlier detection of brain metastases. Prostate-specific membrane antigen (PSMA) labeled with gallium-68 ($[^{68}$Ga]PSMA) has recently shown extremely low uptake in normal brain (SUV_{max} < 0.23) and very high TBR (median: 152) in glioma (176). Cases with $[^{68}$Ga]PSMA/$[^{18}$F]PSMA uptake in brain metastases have also been observed and allowed for detection of brain metastases not identified with MRI (177-182).

In addition to $[^{18}$F]FACBC, another amino acid tracer, α-$[^{11}$C]-methyl-L-tryptophan ($[^{11}$C]AMT), has shown promising results for brain tumors. Although the literature is still

limited, [11C]AMT has shown a strong prognostic value for glioma in addition to promising results for tumor delineation and diagnosis of treatment-related changes (44).

5.4.1.5 Theranostics

Theranostics, the combination of therapeutics and diagnostics, is an emerging field in cancer management where PET will play an important role. Diagnostic PET (or SPECT) imaging can identify whether target receptors are present on cancer cells. If so, the patient can receive radionuclide therapy based on the same PET tracer but with different isotopes that cause a locally delivered radiation dose to the cancer cells. Additionally, post-therapeutic imaging can be used for dosimetry calculations. Theranostics has successfully been implemented for thyroid cancer, neuroblastoma, metastatic prostate cancer and neuroendocrine tumors (183-186). For prostate cancer for instance, ^{68}Ga and Lutetium-177 (^{177}Lu) can be labeled to PSMA for diagnostics and therapeutics, respectively. No clinical theranostic approaches have been established for gliomas or brain metastases, but as gliomas have shown to be PSMA-avid this is a potential therapeutic target agent also for gliomas (187). Two case reports have shown the feasibility of targeted radionuclide therapy with [^{177}Lu]PSMA of glioblastoma multiforme (188, 189). This opens the possibility for theranostics also for brain tumors and increased treatment options for a patient group with limited treatment options (176).

5.4.1.6 Summary

Although no added diagnostic value of [^{18}F]FACBC PET to MRI in the evaluation of brain metastases has yet been shown, the potential in tumor delineation, radiotherapy planning and recurrence evaluations should be further explored. Other AA tracers, like [^{18}F]FET, likely improves recurrence evaluations of brain metastases and AA PET improves diagnosis of gliomas compared to MRI. PET/MRI is hence a well-suited imaging modality in neuro-oncology as PET can add complementary metabolic information in situations where MRI is limited. PET/MRI can potentially improve treatment planning of radiotherapy and surgery and be a well-suited imaging modality for theranostics in the future.

5.5   Limitations of PET/MRI

The disadvantages of PET/MRI is the high cost and limited availability compared to PET/CT. PET/MRI benefits over PET/CT in reduced radiation dose, however AI-based reconstruction for reducing CT dose is now clinically introduced and this advantage may diminish in the future (149). The longer acquisition time of MRI compared to CT is also often highlighted as a limitation of PET/MRI, but this is mostly an issue for whole-body acquisitions. For brain applications, the patients need an MRI examination anyway and will rather benefit from a simultaneous PET/MRI examination as PET data will be acquired at the same time as the MRI data.

In whole-body imaging, the introduction of TB PET/CT systems in clinical routine will enable considerable decrease both in injected activity and acquisition time, meanwhile maintaining or even improving image quality. TB PET/MRI is as mentioned not feasible in the same way. However, current PET/MRI systems is convenient for brain imaging with one bed position and for the purpose of providing complementary information to an MRI examination.

5.6   Synergy of PET and MRI

PET/MRI benefits from synergy effects, meaning that the combination of the two modalities is improved compared to each of the modalities alone. In dementia assessment for instance, the accuracy of differentiation of AD, FTD and controls by automatic classification increased from 73% and 81% for MRI and [^{18}F]FDG PET, respectively, to 92% for the combination of MRI and PET data (116). Furthermore, neuro-oncology studies on AA PET and aMRI have shown that AA PET is superior to DWI and PWI in tumor detection, predicting recurrence and survival, and diagnosing progression in glioma imaging, but the performance was further improved for the combination of AA PET and DWI or PWI (175). Another example is a study on the ability of [^{18}F]FET PET/MRI radiomics to differentiate radiation injury from recurrent brain metastasis (190). A diagnostic accuracy of 81% for ce-MRI and 83% for [^{18}F]FET PET was found, while for the combination of the two modalities the accuracy reached 89%. These examples show that PET and MRI provide complementary information and that future research should focus on the effect by combining data from the two modalities.

Multi-modal imaging provides new opportunities as complementary information can be obtained in one examination and accurately aligned, and especially for simultaneous acquisitions possible with integrated PET/MRI systems. Simultaneous acquisition excludes variations due to biological processes and enables temporal and spatial matching of MRI and PET data. This can be exploited for purposes like MR-based motion correction (191-195) and partial volume corrections (196-198), as well as incorporation of anatomical information in the PET image reconstruction (199, 200). Such advances can make improvements in the PET image quality not possible with PET/CT due to the non-simultaneous acquisition of PET and CT data as well as poor soft tissue contrast of CT.

5.7 Outlook

Based on the two first papers of this thesis as well as other literature, it can be concluded that PET/MRI is applicable for brain examinations. The inaccuracies with MRAC are solved to an acceptable degree for the brain and the PET image quality is comparable to that of PET/CT for brain examinations. MRI is the standard imaging modality for this body region, and the field of neurology is well suited to explore the potential of PET/MRI.

At St. Olavs Hospital today, assessments of patients with suspected dementia are performed on the PET/MRI system as a result of Paper I. The DeepUTE method is used for attenuation correction, with AC maps generated offline. DeepDixon was recently installed as a work-in-progress sequence at our PET/MRI system at St. Olavs Hospital as one of two sites worldwide, and we will test this sequence on our neurological PET/MRI examinations. Hopefully, this method will become available for clinical use within the end of 2022.

A nuclear medicine multicenter project, Norwegian Nuclear Medicine Consortium (180°N), was started in Norway in 2020, funded by Trond Mohn. The project includes the hospitals and universities in Trondheim, Bergen and Tromsø, all of which have installed the same Siemens PET/MRI system. 180°N consists of three projects, one on tracer development, the second on preclinical research and the third on clinical PET/MRI. The study of Paper III is a part of the clinical PET/MRI project, and ongoing studies also include the use of $[^{18}F]$FACBC PET/MRI in glioma patients, the use of a new second-generation tau tracer, $[^{18}F]$MK-6240, conducted on patients with MCI, as well as a theranostic study on $[^{68}Ga]$PSMA and $[^{177}Lu]$PSMA in recurrent high-grade gliomas.

The ongoing development of both PET image quality and tracers will give new and exciting possibilities and applications of PET/MRI that is not yet found, particularly for the brain.

6 Conclusions

With the offline implementation of an improved research MRAC method evaluated in this thesis, PET/MRI is now considered applicable for clinical brain examinations at St. Olavs Hospital. The largely unexplored potential of PET/MRI in the brain can now be exploited to the benefit of the patients. The main findings were

I.   Slightly decreased image quality was observed for PET/MRI compared to PET/CT. However, for an increased acquisition time the same detectability was obtained.

II.   The accuracy of the best clinically implemented MRAC method was acceptable for clinical neurological brain examinations but was further improved for research MRAC methods. Based on these results [18F]FDG PET/MRI is now used in clinical routine of dementia at St. Olavs Hospital using one of the proposed research methods (DeepUTE).

III. [18F]FACBC PET showed uptake in brain metastases from all included primary cancers and in general high TBR, although detection of small metastases was superior with MRI. The potential of [18F]FACBC PET for differentiation between recurrence of brain metastases from radiation necrosis and improved tumor delineation should be further evaluated.

The work on this thesis has been an interesting journey where the use of the PET/MRI system at St. Olavs Hospital has gone from technical to clinical research projects and further to implementation in clinical routine. The future looks even more exciting with respect to tracer developments and increasing applications for PET/MRI. I look forward to applying the knowledge and experiences I have acquired throughout these years in my employment as a medical physicist at St. Olavs Hospital for improvement of patient management.

7 References

1. Nutt R. The History of Positron Emission Tomography. Molecular Imaging and Biology. 2002;4(1):11-26.

2. Townsend DW, Beyer T. A combined PET/CT scanner: the path to true image fusion. The British journal of radiology. 2002;75(suppl_9):S24-S30.

3. Townsend DW. Positron Emission Tomography/Computed Tomography. Seminars in nuclear medicine. 2008;38(3):152-66.

4. Fendler WP, Czernin J, Herrmann K, Beyer T. Variations in PET/MRI Operations: Results from an International Survey Among 39 Active Sites. Journal of Nuclear Medicine. 2016;57(12):2016-21.

5. Beyer T, Mawlawi O, Quick HH. PET/MR Instrumentation. In: Ratib O, Schwaiger M, Beyer T, editors. Atlas of PET/MR Imaging in Oncology. Berlin, Heidelberg: Springer Berlin Heidelberg; 2013. p. 7-28.

6. Zaidi H, Ojha N, Morich M, Griesmer J, Hu Z, Maniawski P, et al. Design and performance evaluation of a whole-body Ingenuity TF PET-MRI system. Physics in medicine and biology. 2011;56(10):3091-106.

7. Delso G, Furst S, Jakoby B, Ladebeck R, Ganter C, Nekolla SG, et al. Performance measurements of the Siemens mMR integrated whole-body PET/MR scanner. Journal of nuclear medicine : official publication, Society of Nuclear Medicine. 2011;52(12):1914-22.

8. Cherry SR, Dahlbom M, Phelps ME. PET : physics, instrumentation, and scanners. New York Springer2006.

9. van der Veldt AA, Smit EF, Lammertsma AA. Positron Emission Tomography as a Method for Measuring Drug Delivery to Tumors in vivo: The Example of [(11)C]docetaxel. Front Oncol. 2013;3:208.

10. Berg E, Cherry SR. Innovations in Instrumentation for Positron Emission Tomography. Seminars in nuclear medicine. 2018;48(4):311-31.

11. Roncali E, Cherry SR. Application of silicon photomultipliers to positron emission tomography. Ann Biomed Eng. 2011;39(4):1358-77.

12. Carrio I, Ros P. PET/MRI: Methodology and Clinical Applications: Springer New York; 2014.

13. Alessio AM, Butterworth E, Caldwell JH, Bassingthwaighte JB. Quantitative imaging of coronary blood flow. Nano Rev. 2010;1.

14. Saha PGB. Basics of PET Imaging : Physics, Chemistry, and Regulations. Cham: Springer International Publishing : Imprint: Springer; 2016.

15. Bailey DL, Townsend DW, Valk PE, Maisey MN. Positron Emission Tomography : Basic Sciences. London: Springer London : Imprint: Springer; 2005.

16. Zhang J, Knopp MV. Advances in PET : the latest in instrumentation, technology, and clinical practice. Cham, Switzerland: Springer; 2020.

17. Theodorakis L, Loudos G, Prassopoulos V, Kappas C, Tsougos I, Georgoulias P. A review of PET normalization: striving for count rate uniformity. Nuclear medicine communications. 2013;34(11):1033-45.

18. Carney JP, Townsend DW, Rappoport V, Bendriem B. Method for transforming CT images for attenuation correction in PET/CT imaging. Medical physics. 2006;33(4):976-83.

19.   Watson CC, Newport D, Casey M, DeKemp R, Beanlands R, Schmand M. Evaluation of simulation-based scatter correction for 3-D PET cardiac imaging. IEEE Transactions on Nuclear Science. 1997;44(1):90-7.

20.   Watson CC. New, faster, image-based scatter correction for 3D PET. IEEE Transactions on Nuclear Science. 2000;47(4):1587-94.

21.   Watson CC, Casey ME, Michel C, Bendriem B, editors. Advances in scatter correction for 3D PET/CT. IEEE Symposium Conference Record Nuclear Science 2004; 2004 16-22 Oct. 2004.

22.   Surti S. Update on time-of-flight PET imaging. Journal of nuclear medicine : official publication, Society of Nuclear Medicine. 2015;56(1):98-105.

23.   Spanoudaki VC, Levin CS. Photo-Detectors for Time of Flight Positron Emission Tomography (ToF-PET). Sensors. 2010;10(11):10484-505.

24.   Karlberg AM, Saether O, Eikenes L, Goa PE. Quantitative comparison of PET performance-Siemens Biograph mCT and mMR. EJNMMI physics. 2016;3(1):5.

25.   Budinger TF. Time-of-flight positron emission tomography: status relative to conventional PET. Journal of nuclear medicine : official publication, Society of Nuclear Medicine. 1983;24(1):73-8.

26.   National Electrical Manufacturers Association. Performance Measurements of Positron Emission Tomographs (PET) NEMA Standards Publication NU 2-2018. 2018.

27.   Andersen FL, Klausen TL, Loft A, Beyer T, Holm S. Clinical evaluation of PET image reconstruction using a spatial resolution model. European journal of radiology. 2013;82(5):862-9.

28.   Soret M, Bacharach SL, Buvat I. Partial-volume effect in PET tumor imaging. Journal of nuclear medicine : official publication, Society of Nuclear Medicine. 2007;48(6):932-45.

29.   Tong S, Alessio AM, Kinahan PE. Noise and signal properties in PSF-based fully 3D PET image reconstruction: an experimental evaluation. Physics in medicine and biology. 2010;55(5):1453-73.

30.   Munk OL, Tolbod LP, Hansen SB, Bogsrud TV. Point-spread function reconstructed PET images of sub-centimeter lesions are not quantitative. EJNMMI physics. 2017;4(1):5.

31.   Tsutsui Y, Awamoto S, Himuro K, Umezu Y, Baba S, Sasaki M. Edge Artifacts in Point Spread Function-based PET Reconstruction in Relation to Object Size and Reconstruction Parameters. Asia Oceania journal of nuclear medicine & biology. 2017;5(2):134-43.

32.   Nuyts J, Fessler JA. A penalized-likelihood image reconstruction method for emission tomography, compared to postsmoothed maximum-likelihood with matched spatial resolution. IEEE transactions on medical imaging. 2003;22(9):1042-52.

33.   Cherry SR, Sorenson JA, Phelps ME. chapter 15 - Image Quality in Nuclear Medicine. In: Cherry SR, Sorenson JA, Phelps ME, editors. Physics in Nuclear Medicine (Fourth Edition). Philadelphia: W.B. Saunders; 2012. p. 233-51.

34.   Kessler RM, Ellis JR, Jr., Eden M. Analysis of emission tomographic scan data: limitations imposed by resolution and background. Journal of computer assisted tomography. 1984;8(3):514-22.

35.   Wadsak W, Mitterhauser M. Basics and principles of radiopharmaceuticals for PET/CT. European journal of radiology. 2010;73(3):461-9.

36.   Cherry SR, Sorenson JA, Phelps ME. chapter 5 - Radionuclide and Radiopharmaceutical Production. In: Cherry SR, Sorenson JA, Phelps ME, editors. Physics in Nuclear Medicine (Fourth Edition). Philadelphia: W.B. Saunders; 2012. p. 43-61.

37.   Hutchings M. PET imaging in lymphoma. Expert review of hematology. 2009;2(3):261-76.

38.		Guedj E, Varrone A, Boellaard R, Albert NL, Barthel H, van Berckel B, et al. EANM procedure guidelines for brain PET imaging using [(18)F]FDG, version 3. European journal of nuclear medicine and molecular imaging. 2021.

39.		Rowley PA, Samsonov AA, Betthauser TJ, Pirasteh A, Johnson SC, Eisenmenger LB. Amyloid and Tau PET Imaging of Alzheimer Disease and Other Neurodegenerative Conditions. Semin Ultrasound CT MR. 2020;41(6):572-83.

40.		Law I, Albert NL, Arbizu J, Boellaard R, Drzezga A, Galldiks N, et al. Joint EANM/EANO/RANO practice guidelines/SNMMI procedure standards for imaging of gliomas using PET with radiolabelled amino acids and [(18)F]FDG: version 1.0. European journal of nuclear medicine and molecular imaging. 2019;46(3):540-57.

41.		Cecchin D, Garibotto V, Law I, Goffin K. PET Imaging in Neurodegeneration and Neuro-oncology: Variants and Pitfalls. Seminars in nuclear medicine. 2021.

42.		Dunet V, Pomoni A, Hottinger A, Nicod-Lalonde M, Prior JO. Performance of 18F-FET versus 18F-FDG-PET for the diagnosis and grading of brain tumors: systematic review and meta-analysis. Neuro-oncology. 2016;18(3):426-34.

43.		Albert NL, Weller M, Suchorska B, Galldiks N, Soffietti R, Kim MM, et al. Response Assessment in Neuro-Oncology working group and European Association for Neuro-Oncology recommendations for the clinical use of PET imaging in gliomas. Neuro Oncol. 2016;18(9):1199-208.

44.		Juhász C, Dwivedi S, Kamson DO, Michelhaugh SK, Mittal S. Comparison of amino acid positron emission tomographic radiotracers for molecular imaging of primary and metastatic brain tumors. Mol Imaging. 2014;13.

45.		Pöpperl G, Kreth FW, Mehrkens JH, Herms J, Seelos K, Koch W, et al. FET PET for the evaluation of untreated gliomas: correlation of FET uptake and uptake kinetics with tumour grading. European journal of nuclear medicine and molecular imaging. 2007;34(12):1933-42.

46.		Kratochwil C, Combs SE, Leotta K, Afshar-Oromieh A, Rieken S, Debus J, et al. Intra-individual comparison of ^{18}F-FET and ^{18}F-DOPA in PET imaging of recurrent brain tumors. Neuro Oncol. 2014;16(3):434-40.

47.		Calcagni ML, Galli G, Giordano A, Taralli S, Anile C, Niesen A, et al. Dynamic O-(2-[18F]fluoroethyl)-L-tyrosine (F-18 FET) PET for glioma grading: assessment of individual probability of malignancy. Clinical nuclear medicine. 2011;36(10):841-7.

48.		Galldiks N, Stoffels G, Filss C, Rapp M, Blau T, Tscherpel C, et al. The use of dynamic O-(2-18F-fluoroethyl)-l-tyrosine PET in the diagnosis of patients with progressive and recurrent glioma. Neuro Oncol. 2015;17(9):1293-300.

49.		Galldiks N, Dunkl V, Stoffels G, Hutterer M, Rapp M, Sabel M, et al. Diagnosis of pseudoprogression in patients with glioblastoma using O-(2-[18F]fluoroethyl)-L-tyrosine PET. European journal of nuclear medicine and molecular imaging. 2015;42(5):685-95.

50.		Galldiks N, Stoffels G, Filss CP, Piroth MD, Sabel M, Ruge MI, et al. Role of O-(2-(18)F-fluoroethyl)-L-tyrosine PET for differentiation of local recurrent brain metastasis from radiation necrosis. Journal of nuclear medicine : official publication, Society of Nuclear Medicine. 2012;53(9):1367-74.

51.		Romagna A, Unterrainer M, Schmid-Tannwald C, Brendel M, Tonn JC, Nachbichler SB, et al. Suspected recurrence of brain metastases after focused high dose radiotherapy: can [(18)F]FET- PET overcome diagnostic uncertainties? Radiat Oncol. 2016;11(1):139.

52.   Ceccon G, Lohmann P, Stoffels G, Judov N, Filss CP, Rapp M, et al. Dynamic O-(2-18F-fluoroethyl)-L-tyrosine positron emission tomography differentiates brain metastasis recurrence from radiation injury after radiotherapy. Neuro Oncol. 2017;19(2):281-8.

53.   Tsuyuguchi N, Terakawa Y, Uda T, Nakajo K, Kanemura Y. Diagnosis of Brain Tumors Using Amino Acid Transport PET Imaging with (18)F-fluciclovine: A Comparative Study with L-methyl-(11)C-methionine PET Imaging. Asia Ocean J Nucl Med Biol. 2017;5(2):85-94.

54.   Akhurst T, Beattie B, Gogiberidze G, Montiel J, Cai S, Lassman A, et al. [18F] FACBC imaging of recurrent gliomas: a comparison with [11C] methionine and MRI. Journal of Nuclear Medicine. 2006;47(suppl 1):79P-P.

55.   Michaud L, Beattie BJ, Akhurst T, Dunphy M, Zanzonico P, Finn R, et al. 18F-Fluciclovine (18F-FACBC) PET imaging of recurrent brain tumors. European journal of nuclear medicine and molecular imaging. 2020;47(6):1353-67.

56.   Karlberg A, Berntsen EM, Johansen H, Skjulsvik AJ, Reinertsen I, Dai HY, et al. 18F-FACBC PET/MRI in Diagnostic Assessment and Neurosurgery of Gliomas. Clinical nuclear medicine. 2019;44(7):550-9.

57.   Parent EE, Benayoun M, Ibeanu I, Olson JJ, Hadjipanayis CG, Brat DJ, et al. [(18)F]Fluciclovine PET discrimination between high- and low-grade gliomas. EJNMMI research. 2018;8(1):67.

58.   Johannessen K, Berntsen EM, Johansen H, Solheim TS, Karlberg A, Eikenes L. 18F-FACBC PET/MRI in the evaluation of human brain metastases: a case report. European Journal of Hybrid Imaging. 2021;5(1):7.

59.   Parent EE, Patel D, Nye JA, Li Z, Olson JJ, Schuster DM, et al. [(18)F]-Fluciclovine PET discrimination of recurrent intracranial metastatic disease from radiation necrosis. EJNMMI research. 2020;10(1):148.

60.   Brown RK, Bohnen NI, Wong KK, Minoshima S, Frey KA. Brain PET in suspected dementia: patterns of altered FDG metabolism. Radiographics. 2014;34(3):684-701.

61.   Nobili F, Festari C, Altomare D, Agosta F, Orini S, Van Laere K, et al. Automated assessment of FDG-PET for differential diagnosis in patients with neurodegenerative disorders. European journal of nuclear medicine and molecular imaging. 2018;45(9):1557-66.

62.   Singh TD, Josephs KA, Machulda MM, Drubach DA, Apostolova LG, Lowe VJ, et al. Clinical, FDG and amyloid PET imaging in posterior cortical atrophy. Journal of neurology. 2015;262(6):1483-92.

63.   Kinahan PE, Fletcher JW. Positron emission tomography-computed tomography standardized uptake values in clinical practice and assessing response to therapy. Semin Ultrasound CT MR. 2010;31(6):496-505.

64.   Zaidi H. Quantitative analysis in nuclear medicine imaging: Springer; 2006.

65.   Unterrainer M, Vettermann F, Brendel M, Holzgreve A, Lifschitz M, Zähringer M, et al. Towards standardization of (18)F-FET PET imaging: do we need a consistent method of background activity assessment? EJNMMI research. 2017;7(1):48-.

66.   Keyes JW, Jr. SUV: standard uptake or silly useless value? Journal of nuclear medicine : official publication, Society of Nuclear Medicine. 1995;36(10):1836-9.

67.   Jansen NL, Suchorska B, Wenter V, Eigenbrod S, Schmid-Tannwald C, Zwergal A, et al. Dynamic 18F-FET PET in newly diagnosed astrocytic low-grade glioma identifies high-risk patients. Journal of nuclear medicine : official publication, Society of Nuclear Medicine. 2014;55(2):198-203.

68.   Jansen NL, Graute V, Armbruster L, Suchorska B, Lutz J, Eigenbrod S, et al. MRI-suspected low-grade glioma: is there a need to perform dynamic FET PET? European journal of nuclear medicine and molecular imaging. 2012;39(6):1021-9.

69.   Westbrook C, Talbot J. MRI in Practice. Hoboken, NJ: Wiley-Blackwell; 2019.

70.   Broadhouse K. The Physics of MRI and How We Use It to Reveal the Mysteries of the Mind. Frontiers for Young Minds. 2019;7.

71.   Galldiks N, Langen KJ, Albert NL, Chamberlain M, Soffietti R, Kim MM, et al. PET imaging in patients with brain metastasis-report of the RANO/PET group. Neuro Oncol. 2019;21(5):585-95.

72.   McRobbie DW. MRI : from picture to proton. 2nd ed. ed. Cambridge: Cambridge University Press; 2007.

73.   Shao Y, Cherry SR, Farahani K, Meadors K, Siegel S, Silverman RW, et al. Simultaneous PET and MR imaging. Physics in medicine and biology. 1997;42(10):1965-70.

74.   Schlemmer HP, Pichler BJ, Schmand M, Burbar Z, Michel C, Ladebeck R, et al. Simultaneous MR/PET imaging of the human brain: feasibility study. Radiology. 2008;248(3):1028-35.

75.   Boss A, Stegger L, Bisdas S, Kolb A, Schwenzer N, Pfister M, et al. Feasibility of simultaneous PET/MR imaging in the head and upper neck area. Eur Radiol. 2011;21(7):1439-46.

76.   Drzezga A, Souvatzoglou M, Eiber M, Beer AJ, Fürst S, Martinez-Möller A, et al. First clinical experience with integrated whole-body PET/MR: comparison to PET/CT in patients with oncologic diagnoses. Journal of nuclear medicine : official publication, Society of Nuclear Medicine. 2012;53(6):845-55.

77.   Levin CS, Maramraju SH, Khalighi MM, Deller TW, Delso G, Jansen F. Design Features and Mutual Compatibility Studies of the Time-of-Flight PET Capable GE SIGNA PET/MR System. IEEE transactions on medical imaging. 2016;35(8):1907-14.

78.   Cao T, Chen S, Pang L. NEMA NU2-2012 performance measurements of the United-Imaging uPMR790: a HD TOF simultaneous PET/MR system. Soc Nuclear Med; 2018.

79.   Ladefoged CN, Law I, Anazodo U, Lawrence KS, Izquierdo-Garcia D, Catana C, et al. A multi-centre evaluation of eleven clinically feasible brain PET/MRI attenuation correction techniques using a large cohort of patients. NeuroImage. 2016.

80.   Nuyts J, Dupont P, Stroobants S, Benninck R, Mortelmans L, Suetens P. Simultaneous maximum a posteriori reconstruction of attenuation and activity distributions from emission sinograms. IEEE transactions on medical imaging. 1999;18(5):393-403.

81.   Schulz V, Torres-Espallardo I, Renisch S, Hu Z, Ojha N, Bornert P, et al. Automatic, three-segment, MR-based attenuation correction for whole-body PET/MR data. European journal of nuclear medicine and molecular imaging. 2011;38(1):138-52.

82.   Martinez-Moller A, Souvatzoglou M, Delso G, Bundschuh RA, Chefd'hotel C, Ziegler SI, et al. Tissue classification as a potential approach for attenuation correction in whole-body PET/MRI: evaluation with PET/CT data. Journal of nuclear medicine : official publication, Society of Nuclear Medicine. 2009;50(4):520-6.

83.   Burgos N, Cardoso MJ, Thielemans K, Modat M, Pedemonte S, Dickson J, et al. Attenuation correction synthesis for hybrid PET-MR scanners: application to brain studies. IEEE transactions on medical imaging. 2014;33(12):2332-41.

84.   Wollenweber S, Ambwani S, Delso G, Lonn A, Mullick R, Wiesinger F, et al. Evaluation of an atlas-based PET head attenuation correction using PET/CT & MR patient data. IEEE Transactions on Nuclear Science. 2013;60(5):3383-90.

85.   Paulus DH, Quick HH, Geppert C, Fenchel M, Zhan Y, Hermosillo G, et al. Whole-Body PET/MR Imaging: Quantitative Evaluation of a Novel Model-Based MR Attenuation Correction Method Including Bone. Journal of nuclear medicine : official publication, Society of Nuclear Medicine. 2015;56(7):1061-6.

86.   Benoit D, Ladefoged CN, Rezaei A, Keller SH, Andersen FL, Hojgaard L, et al. Optimized MLAA for quantitative non-TOF PET/MR of the brain. Physics in medicine and biology. 2016;61(24):8854-74.

87.   Samarin A, Burger C, Wollenweber SD, Crook DW, Burger IA, Schmid DT, et al. PET/MR imaging of bone lesions--implications for PET quantification from imperfect attenuation correction. European journal of nuclear medicine and molecular imaging. 2012;39(7):1154-60.

88.   Andersen FL, Ladefoged CN, Beyer T, Keller SH, Hansen AE, Hojgaard L, et al. Combined PET/MR imaging in neurology: MR-based attenuation correction implies a strong spatial bias when ignoring bone. Neuroimage. 2014;84:206-16.

89.   Catana C, van der Kouwe A, Benner T, Michel CJ, Hamm M, Fenchel M, et al. Toward implementing an MRI-based PET attenuation-correction method for neurologic studies on the MR-PET brain prototype. Journal of nuclear medicine : official publication, Society of Nuclear Medicine. 2010;51(9):1431-8.

90.   Wiesinger F, Sacolick LI, Menini A, Kaushik SS, Ahn S, Veit-Haibach P, et al. Zero TE MR bone imaging in the head. Magnetic resonance in medicine. 2016;75(1):107-14.

91.   Sekine T, Ter Voert EE, Warnock G, Buck A, Huellner MW, Veit-Haibach P, et al. Clinical evaluation of ZTE attenuation correction for brain FDG-PET/MR imaging-comparison with atlas attenuation correction. Journal of nuclear medicine : official publication, Society of Nuclear Medicine. 2016.

92.   Aasheim LB, Karlberg A, Goa PE, Haberg A, Sorhaug S, Fagerli UM, et al. PET/MR brain imaging: evaluation of clinical UTE-based attenuation correction. Eur J Nucl Med Mol Imaging. 2015;42(9):1439-46.

93.   Dickson JC, O'Meara C, Barnes A. A comparison of CT- and MR-based attenuation correction in neurological PET. European journal of nuclear medicine and molecular imaging. 2014;41(6):1176-89.

94.   Koesters T, Friedman KP, Fenchel M, Zhan Y, Hermosillo G, Babb J, et al. Dixon Sequence with Superimposed Model-Based Bone Compartment Provides Highly Accurate PET/MR Attenuation Correction of the Brain. J Nucl Med. 2016;57(6):918-24.

95.   Sekine T, Buck A, Delso G, Ter Voert EE, Huellner M, Veit-Haibach P, et al. Evaluation of Atlas-Based Attenuation Correction for Integrated PET/MR in Human Brain: Application of a Head Atlas and Comparison to True CT-Based Attenuation Correction. Journal of nuclear medicine : official publication, Society of Nuclear Medicine. 2016;57(2):215-20.

96.   Catana C. Attenuation correction for human PET/MRI studies. Physics in medicine and biology. 2020;65(23):23tr02.

97.   Liu G, Cao T, Hu L, Zheng J, Pang L, Hu P, et al. Validation of MR-Based Attenuation Correction of a Newly Released Whole-Body Simultaneous PET/MR System. Biomed Res Int. 2019;2019:8213215.

98.   Ladefoged CN, Hansen AE, Henriksen OM, Bruun FJ, Eikenes L, Øen SK, et al. AI-driven attenuation correction for brain PET/MRI: Clinical evaluation of a dementia cohort and importance of the training group size. NeuroImage. 2020;222:117221.

99.   Blanc-Durand P, Khalife M, Sgard B, Kaushik S, Soret M, Tiss A, et al. Attenuation correction using 3D deep convolutional neural network for brain 18F-FDG PET/MR: Comparison with Atlas, ZTE and CT based attenuation correction. PLoS One. 2019;14(10):e0223141.

100.   Dong X, Lei Y, Wang T, Higgins K, Liu T, Curran WJ, et al. Deep learning-based attenuation correction in the absence of structural information for whole-body positron emission tomography imaging. Physics in medicine and biology. 2020;65(5):055011.

101.   Shiri I, Arabi H, Geramifar P, Hajianfar G, Ghafarian P, Rahmim A, et al. Deep-JASC: joint attenuation and scatter correction in whole-body 18F-FDG PET using a deep residual network. European journal of nuclear medicine and molecular imaging. 2020;47(11):2533-48.

102.   Armanious K, Hepp T, Küstner T, Dittmann H, Nikolaou K, La Fougère C, et al. Independent attenuation correction of whole body [18F]FDG-PET using a deep learning approach with Generative Adversarial Networks. EJNMMI research. 2020;10(1):53.

103.   Mostafapour S, Gholamiankhah F, Dadgar H, Arabi H, Zaidi H. Feasibility of Deep Learning-Guided Attenuation and Scatter Correction of Whole-Body 68Ga-PSMA PET Studies in the Image Domain. Clinical nuclear medicine. 2021.

104.   Hu Z, Li Y, Zou S, Xue H, Sang Z, Liu X, et al. Obtaining PET/CT images from non-attenuation corrected PET images in a single PET system using Wasserstein generative adversarial networks. Physics in medicine and biology. 2020;65(21):215010.

105.   Currie GM, Leon JL, Nevo E, Kamvosoulis PV. PET/MR Part 4: Clinical Applications of PET/MRI. Journal of nuclear medicine technology. 2021:jnmt.121.263288.

106.   Broski SM, Goenka AH, Kemp BJ, Johnson GB. Clinical PET/MRI: 2018 Update. AJR American journal of roentgenology. 2018;211(2):295-313.

107.   Grueneisen J, Sawicki LM, Schaarschmidt BM, Suntharalingam S, von der Ropp S, Wetter A, et al. Evaluation of a Fast Protocol for Staging Lymphoma Patients with Integrated PET/MRI. PloS one. 2016;11(6):e0157880-e.

108.   Muehe AM, Theruvath AJ, Lai L, Aghighi M, Quon A, Holdsworth SJ, et al. How to Provide Gadolinium-Free PET/MR Cancer Staging of Children and Young Adults in Less than 1 h: the Stanford Approach. Molecular imaging and biology. 2018;20(2):324-35.

109.   Mattsson S, Johansson L, Leide Svegborn S, Liniecki J, Noßke D, Riklund K, et al. Radiation Dose to Patients from Radiopharmaceuticals: a Compendium of Current Information Related to Frequently Used Substances. Ann ICRP. 2015;44(2 Suppl):7-321.

110.   Spick C, Herrmann K, Czernin J. 18F-FDG PET/CT and PET/MRI Perform Equally Well in Cancer: Evidence from Studies on More Than 2,300 Patients. Journal of nuclear medicine : official publication, Society of Nuclear Medicine. 2016;57(3):420-30.

111.   Weber W. Clinical PET/MR. In: Schober O, Kiessling F, Debus J, editors. Molecular Imaging in Oncology. Cham: Springer International Publishing; 2020. p. 747-64.

112.   Rauscher I, Eiber M, Furst S, Souvatzoglou M, Nekolla SG, Ziegler SI, et al. PET/MR imaging in the detection and characterization of pulmonary lesions: technical and diagnostic evaluation in comparison to PET/CT. Journal of nuclear medicine : official publication, Society of Nuclear Medicine. 2014;55(5):724-9.

113.   Souvatzoglou M, Eiber M, Takei T, Fürst S, Maurer T, Gaertner F, et al. Comparison of integrated whole-body [11C]choline PET/MR with PET/CT in patients with prostate cancer. European journal of nuclear medicine and molecular imaging. 2013;40(10):1486-99.

114.   Eiber M, Takei T, Souvatzoglou M, Mayerhoefer ME, Fürst S, Gaertner FC, et al. Performance of Whole-Body Integrated ^{18}F-FDG PET/MR in Comparison to PET/CT for Evaluation of Malignant Bone Lesions. Journal of Nuclear Medicine. 2014;55(2):191-7.

115.   Catalano OA, Nicolai E, Rosen BR, Luongo A, Catalano M, Iannace C, et al. Comparison of CE-FDG-PET/CT with CE-FDG-PET/MR in the evaluation of osseous metastases in breast cancer patients. Br J Cancer. 2015;112(9):1452-60.

116.   Dukart J, Mueller K, Horstmann A, Barthel H, Moller HE, Villringer A, et al. Combined evaluation of FDG-PET and MRI improves detection and differentiation of dementia. PLoS One. 2011;6(3):e18111.

117.   Park J, Pak K, Yun TJ, Lee EK, Ryoo I, Lee JY, et al. Diagnostic Accuracy and Confidence of [18F] FDG PET/MRI in comparison with PET or MRI alone in Head and Neck Cancer. Sci Rep. 2020;10(1):9490.

118.   Yeh CH, Chan SC, Lin CY, Yen TC, Chang JT, Ko SF, et al. Comparison of (18)F-FDG PET/MRI, MRI, and (18)F-FDG PET/CT for the detection of synchronous cancers and distant metastases in patients with oropharyngeal and hypopharyngeal squamous cell carcinoma. European journal of nuclear medicine and molecular imaging. 2020;47(1):94-104.

119.   Crimì F, Borsetto D, Stramare R, Di Carlo R, Emauelli E, Nicolai P, et al. [(18)F]FDG PET/MRI versus contrast-enhanced MRI in detecting regional HNSCC metastases. Annals of nuclear medicine. 2021;35(2):260-9.

120.   Sawicki LM, Kirchner J, Grueneisen J, Ruhlmann V, Aktas B, Schaarschmidt BM, et al. Comparison of (18)F-FDG PET/MRI and MRI alone for whole-body staging and potential impact on therapeutic management of women with suspected recurrent pelvic cancer: a follow-up study. European journal of nuclear medicine and molecular imaging. 2018;45(4):622-9.

121.   Steiner A, Narva S, Rinta-Kiikka I, Hietanen S, Hynninen J, Virtanen J. Diagnostic efficiency of whole-body (18)F-FDG PET/MRI, MRI alone, and SUV and ADC values in staging of primary uterine cervical cancer. Cancer imaging : the official publication of the International Cancer Imaging Society. 2021;21(1):16.

122.   Li M, Huang Z, Yu H, Wang Y, Zhang Y, Song B. Comparison of PET/MRI with multiparametric MRI in diagnosis of primary prostate cancer: A meta-analysis. European journal of radiology. 2019;113:225-31.

123.   Overcast WB, Davis KM, Ho CY, Hutchins GD, Green MA, Graner BD, et al. Advanced imaging techniques for neuro-oncologic tumor diagnosis, with an emphasis on PET-MRI imaging of malignant brain tumors. Current Oncology Reports. 2021;23(3):34.

124.   Hourani R, Brant LJ, Rizk T, Weingart JD, Barker PB, Horská A. Can Proton MR Spectroscopic and Perfusion Imaging Differentiate Between Neoplastic and Nonneoplastic Brain Lesions in Adults? American Journal of Neuroradiology. 2008;29(2):366-72.

125.   Werner JM, Stoffels G, Lichtenstein T, Borggrefe J, Lohmann P, Ceccon G, et al. Differentiation of treatment-related changes from tumour progression: a direct comparison between dynamic FET PET and ADC values obtained from DWI MRI. European journal of nuclear medicine and molecular imaging. 2019;46(9):1889-901.

126.   Kebir S, Rauschenbach L, Galldiks N, Schlaak M, Hattingen E, Landsberg J, et al. Dynamic O-(2-[18F]fluoroethyl)-L-tyrosine PET imaging for the detection of checkpoint inhibitor-related pseudoprogression in melanoma brain metastases. Neuro-oncology. 2016;18(10):1462-4.

127.   Galldiks N, Abdulla DSY, Scheffler M, Wolpert F, Werner JM, Hüllner M, et al. Treatment Monitoring of Immunotherapy and Targeted Therapy Using (18)F-FET PET in Patients with

Melanoma and Lung Cancer Brain Metastases: Initial Experiences. Journal of nuclear medicine : official publication, Society of Nuclear Medicine. 2021;62(4):464-70.

128.   Abdulla DSY, Scheffler M, Brandes V, Ruge M, Kunze S, Merkelbach-Bruse S, et al. Monitoring Treatment Response to Erlotinib in EGFR-mutated Non–small-cell Lung Cancer Brain Metastases Using Serial O-(2-[18F]fluoroethyl)-L-tyrosine PET. Clinical Lung Cancer. 2019;20(2):e148-e51.

129.   Barthel H, Schroeter ML, Hoffmann K-T, Sabri O. PET/MR in Dementia and Other Neurodegenerative Diseases. Seminars in nuclear medicine. 2015;45(3):224-33.

130.   Minoshima S, Drzezga AE, Barthel H, Bohnen N, Djekidel M, Lewis DH, et al. SNMMI Procedure Standard/EANM Practice Guideline for Amyloid PET Imaging of the Brain 1.0. Journal of Nuclear Medicine. 2016;57(8):1316-22.

131.   McKhann GM, Knopman DS, Chertkow H, Hyman BT, Jack CR, Jr., Kawas CH, et al. The diagnosis of dementia due to Alzheimer's disease: recommendations from the National Institute on Aging-Alzheimer's Association workgroups on diagnostic guidelines for Alzheimer's disease. Alzheimers Dement. 2011;7(3):263-9.

132.   Dubois B, Feldman HH, Jacova C, Hampel H, Molinuevo JL, Blennow K, et al. Advancing research diagnostic criteria for Alzheimer's disease: the IWG-2 criteria. The Lancet Neurology. 2014;13(6):614-29.

133.   Landis JR, Koch GG. The measurement of observer agreement for categorical data. Biometrics. 1977;33(1):159-74.

134.   Øen SK, Aasheim LB, Eikenes L, Karlberg AM. Image quality and detectability in Siemens Biograph PET/MRI and PET/CT systems-a phantom study. EJNMMI physics. 2019;6(1):16.

135.   Rausch I, Rischka L, Ladefoged CN, Furtner J, Fenchel M, Hahn A, et al. PET/MRI for Oncologic Brain Imaging: A Comparison of Standard MR-Based Attenuation Corrections with a Model-Based Approach for the Siemens mMR PET/MR System. Journal of nuclear medicine : official publication, Society of Nuclear Medicine. 2017;58(9):1519-25.

136.   De Luca F, Bolin M, Blomqvist L, Wassberg C, Martin H, Falk Delgado A. Validation of PET/MRI attenuation correction methodology in the study of brain tumours. BMC Med Imaging. 2020;20(1):126.

137.   Rausch I, Zitterl A, Berroterán-Infante N, Rischka L, Prayer D, Fenchel M, et al. Dynamic [18F]FET-PET/MRI using standard MRI-based attenuation correction methods. European radiology. 2019;29(8):4276-85.

138.   Sekine T, Buck A, Delso G, Kemp B, Ter Voert E, Huellner M, et al. The impact of atlas-based MR attenuation correction on the diagnosis of FDG-PET/MR for Alzheimer's diseases- A simulation study combining multi-center data and ADNI-data. PLoS One. 2020;15(6):e0233886.

139.   Ando T, Kemp B, Warnock G, Sekine T, Kaushik S, Wiesinger F, et al. Zero Echo Time MRAC on FDG-PET/MR Maintains Diagnostic Accuracy for Alzheimer's Disease; A Simulation Study Combining ADNI-Data. Frontiers in neuroscience. 2020;14:569706.

140.   Sgard B, Khalifé M, Bouchut A, Fernandez B, Soret M, Giron A, et al. ZTE MR-based attenuation correction in brain FDG-PET/MR: performance in patients with cognitive impairment. Eur Radiol. 2020;30(3):1770-9.

141.   Guedj E, Varrone A, Boellaard R, Albert NL, Barthel H, van Berckel B, et al. EANM procedure guidelines for brain PET imaging using [18F]FDG, version 3. European journal of nuclear medicine and molecular imaging. 2022;49(2):632-51.

142.   Aide N, Lasnon C, Desmonts C, Armstrong IS, Walker MD, McGowan DR. Advances in PET-CT technology: An update. Seminars in nuclear medicine. 2021.

143.   Adler S, Seidel J, Choyke P, Knopp MV, Binzel K, Zhang J, et al. Minimum lesion detectability as a measure of PET system performance. EJNMMI physics. 2017;4.

144.   Bogsrud TV, Londalen A, Brandal P, Leske H, Panagopoulos I, Borghammer P, et al. 18F-Fluciclovine PET/CT in Suspected Residual or Recurrent High-Grade Glioma. Clinical nuclear medicine. 2019;44(8):605-11.

145.   Chen S, Gu Y, Yu H, Chen X, Cao T, Hu L, et al. NEMA NU2-2012 performance measurements of the United Imaging uPMR790: an integrated PET/MR system. European journal of nuclear medicine and molecular imaging. 2021;48(6):1726-35.

146.   Greve DN, Salat DH, Bowen SL, Izquierdo-Garcia D, Schultz AP, Catana C, et al. Different partial volume correction methods lead to different conclusions: An 18F-FDG-PET study of aging. NeuroImage. 2016;132:334-43.

147.   Caribé PRRV, Koole M, D'Asseler Y, Deller TW, Van Laere K, Vandenberghe S. NEMA NU 2–2007 performance characteristics of GE Signa integrated PET/MR for different PET isotopes. EJNMMI physics. 2019;6(1):11.

148.   Pourashraf S, Gonzalez-Montoro A, Won JY, Lee MS, Cates JW, Zhao Z, et al. Scalable electronic readout design for a 100 ps coincidence time resolution TOF-PET system. Physics in Medicine & Biology. 2021;66(8):085005.

149.   Nadig V, Herrmann K, Mottaghy F, Schulz V. Hybrid total-body pet scanners—current status and future perspectives. European journal of nuclear medicine and molecular imaging. 2021:1-15.

150.   Ribeiro D, Hallett W, Tavares AAS. Performance evaluation of the Q.Clear reconstruction framework versus conventional reconstruction algorithms for quantitative brain PET-MR studies. EJNMMI physics. 2021;8(1):41.

151.   Caribé PRRV, Koole M, D'Asseler Y, Van Den Broeck B, Vandenberghe S. Noise reduction using a Bayesian penalized-likelihood reconstruction algorithm on a time-of-flight PET-CT scanner. EJNMMI physics. 2019;6(1):22.

152.   Parvizi N, Franklin JM, McGowan DR, Teoh EJ, Bradley KM, Gleeson FV. Does a novel penalized likelihood reconstruction of 18F-FDG PET-CT improve signal-to-background in colorectal liver metastases? European journal of radiology. 2015;84(10):1873-8.

153.   Howard BA, Morgan R, Thorpe MP, Turkington TG, Oldan J, James OG, et al. Comparison of Bayesian penalized likelihood reconstruction versus OS-EM for characterization of small pulmonary nodules in oncologic PET/CT. Annals of nuclear medicine. 2017;31(8):623-8.

154.   Teoh EJ, McGowan DR, Bradley KM, Belcher E, Black E, Gleeson FV. Novel penalised likelihood reconstruction of PET in the assessment of histologically verified small pulmonary nodules. European Radiology. 2016;26(2):576-84.

155.   Teoh EJ, McGowan DR, Bradley KM, Belcher E, Black E, Moore A, et al. 18F-FDG PET/CT assessment of histopathologically confirmed mediastinal lymph nodes in non-small cell lung cancer using a penalised likelihood reconstruction. European Radiology. 2016;26(11):4098-106.

156.   Mehranian A, Wollenweber SD, Walker MD, Bradley KM, Fielding PA, Su K-H, et al. Image enhancement of whole-body oncology [18F]-FDG PET scans using deep neural networks to reduce noise. European journal of nuclear medicine and molecular imaging. 2022;49(2):539-49.

157.   Fact sheet on dementia. World Health Organization (WHO). 2021;https://www.who.int/news-room/fact-sheets/detail/dementia.

158.   Ni R, Nitsch RM. Recent Developments in Positron Emission Tomography Tracers for Proteinopathies Imaging in Dementia. Front Aging Neurosci. 2022;13:751897-.

159. Grosu AL, Astner ST, Riedel E, Nieder C, Wiedenmann N, Heinemann F, et al. An interindividual comparison of O-(2-[18F]fluoroethyl)-L-tyrosine (FET)- and L-[methyl-11C]methionine (MET)-PET in patients with brain gliomas and metastases. Int J Radiat Oncol Biol Phys. 2011;81(4):1049-58.

160. Unterrainer M, Galldiks N, Suchorska B, Kowalew LC, Wenter V, Schmid-Tannwald C, et al. (18)F-FET PET Uptake Characteristics in Patients with Newly Diagnosed and Untreated Brain Metastasis. Journal of nuclear medicine : official publication, Society of Nuclear Medicine. 2017;58(4):584-9.

161. Yomo S, Oguchi K. Prospective study of (11)C-methionine PET for distinguishing between recurrent brain metastases and radiation necrosis: limitations of diagnostic accuracy and long-term results of salvage treatment. BMC cancer. 2017;17(1):713.

162. Terakawa Y, Tsuyuguchi N, Iwai Y, Yamanaka K, Higashiyama S, Takami T, et al. Diagnostic accuracy of 11C-methionine PET for differentiation of recurrent brain tumors from radiation necrosis after radiotherapy. Journal of nuclear medicine : official publication, Society of Nuclear Medicine. 2008;49(5):694-9.

163. Percy DB, Ribot EJ, Chen Y, McFadden C, Simedrea C, Steeg PS, et al. In vivo characterization of changing blood-tumor barrier permeability in a mouse model of breast cancer metastasis: a complementary magnetic resonance imaging approach. Investigative radiology. 2011;46(11):718-25.

164. Henry MN, Chen Y, McFadden CD, Simedrea FC, Foster PJ. In-vivo longitudinal MRI study: an assessment of melanoma brain metastases in a clinically relevant mouse model. Melanoma research. 2015;25(2):127-37.

165. Gempt J, Bette S, Buchmann N, Ryang YM, Forschler A, Pyka T, et al. Volumetric Analysis of F-18-FET-PET Imaging for Brain Metastases. World Neurosurg. 2015;84(6):1790-7.

166. Kondo A, Ishii H, Aoki S, Suzuki M, Nagasawa H, Kubota K, et al. Phase IIa clinical study of [18F]fluciclovine: efficacy and safety of a new PET tracer for brain tumors. Annals of nuclear medicine. 2016;30(9):608-18.

167. Wakabayashi T, Iuchi T, Tsuyuguchi N, Nishikawa R, Arakawa Y, Sasayama T, et al. Diagnostic Performance and Safety of Positron Emission Tomography Using (18)F-Fluciclovine in Patients with Clinically Suspected High- or Low-grade Gliomas: A Multicenter Phase IIb Trial. Asia Ocean J Nucl Med Biol. 2017;5(1):10-21.

168. Albert NL, Winkelmann I, Suchorska B, Wenter V, Schmid-Tannwald C, Mille E, et al. Early static (18)F-FET-PET scans have a higher accuracy for glioma grading than the standard 20-40 min scans. European journal of nuclear medicine and molecular imaging. 2016;43(6):1105-14.

169. Galldiks N, Niyazi M, Grosu AL, Kocher M, Langen KJ, Law I, et al. Contribution of PET imaging to radiotherapy planning and monitoring in glioma patients - a report of the PET/RANO group. Neuro Oncol. 2021;23(6):881-93.

170. Laack NN, Pafundi D, Anderson SK, Kaufmann T, Lowe V, Hunt C, et al. Initial Results of a Phase 2 Trial of (18)F-DOPA PET-Guided Dose-Escalated Radiation Therapy for Glioblastoma. Int J Radiat Oncol Biol Phys. 2021;110(5):1383-95.

171. Piroth MD, Pinkawa M, Holy R, Klotz J, Schaar S, Stoffels G, et al. Integrated boost IMRT with FET-PET-adapted local dose escalation in glioblastomas. Strahlentherapie und Onkologie. 2012;188(4):334-9.

172. Kosztyla R, Raman S, Moiseenko V, Reinsberg SA, Toyota B, Nichol A. Dose-painted volumetric modulated arc therapy of high-grade glioma using 3,4-dihydroxy-6-[(18F]fluoro-L-phenylalanine positron emission tomography. The British journal of radiology. 2019;92(1099):20180901.

173.   Galldiks N, Niyazi M, Grosu AL, Kocher M, Langen KJ, Law I, et al. Contribution of PET imaging to radiotherapy planning and monitoring in glioma patients - a report of the PET/RANO group. Neuro Oncol. 2021.

174.   Brandsma D, Stalpers L, Taal W, Sminia P, van den Bent MJ. Clinical features, mechanisms, and management of pseudoprogression in malignant gliomas. The Lancet Oncology. 2008;9(5):453-61.

175.   Stopa BM, Juhász C, Mittal S. Comparison of Amino Acid PET to Advanced and Emerging MRI Techniques for Neurooncology Imaging: A Systematic Review of the Recent Studies. Mol Imaging. 2021;2021:8874078.

176.   Kunikowska J, Czepczyński R, Pawlak D, Koziara H, Pełka K, Królicki L. Expression of glutamate carboxypeptidase II in the glial tumor recurrence evaluated in vivo using radionuclide imaging. Scientific reports. 2022;12(1):652-.

177.   Datta Gupta S, Arora G, Kumar D, Seith Bhalla A, Sikka K, Shamim SA. Rare Brain Metastasis in Parotid Adenoid Cystic Carcinoma Detected on 68Ga-PSMA PET/CT. Clinical nuclear medicine. 2021;46(11):e561-e2.

178.   Parihar AS, Chandekar KR, Singh H, Sood A, Mittal BR. Orbital and brain metastases on (68)Ga-PSMA PET/CT in a patient with prostate carcinoma refractory to (177)Lu-PSMA and (225)Ac-PSMA therapy. Asia Oceania journal of nuclear medicine & biology. 2021;9(1):67-70.

179.   Pitalua-Cortes Q, García-Perez FO, Vargas-Ahumada J, Gonzalez-Rueda S, Gomez-Argumosa E, Ignacio-Alvarez E, et al. Head-to-Head Comparison of (68)Ga-PSMA-11 and (131)I in the Follow-Up of Well-Differentiated Metastatic Thyroid Cancer: A New Potential Theragnostic Agent. Front Endocrinol (Lausanne). 2021;12:794759.

180.   Arslan E, Ergül N, Karagöz Y, Gedik AA, Çermik TF. Recurrent Brain Metastasis of Triple Negative Breast Cancer With High Uptake in 68Ga-PSMA-11 PET/CT. Clinical nuclear medicine. 2021;46(2):e106-e8.

181.   Hod N, Lantsberg S, Benkovich E, Kazap DE, Preiskel M, Levin D. Incidental Detection of Malignant Melanoma Brain Recurrence on 68Ga–Prostate-Specific Membrane Antigen PET/CT. Clinical nuclear medicine. 2020;45(11):896-9.

182.   Marafi F, Sasikumar A, Alfeeli M, Fathallah W. 18F-PSMA 1007 Uptake in Brain Metastases From Breast Cancer. Clinical nuclear medicine. 2020;45(2):e77-e9.

183.   Sartor O, de Bono J, Chi KN, Fizazi K, Herrmann K, Rahbar K, et al. Lutetium-177-PSMA-617 for Metastatic Castration-Resistant Prostate Cancer. N Engl J Med. 2021;385(12):1091-103.

184.   Morris MJ, De Bono JS, Chi KN, Fizazi K, Herrmann K, Rahbar K, et al. Phase III study of lutetium-177-PSMA-617 in patients with metastatic castration-resistant prostate cancer (VISION). Journal of Clinical Oncology. 2021;39(18_suppl):LBA4-LBA.

185.   Strosberg JR, Caplin ME, Kunz PL, Ruszniewski PB, Bodei L, Hendifar AE, et al. Final overall survival in the phase 3 NETTER-1 study of lutetium-177-DOTATATE in patients with midgut neuroendocrine tumors. Journal of Clinical Oncology. 2021;39(15_suppl):4112-.

186.   Filippi L, Chiaravalloti A, Schillaci O, Cianni R, Bagni O. Theranostic approaches in nuclear medicine: current status and future prospects. Expert Rev Med Devices. 2020;17(4):331-43.

187.   Bertagna F, Albano D, Cerudelli E, Gazzilli M, Giubbini R, Treglia G. Potential of Radiolabeled PSMA PET/CT or PET/MRI Diagnostic Procedures in Gliomas/Glioblastomas. Current radiopharmaceuticals. 2020;13(2):94-8.

188.	Kunikowska J, Charzyńska I, Kuliński R, Pawlak D, Maurin M, Królicki L. Tumor uptake in glioblastoma multiforme after IV injection of [(177)Lu]Lu-PSMA-617. European journal of nuclear medicine and molecular imaging. 2020;47(6):1605-6.

189.	Kumar A, Ballal S, Yadav MP, ArunRaj ST, Haresh KP, Gupta S, et al. 177Lu-/68Ga-PSMA Theranostics in Recurrent Glioblastoma Multiforme: Proof of Concept. Clinical nuclear medicine. 2020;45(12).

190.	Lohmann P, Kocher M, Ceccon G, Bauer EK, Stoffels G, Viswanathan S, et al. Combined FET PET/MRI radiomics differentiates radiation injury from recurrent brain metastasis. NeuroImage Clinical. 2018;20:537-42.

191.	Munoz C, Kunze KP, Neji R, Vitadello T, Rischpler C, Botnar RM, et al. Motion-corrected whole-heart PET-MR for the simultaneous visualisation of coronary artery integrity and myocardial viability: an initial clinical validation. European journal of nuclear medicine and molecular imaging. 2018;45(11):1975-86.

192.	Chen KT, Salcedo S, Chonde DB, Izquierdo-Garcia D, Levine MA, Price JC, et al. MR-assisted PET motion correction in simultaneous PET/MRI studies of dementia subjects. Journal of magnetic resonance imaging : JMRI. 2018;48(5):1288-96.

193.	Keller SH, Hansen C, Hansen C, Andersen FL, Ladefoged C, Svarer C, et al. Motion correction in simultaneous PET/MR brain imaging using sparsely sampled MR navigators: a clinically feasible tool. EJNMMI physics. 2015;2(1):14-.

194.	Johnson PM, Taylor R, Whelan T, Thiessen JD, Anazodo U, Drangova M. Rigid-body motion correction in hybrid PET/MRI using spherical navigator echoes. Physics in medicine and biology. 2019;64(8):08nt3.

195.	Guérin B, Cho S, Chun SY, Zhu X, Alpert NM, El Fakhri G, et al. Nonrigid PET motion compensation in the lower abdomen using simultaneous tagged-MRI and PET imaging. Medical physics. 2011;38(6):3025-38.

196.	Chen KT, Salcedo S, Gong K, Chonde DB, Izquierdo-Garcia D, Drzezga AE, et al. An Efficient Approach to Perform MR-assisted PET Data Optimization in Simultaneous PET/MR Neuroimaging Studies. Journal of nuclear medicine : official publication, Society of Nuclear Medicine. 2018.

197.	Yan J, Lim JC, Townsend DW. MRI-guided brain PET image filtering and partial volume correction. Physics in medicine and biology. 2015;60(3):961-76.

198.	Coello C, Willoch F, Selnes P, Gjerstad L, Fladby T, Skretting A. Correction of partial volume effect in (18)F-FDG PET brain studies using coregistered MR volumes: voxel based analysis of tracer uptake in the white matter. NeuroImage. 2013;72:183-92.

199.	Tang J, Rahmim A. Anatomy assisted PET image reconstruction incorporating multi-resolution joint entropy. Physics in medicine and biology. 2015;60(1):31-48.

200.	Hutchcroft W, Wang G, Chen KT, Catana C, Qi J. Anatomically-aided PET reconstruction using the kernel method. Physics in medicine and biology. 2016;61(18):6668-83.

8 Authors' contributions

Paper I

SKØ was involved in the study design, generated offline AC maps, performed the image reconstructions and data analysis, and drafted the manuscript. TK was responsible for patient recruitment and interpreted PET images. EMB interpreted MR images, and JFA and TS interpreted PET images. CNL generated DeepUTE MRAC maps. AK contributed to the study design, was responsible for the acquisition protocol, and revised the manuscript thoroughly. LE was involved in the study design, applied for ethical approval and gathered written informed consent, was responsible for the acquisition protocol and revised the manuscript thoroughly. All authors read and approved the final manuscript.

Paper II

SKØ participated in the phantom preparations and acquisitions, performed the reconstructions and data analysis, and drafted the manuscript. LBA took part in the study design and assisted the data analysis. LE participated in the study design, visual image evaluations and revised the manuscript thoroughly. AK conceived the study, performed the phantom preparations and acquisitions, participated in the visual image evaluations and revised the manuscript thoroughly. All authors read and approved the final manuscript.

Paper III

SKØ was involved in developing the acquisition protocol, gathered informed consent, performed image reconstructions and image analysis, and drafted the manuscript. KJ participated in image analysis and drafted the manuscript together with SKØ. LKP recruited patients, gathered patient information and image descriptions. EMB and JAT interpreted MRI images, while HJ and TB interpret PET images. TS contributed to the study design and patient recruitment and revised the manuscript thoroughly. AK participated in study design, was responsible for the acquisition protocol and revised the manuscript thoroughly. LE contributed to the study design, was responsible for the acquisition protocol, applied for ethical approval, gathered written informed consent, performed image reconstructions and revised the manuscript thoroughly. All authors read and approved the final manuscript.

Paper I-III

Paper I

ORIGINAL RESEARCH   **Open Access**

Quantitative and clinical impact of MRI-based attenuation correction methods in [18F]FDG evaluation of dementia

Silje Kjærnes Øen[1*] [iD], Thomas Morten Keil[2], Erik Magnus Berntsen[1,2], Joel Fredrik Aanerud[3], Thomas Schwarzlmüller[4,5], Claes Nøhr Ladefoged[6], Anna Maria Karlberg[1,2] and Live Eikenes[1]

Abstract

Background: Positron emission tomography/magnetic resonance imaging (PET/MRI) is a promising diagnostic imaging tool for the diagnosis of dementia, as PET can add complementary information to the routine imaging examination with MRI. The purpose of this study was to evaluate the influence of MRI-based attenuation correction (MRAC) on diagnostic assessment of dementia with [18F]FDG PET. Quantitative differences in both [18F]FDG uptake and z-scores were calculated for three clinically available (DixonNoBone, DixonBone, UTE) and two research MRAC methods (UCL, DeepUTE) compared to CT-based AC (CTAC). Furthermore, diagnoses based on visual evaluations were made by three nuclear medicine physicians and one neuroradiologist (PET_{CT}, $PET_{DeepUTE}$, $PET_{DixonBone}$, PET_{UTE}, PET_{CT} + MRI, $PET_{DixonBone}$ + MRI). In addition, pons and cerebellum were compared as reference regions for normalization.

Results: The mean absolute difference in z-scores were smallest between MRAC and CTAC with cerebellum as reference region: 0.15 ± 0.11 σ (DeepUTE), 0.15 ± 0.12 σ (UCL), 0.23 ± 0.20 σ (DixonBone), 0.32 ± 0.28 σ (DixonNoBone), and 0.54 ± 0.40 σ (UTE). In the visual evaluation, the diagnoses agreed with PET_{CT} in 74% ($PET_{DeepUTE}$), 67% ($PET_{DixonBone}$), and 70% (PET_{UTE}) of the patients, while PET_{CT} + MRI agreed with $PET_{DixonBone}$ + MRI in 89% of the patients.

Conclusion: The MRAC research methods performed close to that of CTAC in the quantitative evaluation of [18F]FDG uptake and z-scores. Among the clinically implemented MRAC methods, $Dixon_{Bone}$ should be preferred for diagnostic assessment of dementia with [18F]FDG PET/MRI. However, as artifacts occur in $Dixon_{Bone}$ attenuation maps, they must be visually inspected to assure proper quantification.

Keywords: PET/MRI, Attenuation correction, z-scores, dementia

Background

Magnetic resonance imaging (MRI) is today the preferred imaging modality in the clinical workup of suspected neurodegenerative disease due to the high spatial resolution and high soft tissue contrast. MRI can identify atrophy in dementia and exclude other diseases like vascular disease, cerebral amyloid angiopathy, brain tumors, and traumatic as well as inflammatory brain changes [1]. Positron emission

tomography (PET) with fluorodeoxyglucose ([18F]FDG) is however increasingly used to support the clinical diagnosis of patients with suspected dementia, as hypometabolism in certain brain regions can help identify specific types of dementia, including Alzheimer's disease (AD) and frontotemporal dementia (FTD) [2]. PET has a higher sensitivity for detecting early metabolic changes, which takes place prior to the morphological changes visible on MRI [1]. Hybrid PET/MRI systems have opened up the opportunity for simultaneous PET/MRI acquisitions, enabling fast and convenient examinations for patients with dementia. The information from PET and MRI is complementary, and detection of dementia with the combination of [18F]FDG

* Correspondence: silje.k.oen@ntnu.no
[1]Department of Circulation and Medical Imaging, Norwegian University of Science and Technology, Postbox 8905, N-7491 Trondheim, Norway
Full list of author information is available at the end of the article

PET and MRI is more accurate than with either of the imaging modalities alone [3].

As a complement to the visual assessment of hypometabolism in PET images performed by nuclear medicine physicians, PET data can be compared to databases of age-matched healthy controls. Z-score maps are then calculated, which represents the number of standard deviations (σ) separating the [18F]FDG uptake of the patient and the average of the healthy controls, where moderate hypometabolism is defined as a z-score between − 2 σ and − 3 σ, and severe hypometabolism for a z-score below − 3 σ [4]. A prerequisite for using such quantitative comparisons clinically is quantitatively accurate PET images, which are heavily dependent on attenuation correction (AC). AC is one of the most important corrections that needs to be performed on PET images, but is still challenging when using a PET/MRI system.

For PET/computed tomography (CT) systems, AC is based on CT images (CTAC), which is scaled by a bilinear function to represent the linear attenuation coefficients (LACs) of the 511 keV photons. For PET/MRI systems, alternative methods had to be developed in order to calculate attenuation maps from MRI data since there is no direct relation between the MRI signal and the electron density of tissue. Several proposed brain MRI-based AC (MRAC) methods have demonstrated a small and acceptable bias from CTAC (regional difference within ± 5%) [5]. Most of these promising methods are however not implemented in clinical systems, except for Dixon with bone model that recently became available on the Siemens PET/MRI system (software VE11P). A few studies have compared clinically implemented and research MRAC methods with CTAC in the evaluation of cognitive impairment. Cabello et al. [6] compared Dixon-based (without bone) AC and ultrashort echo time (UTE) AC with four novel MRAC methods. They concluded that Dixon- and UTE-based AC were inferior to the research MRAC methods, both when measuring [18F]FDG uptake and z-score accuracy to identify regions with reduced metabolism, compared to CTAC. These findings need to be re-evaluated after the recent software upgrade with modifications to the Dixon and UTE sequences.

The most relevant clinical issue is whether MRAC have an impact on clinical neurodegenerative diagnosis. Werner et al. [7] found that the pattern of hypometabolism remained largely unchanged with Dixon and that the clinical impact was negligible compared to CTAC. Franceschi et al. [8] found similar performance for Dixon and the prototype of Dixon with bone model in visually identifying hypometabolism without z-scores, and also concluded that even Dixon is acceptable for routine clinical evaluation of dementia. Still, the

quantitative errors should be further reduced and MRAC methods better imitating CTAC is warranted.

Another factor that potentially can impact the presence of hypometabolism is the choice of reference region. In the comparison to the database of healthy controls, the [18F]FDG uptake is normalized to a reference region, which should be unaffected by the disease. The most commonly used reference regions in dementia evaluations are cerebellum and pons, and incorrect AC in these regions can induce a bias in the [18F]FDG uptake affecting z-scores throughout the brain. The accuracy of the MRAC methods in the reference region is thus important and should be investigated further.

The aim of this study was to assess the quantitative and clinical impact of the implemented MRAC methods in [18F]FDG PET evaluation of dementia (Dixon, Dixon with bone model, UTE) on the Siemens Biograph PET/MRI scanner. Two research MRAC methods (DeepUTE and UCL) presented in the literature were also included for comparison, in addition to CTAC as reference. Secondary aims were to investigate how the choice of reference region influenced the z-scores quantitatively.

Materials and Methods

Patients

Twenty-seven consecutive patients with suspected dementia were referred to brain PET/CT and PET/MRI examinations. Nine patients were excluded from this study due to incorrect anatomical position during the PET/CT examination ($n = 5$), misregistration of bone in Dixon$_{Bone}$ MRAC ($n = 2$) (the artifacts could not be removed manually and a new Dixon acquisition was not acquired), aliasing in MRI scans ($n = 1$), and problems with co-registration of PET images to the MNI PET template ($n = 1$). The 18 patients included had a mean age of 69 ± 9 years and a mean weight of 75 ± 16 kg. Patient characteristics and the proposed diagnosis made by a nuclear medicine physician and a neuroradiologist based on PET/CT and MR imaging and clinical referral text is given in Table 1. The study was approved by the Regional Committee for ethics in Medical Research (REC Central) (ref. number: 2013/1371) and all patients gave written informed consent.

Image acquisition and reconstruction

Image acquisition was performed on a Biograph mCT PET/CT system (software version VG51C), and subsequently on a Biograph mMR PET/MRI system (software version VE11P) (Siemens Healthcare GmbH, Erlangen, Germany). All patients fasted at least 6 h prior to intravenous injection of [18F]FDG (210 ± 46 MBq). The patients were kept blindfolded in a quiet room during the uptake phase prior to the PET/CT examination, which was performed 35 ± 1 min post injection (p.i.),

Table 1 Patient characteristics

Patient	Age (years)	Gender	Proposed diagnosis[a]
1	72	M	Non-specific
2	70	F	FTD
3	49	F	Normal
4	78	F	Normal
5	74	M	FTD
6	64	M	Normal
7	83	F	AD/FTD[b]
8	54	F	Non-specific
9	61	M	Normal
10	82	M	Normal
11	71	F	Non-specific
12	75	F	Normal
13	68	M	Non-specific
14	66	F	Normal
15	72	F	Non-specific
16	63	M	AD
17	69	M	Non-specific[c]
18	70	F	Normal

AD Alzheimer's disease, *FTD* frontotemporal dementia, *Non-specific* other subtypes of dementia, and other patterns of hypometabolism that cannot be explained by image artifacts
[a]Diagnosis based on PET/CT + MRI and clinical referral text
[b]Ambiguous clinical information as well as imaging data, but clearly neurodegenerative
[c]Suspicion of normal pressure hydrocephalus (later confirmed clinically and operated with ventricular shunt)

followed by the PET/MRI examination, performed 64 ± 9 min p.i.

Only the low-dose CT scan and the corresponding attenuation map were used (as reference) from the PET/CT examination. The PET (20 min) and MRI (17 min) acquisitions were performed simultaneously, and the MRI protocol consisted of the same sequences as in the clinical MRI protocol for patients with suspicion of dementia (sagittal 3D T1 MPRAGE, coronal T2, transversal FLAIR, GRE T2* (microhemorrhage), and diffusion weighted imaging) in addition to the MRI sequences for MRAC; a high-resolution two-point Dixon VIBE and a UTE sequence. All PET reconstructions were performed on the mMR system using 3D OSEM reconstruction (three iterations and 21 subsets, 344 × 344 image matrix, 4 mm Gaussian filter) and corrections for scatter, randoms, detector normalization, decay, and attenuation.

Attenuation maps
PET data acquired at the PET/MRI system was reconstructed with the following five MR attenuation maps and a CT attenuation map (presented in Fig. 4) for each patient:

1. Dixon$_{NoBone}$: Implemented at the mMR system. Segmentation-based method that relies on the two-point Dixon VIBE sequence (Brain HiRes), where air, fat, and soft tissue are segmented and assigned predefined discrete LACs (air: 0 cm^{-1}, fat: 0.0854 cm^{-1}, fat/soft tissue mix: 0.0927 cm^{-1}, and soft tissue: 0.1000 cm^{-1}).

2. Dixon$_{Bone}$: Implemented at the mMR system (product in the latest software, VE11P). Similar to Dixon$_{NoBone}$, but includes continuous bone information from an integrated bone atlas by registration of MR images of the subject to MR images of the atlas [9, 10]. The atlas contains sets of pre-aligned MR image and bone mask pairs with bone densities as LACs in cm^{-1} at the PET energy level of 511 keV.

3. UTE: Implemented at the mMR system. Segmentation-based method that relies on the two images from the UTE sequence with different echo times (TE$_1$ and TE$_2$), and segments the image into air (0 cm^{-1}), soft tissue (0.1000 cm^{-1}), and bone (0.1510 cm^{-1}).

4. UCL: Atlas-based method using a database of 41 paired T1-weighted MRI and CT data sets [11–13]. All MRI data sets of the atlas are non-rigidly registered to the patient's MRI data and normalized correlation coefficients are calculated at each voxel. A pseudo CT is then calculated from averaged weights of the CT data sets based on the correlation coefficients. In this study, T1-weighted MPRAGE was used as input in a web-based tool, after bias correction with FMRIB Software Library (FSL, Oxford Centre for Functional MRI of the Brain, UK), as recommended by the distributor. The returned UCL attenuation map in Houndfield units (HU) was converted to LACs [14] and smoothed with a 4 mm Gaussian filter.

5. DeepUTE: Artificial intelligence approach to MRAC, using a deep learning algorithm [15]. Briefly, the method uses a modified 3D U-net architecture [16] for image-to-image learning of paired UTE and CT data. Compared to [15], the network was here trained using data from 832 adult examinations.

6. CT: Attenuation map generated by converting a low-dose CT scan on the mCT scanner to LACs [14]. The bed and head holder was excluded from the CT attenuation map by making a semi-automatic head mask (CT head mask) with the software MRIcron [17], and the attenuation map was multiplied by 10,000 to get the same order of magnitude as the MRAC maps at the mMR system. The CT attenuation maps did not cover the neck region sufficiently for attenuation correction of the PET data from the PET/MRI system due to differences in the

axial field of view of the PET-detectors. The area outside the CT head mask was therefore substituted with the Dixon$_{Bone}$ attenuation map for each patient. The CT image was rigidly registered to the Dixon in-phase image and the same transformation was performed on the CT attenuation map.

The same voxels that were substituted by Dixon$_{Bone}$ in the CT attenuation maps were also substituted by Dixon$_{Bone}$ in all evaluated MR attenuation maps. In order to perform this voxel substitution, the UTE TE$_2$ image and the T1w MPRAGE image was registered to the Dixon in-phase image, and the resulting transformations were used on the respective attenuation maps. All registrations were performed with Aliza Medical Imaging 1.35.3 (Bonn, Germany) (using elastix version 4.8 [18, 19]) [20]. To enable import of the modified attenuation maps at the PET/MRI system, all attenuation maps used the header file of Dixon$_{Bone}$ with exchange of the pixel data.

Quantitative analysis
Bone artifacts
After software upgrade (from VB20P to VE11P) of the PET/MRI system, bone artifacts have been observed in the Dixon$_{Bone}$ and UTE attenuation maps. Two of the most severe artifacts seen in the attenuation maps are misplacement of bone segments from other parts of the body found in the Dixon$_{Bone}$ and bone present inside the brain nearby the anterior ventricles in the UTE attenuation maps. The Dixon$_{Bone}$ and UTE attenuation maps were therefore visually inspected for these artifacts.

[^{18}F]FDG uptake
The [^{18}F]FDG uptake in all PET reconstructions were measured in 15 brain regions that were chosen to match the brain regions in the software used for z-score analysis and visual assessment. The regions were in MNI space and taken from the Harvard-Oxford Cortical Structural Atlas, MNI Structural Atlas, and Talairach Daemon Labels in FSL (Oxford Centre for Functional MRI of the Brain, UK). The PET images of the patients were converted to MNI space by co-registration to a dementia-specific [^{18}F]FDG-PET template [21, 22]. The PET$_{DixonBone}$ was first registered with elastix to the PET template in a two-step process (rigid and non-rigid registration), and the resulting transform was used on the other five PET images of the same patient for transformation to MNI space. Relative difference (RD) was calculated in each brain region, and was defined as

$$\mathrm{RD}(\%) = \frac{\overline{PET}_{MRAC} - \overline{PET}_{CTAC}}{\overline{PET}_{CTAC}} \times 100, \qquad (2)$$

where $\overline{PET}_{MRAC}$ and $\overline{PET}_{CTAC}$ is the average activity measured in a brain region in PET$_{MRAC}$ and PET$_{CTAC}$, respectively. The results are presented by using the boxplot function in MATLAB (R2017b). Absolute RDs were also calculated and averaged over patients and brain regions as $\overline{RD}_{abs}$.

Z-scores
The visual evaluations were performed with the software Cortex ID (GE Healthcare, Waukesha WI, USA), where z-scores were calculated in 26 brain regions. The database constitutes of 294 healthy controls divided in six age groups, imaged with [^{18}F]FDG PET and using a transmission scan of ^{68}Ge for attenuation correction. Both cerebellum and pons were used as reference regions in the quantitative analysis. Quantitative comparison of z-scores between PET$_{MRAC}$ (PET$_{DixonBone}$, PET$_{DixonNoBone}$, PET$_{UTE}$, PET$_{UCL}$, PET$_{DeepUTE}$) and PET$_{CTAC}$ were performed by calculating the difference, D, and absolute difference, D_{abs}, in each brain region, where

$$D = Z_{MRAC} - Z_{CTAC}, and$$

$$D_{abs} = | Z_{MRAC} - Z_{CTAC} |,$$

and D_{abs} was averaged over patients and brain regions as $\overline{D_{abs}}$. The boxplot function in MATLAB was used to present the differences in z-scores.

Visual evaluation
To limit the number of images in the visual evaluation, MRAC methods were chosen based on the z-score analysis. The best and worst of the clinically implemented MRAC methods were included, in addition to the best research MRAC method. The PET$_{CT}$ was used as reference. Three nuclear medicine physicians (brain PET experience; reader 1: 3 years, reader 2: 10 years, reader 3: 1 year) performed the visual assessments individually. Based on PET images and z-scores, the patients were either categorized as normal or diagnosed with AD, FTD, or non-specific pathology (other subtypes of dementia, like DLB, and other patterns of hypometabolism that cannot be explained by image artifacts). The physicians were blinded for AC method and patient ID, and had no information regarding patient history or MRI.

A second reading was made based on both PET images, z-scores, and MR images by a nuclear medicine physician (reader 3) and a neuroradiologist (4-year experience in neuroradiology and European Diploma in NeuroRadiology (EDiNR)) in conjunction. The best clinically implemented MRAC method based on the z-score

analysis was chosen for this second visual evaluation, and PET_{CT} was used as reference. The first and second visual evaluation was done 2 months apart.

PET images and z-scores were evaluated in Cortex ID, while MR images were assessed with the hospitals Picture Archiving and Communication System (PACS; Sectra IDS 7). Cerebellum was chosen as reference region in all visual evaluations.

Statistical analysis

κ-statistics were calculated (with Stata/MP 15.1, Stata-Corp LLC, USA) to determine the agreement between PET_{CT} and each PET_{MRAC} in the visual evaluations after correction for the agreement expected by chance. The inter-reader agreement was also calculated for each AC method in the evaluations with three readers. A κ value of 0 indicates no agreement better than chance, and the values were interpreted according to Landis et al. [23] (poor: < 0, slight: 0.00–0.20, fair: 0.21–0.40, moderate: 0.41–0.60, substantial: 0.61–0.80, almost perfect: 0.81–1.00).

Results

Quantitative analysis

Bone artifacts

Bone artifacts were observed in 22 % (4/18) of the $Dixon_{Bone}$ attenuation maps, while no artifacts were seen in the corresponding Dixon images. New Dixon sequences were acquired for two patients with large bone segments from other parts of the body infiltrating the head (Fig. 1a), resulting in artifact-free attenuation maps (Fig. 1b). Artifacts positioned outside the head (Fig. 1c) were manually removed (Fig. 1d) for the last two patients. Hence, only artifact free $Dixon_{Bone}$ attenuation maps were included in the study. Furthermore, in 89% (16/18) of the UTE attenuation maps, minor bone artifacts were observed inside the brain close to the anterior ventricles (Fig. 1e). The UTE artifacts were not removed.

[18F]FDG uptake

The mean absolute relative difference ($\overline{RD_{abs}}$) in [18F]FDG uptake compared to PET_{CT} was the smallest for $PET_{DeepUTE}$ and the largest when omitting bone information in $PET_{DixonNoBone}$ (Table 2). $PET_{DixonBone}$ performed similar to the research MRAC methods, but had slightly larger range of RD. The relative differences in [18F]FDG uptake for the different brain regions are presented in Fig. 2. Patient 3, with abnormal anatomy (an arachnoid cyst in the posterior fossa), caused most of the outliers seen in Fig. 2. The attenuation maps with corresponding PET images for all reconstructions are demonstrated for this patient in Additional file 1: Figure S1.

Z-scores

The mean absolute difference ($\overline{D_{abs}}$) in z-score between CTAC and MRAC was minimized with the research methods ($PET_{DeepUTE}$ and PET_{UCL}), which also had the smallest range. Among the clinically implemented methods, $PET_{DixonBone}$ performed best, closely followed by $PET_{DixonNoBone}$. The largest $\overline{D_{abs}}$ was found with PET_{UTE} (Table 3). For all MRAC methods, smaller differences were found for cerebellum than for pons as reference region.

Figure 3 shows that the difference in z-scores between CTAC and the MRAC methods were more stable across brain regions for the research methods than for the clinical methods. $PET_{DeepUTE}$ slightly overestimated and PET_{UCL} slightly underestimated the z-scores compared to PET_{CT} for most brain regions for both reference regions (Fig. 3). The clinical MRAC methods ($PET_{DixonBone}$, $PET_{DixonNoBone}$, and PET_{UTE}) yielded lower z-scores than PET_{CT} with pons as reference region, and both over- and underestimated z-scores with cerebellum as reference region (Fig. 3). Examples of z-score maps for one patient with dementia are presented in Fig. 4, where increased hypometabolism is especially pronounced for PET_{UTE} with pons as reference region.
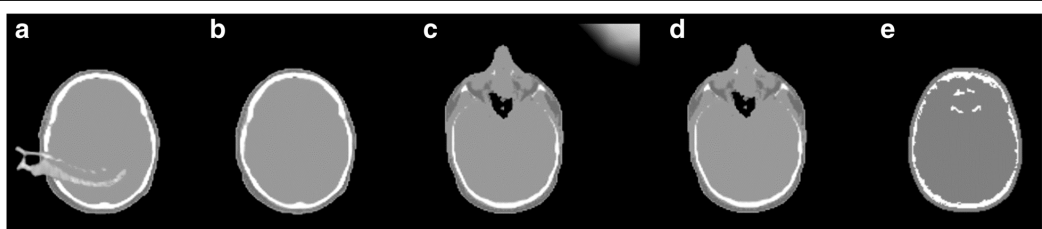
Fig. 1 Typical bone artifacts found in attenuation maps from PET/MRI. **a** $Dixon_{Bone}$ attenuation map with large infiltrative bone segment. Attenuation maps like this were only included in the study if the patient had a second acquisition yielding **b** an artifact-free attenuation map. **c** $Dixon_{Bone}$ attenuation map with artifact in the upper right corner, which could be **d** manually removed. **e** UTE attenuation map with smaller bone segments inside the brain nearby the anterior ventricles. These were not removed

Øen et al. EJNMMI Research   (2019) 9:83

Page 6 of 12

Table 2 The mean absolute relative difference ($\overline{RD_{abs}}$) and the range of RD in ^{18}F[FDG] uptake for the PET$_{MRAC}$ methods compared to PET$_{CTAC}$.

MRAC method	$\overline{RD_{abs}}$ (%) mean ± std	RD (%) [min max]
PET$_{DeepUTE}$	2.2 ± 1.5	[− 10.6, 1.7]
PET$_{UCL}$	3.0 ± 1.4	[− 3.3, 7.3]
PET$_{DixonBone}$	2.5 ± 2.4	[− 13.0, 10.7]
PET$_{DixonNoBone}$	7.1 ± 3.7	[− 19.9, 7.4]
PET$_{UTE}$	4.1 ± 3.3	[− 12.7, 16.3]

Visual evaluation

PET$_{DixonBone}$ and PET$_{UTE}$ were chosen for the first visual evaluations (PET only) as these had the best and the worst results of the clinically implemented MRAC methods in the z-score analysis. The research MRAC methods performed relatively equal in the z-score analysis and PET$_{DeepUTE}$ was chosen for the visual evaluation. Furthermore, PET$_{CT}$ was included as reference. The results of the visual evaluations with PET only are presented in Table 4. The agreement in diagnosis between PET$_{CT}$ and PET$_{DeepUTE}$, PET$_{DixonBone}$ and PET$_{UTE}$ was in average for the three readers 74%, 67%, and 70%, respectively (Table 5), and the κ-statistics indicated mostly *moderate* agreement between PET$_{CT}$ and PET$_{MRAC}$. The inter-reader agreement was *fair* for PET$_{CT}$ (κ = 0.30) and *slight* for PET$_{DeepUTE}$ (κ = 0.17), PET$_{DixonBone}$ (κ = 0.19), and PET$_{UTE}$ (κ = 0.10).

In the second visual evaluation, which also included MRI, PET$_{DixonBone}$ was compared to PET$_{CT}$. When MRI was included in the assessment, the agreement increased to 89% and the κ-statistics indicated *almost perfect* agreement (κ = 0.82) (Table 6) according to Landis et al. [23].

Discussion

The impact of MRAC on dementia assessment was evaluated in this study by comparing [^{18}F]FDG uptake, z-scores, and clinical interpretation between PET$_{MRAC}$ and PET$_{CT}$. The absolute mean quantitative differences in z-scores were small relative to the definition of hypometabolism for most MRAC methods with cerebellum as reference region, and especially for the research methods. Interpretation with PET alone yielded high uncertainties, while assessment with both PET and MRI resulted in almost perfect agreement between PET$_{CT}$ and PET$_{DixonBone}$.

The bone artifacts found in the clinically available MRAC methods highlights the need for careful inspection of the attenuation maps in all brain examinations. In the Dixon$_{Bone}$ attenuation maps, the artifacts were caused by misregistration between the Dixon images and the bone-template, misplacing large bone segments from other parts of the body in the brain. Due to the severity of these artifacts, they were removed by either acquiring a new Dixon acquisition free of this artifact, or manually when found outside the brain. Although not evaluated quantitatively, this artifact would likely induce large errors in the attenuation corrected PET images. The minor bone artifacts observed in most UTE attenuation maps
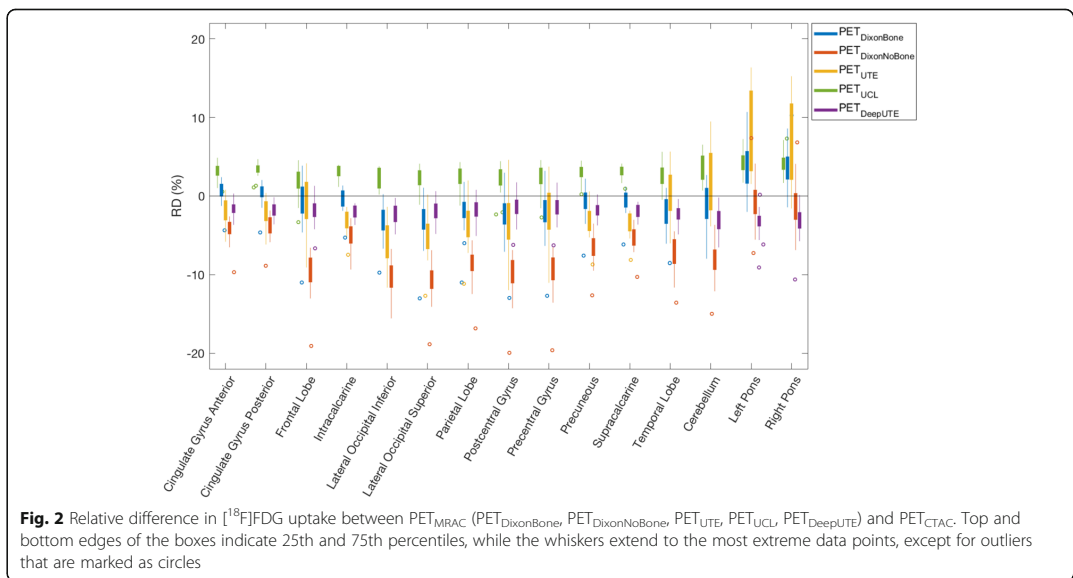
Fig. 2 Relative difference in [^{18}F]FDG uptake between PET$_{MRAC}$ (PET$_{DixonBone}$, PET$_{DixonNoBone}$, PET$_{UTE}$, PET$_{UCL}$, PET$_{DeepUTE}$) and PET$_{CTAC}$. Top and bottom edges of the boxes indicate 25th and 75th percentiles, while the whiskers extend to the most extreme data points, except for outliers that are marked as circles

Table 3 The mean absolute difference $(\overline{D_{abs}})$ in z-score between PET_{MRAC} and PET_{CT} and the range of the difference (D), with pons and cerebellum as reference regions

MRAC method	$\overline{D_{abs}}$ (σ) (pons) mean ± std	D (σ) (pons) [min max]	$\overline{D_{abs}}$ (σ) (cerebellum) mean ± std	D (σ) (cerebellum) [min max]
$PET_{DeepUTE}$	0.19 ± 0.16	[− 0.43, 0.76]	0.15 ± 0.11	[− 0.60, 0.60]
PET_{UCL}	0.21 ± 0.15	[− 0.69, 0.47]	0.15 ± 0.12	[− 0.64, 0.44]
$PET_{DixonBone}$	0.48 ± 0.27	[− 1.52, 0.31]	0.23 ± 0.20	[− 1.14, 1.42]
$PET_{DixonNoBone}$	0.53 ± 0.35	[− 1.77, 0.74]	0.32 ± 0.28	[− 1.32, 1.67]
PET_{UTE}	1.13 ± 0.47	[− 2.85, − 0.02]	0.54 ± 0.40	[− 1.64, 2.49]

Fig. 3 Difference in z-score between PET_{MRAC} ($PET_{DixonBone}$, $PET_{DixonNoBone}$, PET_{UTE}, PET_{UCL}, $PET_{DeepUTE}$) and PET_{CTAC}, for different brain regions, with **a** cerebellum and **b** pons as reference region. Top and bottom edges of the boxes indicate 25th and 75th percentiles, while the whiskers extend to the most extreme data points, except for outliers that are marked as circles

Fig. 4 Examples of z-score maps for one patient (number 16) for the included AC methods, with pons and cerebellum as reference regions, and the corresponding attenuation maps

were caused by changes in the UTE sequence and/or attenuation map algorithm after the software upgrade, and persisted even after acquiring new UTE images. Since the UTE attenuation maps are used clinically, they were not excluded from the current study. In clinical routine, a reliable and stable MRAC method is crucial and these problems need to be solved. The attenuation map errors have been reported to Siemens Healthcare, and will hopefully be solved in the near future. In the meantime, some of the artifacts can be avoided by implementing better procedures among radiographers to detect the artifacts and acquire new MR-based attenuation maps in such cases before the patient leaves the scanner table.

The research MRAC methods, as well as $PET_{DixonBone}$, all demonstrated small absolute differences compared to PET_{CT} regarding $[^{18}F]FDG$ uptake, although the research methods had smaller RD range. Some outliers were observed in the analysis, and most of them were caused by a patient with an abnormal anatomy (arachnoid cyst in posterior fossa). DeepUTE gave least outliers for this patient with abnormal anatomy (2/15 brain regions), while $Dixon_{Bone}$ and $Dixon_{NoBone}$ yielded most outliers for this patient (10/15 brain regions). For

absolute differences in $[^{18}F]FDG$ uptake, the trend was the same as in previous studies [5–7, 24], with descending performance for PET_{UCL}, $PET_{DixonBone}$, PET_{UTE}, and $PET_{DixonNobone}$ (DeepUTE has not been included in previous studies). PET_{UTE} yielded particularly large variations in the pons, probably due to misclassification of bone in that region, which makes pons not suited as a reference region with UTE AC. Furthermore, we found that the LACs for soft tissue were slightly higher with UCL AC and slightly lower with DeepUTE AC compared to the CTAC, which probably caused the general over- and underestimation of $[^{18}F]FDG$ uptake for the two methods, respectively.

For the z-score evaluation, the research MRAC methods yielded the best performance and the differences in z-scores between PET_{MRAC} and PET_{CT} were generally small compared to the definition of hypometabolism, except for PET_{UTE}, when using cerebellum as reference region. Of note, $PET_{DixonBone}$ and $PET_{DixonNoBone}$ yielded similar results for the z-scores, indicating that the missing bone information did not have a remarkable impact on z-scores. Despite small average differences in z-scores to PET_{CT} for most MRAC

Table 4 Assigned diagnostic categorization for each patient made by three nuclear medicine physicians from PET images with three MRAC methods (PET$_{DeepUTE}$, PET$_{DixonBone}$, PET$_{UTE}$) and PET$_{CT}$. Cerebellum was used as reference region. Intra-reader discrepancies with PET$_{CT}$ as reference are italicized

Patient	Reader	PET$_{CT}$	PET$_{DeepUTE}$	PET$_{DixonBone}$	PET$_{UTE}$
1	1	N	N	N	N
	2	N	N	N	*NS*
	3	N	N	N	*NS*
2	1	AD	*N*	AD	AD
	2	NS	*FTD*	*FTD*	NS
	3	FTD	*NS*	*NS*	*NS*
3	1	N	N	N	N
	2	N	N	*NS*	*NS*
	3	N	N	N	*NS*
4	1	N	N	*AD*	*AD*
	2	FTD	FTD	FTD	FTD
	3	N	N	N	N
5	1	FTD	FTD	FTD	FTD
	2	AD	*NS*	*NS*	AD
	3	NS	*AD*	*AD*	*AD*
6	1	N	N	N	*AD*
	2	N	N	N	N
	3	N	N	N	N
7	1	AD	*NS*	*NS*	*NS*
	2	AD	AD	*NS*	AD
	3	AD	AD	AD	AD
8	1	AD	*N*	*N*	AD
	2	FTD	FTD	FTD	FTD
	3	N	*NS*	*NS*	*NS*
9	1	N	N	N	*NS*
	2	NS	NS	*N*	NS
	3	NS	*N*	*N*	*N*
10	1	AD	*N*	*N*	AD
	2	N	N	N	N
	3	N	N	N	N
11	1	N	N	N	*AD*
	2	NS	*FTD*	NS	NS
	3	NS	NS	NS	NS
12	1	N	N	N	N
	2	N	N	N	N
	3	N	N	N	N
13	1	N	N	*FTD*	N
	2	NS	NS	NS	NS
	3	NS	NS	NS	NS
14	1	N	N	N	N
	2	N	*FTD*	*FTD*	*FTD*

Table 4 Assigned diagnostic categorization for each patient made by three nuclear medicine physicians from PET images with three MRAC methods (PET$_{DeepUTE}$, PET$_{DixonBone}$, PET$_{UTE}$) and PET$_{CT}$. Cerebellum was used as reference region. Intra-reader discrepancies with PET$_{CT}$ as reference are italicized *(Continued)*

Patient	Reader	PET$_{CT}$	PET$_{DeepUTE}$	PET$_{DixonBone}$	PET$_{UTE}$
	3	N	N	*NS*	N
15	1	N	N	N	*AD*
	2	FTD	FTD	FTD	FTD
	3	N	*NS*	*NS*	*NS*
16	1	AD	AD	AD	AD
	2	AD	AD	AD	AD
	3	AD	AD	AD	AD
17	1	AD	AD	*NS*	AD
	2	AD	*NS*	AD	AD
	3	NS	NS	NS	NS
18	1	N	N	N	N
	2	NS	NS	NS	NS
	3	N	N	N	N

N normal, *NS* non-specific, *AD* Alzheimer's disease, *FTD* frontotemporal dementia

methods with cerebellum as reference region, large outliers were present for the clinical MRAC methods with a deviation from PET$_{CT}$ > 1 σ, which can have a considerable impact on a z-score assessment. Hence, it is highly desirable to implement the research methods at the clinical PET/MRI systems as soon as possible to avoid large biases in the z-score assessment.

Since the calculation of z-scores use a reference region for normalization, the accuracy of AC in the reference region is of particular importance as bias in this region will affect the hypometabolism globally. Available reference regions in the software used for visual evaluation in the current study were pons, cerebellum, and global cerebral cortex. The extent of hypometabolism can however be underestimated with global normalization [25]. Therefore, only cerebellum and pons were used in this study, and differences in z-scores between MRAC and CTAC were found to be smaller with cerebellum than pons as reference region for all MRAC methods. Although glucose metabolism in the pons have been found to be least affected by dementia among several reference regions [26], the small size makes this region prone to bias and the surrounding inhomogeneous bone affects both attenuation and scatter [25]. Cerebellum is larger and less prone to bias, and the cerebellar glucose metabolism is not significantly reduced for AD patients, except for severe AD [25, 27].

Based on our results, Dixon$_{Bone}$ with cerebellum as reference should be preferred among the clinically implemented MRAC methods when assessing z-scores.

Table 5 κ-statistics for the agreement between PET_{CT} and PET_{MRAC} ($PET_{DeepUTE}$, $PET_{DixonBone}$, PET_{UTE}) for each reader. A κ value of 0 indicates no agreement better than chance, while 1.0 means perfect agreement

	PET_{CT} vs $PET_{DeepUTE}$ Agreement (κ)	PET_{CT} vs $PET_{DixonBone}$ Agreement (κ)	PET_{CT} vs PET_{UTE} Agreement (κ)
Reader 1	77.8% (0.54)	66.7% (0.41)	66.7% (0.47)
Reader 2	72.2% (0.63)	66.7% (0.55)	83.3% (0.78)
Reader 3	72.2% (0.55)	66.7% (0.47)	61.1% (0.39)
Mean of readers	74.1%	66.7%	70.4%

However, for patients with abnormal anatomy and/or unusual tissue density, atlas-based methods should be used with caution [28]. In these cases, or when bone artifacts are present, $Dixon_{NoBone}$ could probably be used as an alternative for z-score assessment in the evaluation of dementia.

The visual evaluations with PET only yielded moderate agreement between PET_{CT} and PET_{MRAC} in general. Highest agreement was found for $PET_{DeepUTE}$, but the other MRAC methods performed quite similarly. Least false positive errors were found for $PET_{DeepUTE}$ compared to PET_{CT}, while false negative errors were highest for $PET_{DeepUTE}$ and $PET_{DixonBone}$. These results seem to

Table 6 Assigned diagnostic categorization made by one nuclear medicine physician (reader 3) and one neuroradiologist in conjunction for PET (PET_{CT}, $PET_{DixonBone}$) and MRI. Discrepancies from PET_{CT} + MRI are italicized

Patient	PET_{CT} + MRI	$PET_{DixonBone}$ + MRI
1	NS	NS
2	NS	NS
3	N	N
4	N	N
5	FTD	FTD
6	N	N
7	FTD	AD[a]
8	N	N
9	N	N
10	N	N
11	Ns	NS
12	N	N
13	NS	NS
14	N	N
15	NS	NS
16	AD	NS
17	NS [b]	NS[b]
18	N	N

AD Alzheimer's disease, FTD frontotemporal dementia
[a]Defined as both FTD and AD in the proposed diagnosis based on PET/CT and MR imaging and clinical referral text (Table 1)
[b]Suspicion of normal pressure hydrocephalus

be in agreement with the quantitative results, as PET_{UTE} underestimated z-scores, inducing false positive errors, while $PET_{DeepUTE}$ slightly overestimated z-scores and tends to more often change pathology to normal than the opposite. However, the inter-reader agreement was low, which indicates that the visual assessment of [^{18}F]FDG PET in dementia is difficult and subjective, and that these evaluations were influenced by additional factors than the different AC methods. Another study by Werner et al. [7], evaluating the clinical impact of different AC methods, demonstrated a higher agreement between the readers; however, the categorization of diagnosis was not the same as in our study, which could have caused less discrepancy in their results.

Due to the large discrepancies in the PET only evaluations, another assessment including MRI was performed. Adding MRI information yielded almost perfect agreement between MRAC and CTAC readings according to the κ-statistics, and in the two cases of discrepancies between PET_{CT} + MRI and $PET_{DixonBone}$ + MRI, the discrepancies were due to different subtypes of dementia. The improvement by including MRI was probably due to the ability to discard areas of hypometabolism due to other pathologies and normal variants (e.g., age-related atrophy, enlarged ventricles, and mega cisterna magna). Furthermore, information of neurodegenerative processes such as hippocampal atrophy (as seen in AD), focal cortical atrophy (as seen in FTD), and white matter hyperintensities (as seen in microvascular disease) was important complementary information to the PET findings. In a clinical setting with all clinical information and imaging available, the discrepancies between MRAC and CTAC would probably be further decreased, but this should be verified in studies with larger patient cohorts.

A limitation of this study is the small number of patients, and hence few patients having dementia and low diversity in diagnoses and severity. Furthermore, PET images suffer from partial volume effects due to the limited resolution that cause spill-out from one region to another. This was not corrected for and could cause a significant effect on hypometabolism from normal aging [29]. However, the aim of this study was to compare MRAC and CTAC, and not the exact diagnosis. Another factor that may affect the z-scores is that the PET

images in the database of Cortex ID were acquired and reconstructed differently than the PET images in this study. Still, the relative differences between CTAC and MRAC should be unaffected.

Conclusion

The quantitative differences in z-scores between CTAC and most MRAC methods were small relative to the definition of hypometabolism, with cerebellum as reference region. Although the research MRAC methods performed slightly better than the clinically implemented MRAC methods regarding calculations of the z-scores, the visual evaluations with PET and MRI demonstrated almost perfect agreement between $Dixon_{Bone}$ and CTAC. Our results indicate that $Dixon_{Bone}$ with cerebellum as reference region should be preferred among the clinically implemented MRAC methods when using Siemens PET/MRI system for dementia assessment with [^{18}F]FDG PET/MRI. Although, inspection of the attenuation maps is a prerequisite for the use of PET/MRI in dementia evaluation.

Additional file

Additional file 1: Figure S1. Attenuation maps (top row) with corresponding PET images (bottom row) for patient number 3 with abnormal anatomy. (a) CT, (b) UCL, (c) DeepUTE, (d) $Dixon_{Bone}$, (e) $Dixon_{NoBone}$ and (f) UTE. (PNG 1967 kb)

Abbreviations

AC: Attenuation correction; AD: Alzheimer's disease; CT: Computed tomography; CTAC: CT-based AC; [^{18}F]FDG: Fluorodeoxyglucose; FTD: Frontotemporal dementia; HU: Houndfield units; LACs: Linear attenuation coefficients; MRI: Magnetic resonance imaging; MRAC: MRI-based AC; PET: Positron emission tomography; RD: Relative difference; UTE: Ultrashort echo time

Authors' contributions

SKØ participated in the study design, generated attenuation maps, performed the image reconstructions, and data analysis. TK was responsible for patient recruitment and interpreted the PET images. EMB interpreted the MR images, while JFA and TS interpreted PET images. CNL generated the DeepUTE attenuation maps. AK participated in the study design, was responsible for the acquisition protocol, gave valuable technical support, and revised the manuscript critically. LE participated in the study design, applied for ethical approval and gathered informed consent, was responsible for the acquisition protocol, gave valuable support throughout the project, and revised the manuscript critically. All authors have read and approved the attached paper.

Availability of data and materials

The datasets used and analyzed during the current study are available from the corresponding author on reasonable request.

Ethics approval and consent to participate

The study was approved by the Regional Committees for Medical and Health Research Ethics (REC) (ref. number: 2013/1371) and all patients gave written informed consent.

Consent for publication

Not applicable.

Competing interests

The authors declare that they have no competing interests.

Author details

[1]Department of Circulation and Medical Imaging, Norwegian University of Science and Technology, Postbox 8905, N-7491 Trondheim, Norway. [2]Department of Radiology and Nuclear Medicine, St. Olavs Hospital, Trondheim, Norway. [3]Department of Nuclear Medicine and PET Centre, Aarhus University Hospital, Aarhus, Denmark. [4]Department of Radiology, Haukeland University Hospital, Bergen, Norway. [5]Department of Clinical Medicine, University of Bergen, Bergen, Norway. [6]Department of Clinical Physiology, Nuclear Medicine & PET, Rigshospitalet, University of Copenhagen, Copenhagen, Denmark.

References

1. Barthel H, Schroeter ML, Hoffmann KT, Sabri O. PET/MR in dementia and other neurodegenerative diseases. Semin Nucl Med. 2015;45(3):224–33.
2. Brown RK, Bohnen NI, Wong KK, Minoshima S, Frey KA. Brain PET in suspected dementia: patterns of altered FDG metabolism. Radiographics. 2014;34(3):684–701.
3. Dukart J, Mueller K, Horstmann A, Barthel H, Moller HE, Villringer A, et al. Combined evaluation of FDG-PET and MRI improves detection and differentiation of dementia. PLoS One. 2011;6(3):e18111.
4. Singh TD, Josephs KA, Machulda MM, Drubach DA, Apostolova LG, Lowe VJ, et al. Clinical, FDG and amyloid PET imaging in posterior cortical atrophy. Journal of neurology. 2015;262(6):1483–92.
5. Ladefoged CN, Law I, Anazodo U, Lawrence KS, Izquierdo-Garcia D, Catana C, et al. A multi-centre evaluation of eleven clinically feasible brain PET/MRI attenuation correction techniques using a large cohort of patients. NeuroImage. 2016.
6. Cabello J, Lukas M, Rota Kops E, Ribeiro A, Shah NJ, Yakushev I, et al. Comparison between MRI-based attenuation correction methods for brain PET in dementia patients. Eur J ucl Med Mol Imaging. 2016; 43(12):2190–200.
7. Werner P, Rullmann M, Bresch A, Tiepolt S, Jochimsen T, Lobsien D, et al. Impact of attenuation correction on clinical [(18)F]FDG brain PET in combined PET/MRI. EJNMMI Res. 2016;6(1):47.
8. Franceschi AM, Abballe V, Raad RA, Nelson A, Jackson K, Babb J, et al. Visual detection of regional brain hypometabolism in cognitively impaired patients is independent of positron emission tomography-magnetic resonance attenuation correction method. World J Nucl Med. 2018;17(3):188–94.
9. Paulus DH, Quick HH, Geppert C, Fenchel M, Zhan Y, Hermosillo G, et al. Whole-body PET/MR imaging: quantitative evaluation of a novel model-based MR attenuation correction method including bone. Journal of nuclear medicine : official publication. Soc Nucl Med. 2015;56(7):1061–6.
10. Koesters T, Friedman KP, Fenchel M, Zhan Y, Hermosillo G, Babb J, et al. Dixon sequence with Superimposed model-based bone compartment provides highly accurate PET/MR attenuation correction of the brain. J Nucl Med. 2016;57(6):918–24.
11. Burgos N, Cardoso MJ, Thielemans K, Modat M, Pedemonte S, Dickson J, et al. Attenuation correction synthesis for hybrid PET-MR scanners: application to brain studies. IEEE Trans Med Imaging. 2014;33(12):2332–41.
12. NiftyWeb [Available from: http://cmictig.cs.ucl.ac.uk/niftyweb/.
13. Prados Carrasco F, Cardoso MJ, Burgos N, Wheeler-Kingshott C, Ourselin S, editors. NiftyWeb: web based platform for image processing on the cloud2016: International Society for Magnetic Resonance in Medicine (ISMRM).

14. Carney JP, Townsend DW, Rappoport V, Bendriem B. Method for transforming CT images for attenuation correction in PET/CT imaging. Med Phys. 2006;33(4):976–83.

15. Ladefoged CN, Marner L, Hindsholm A, Law I, Hojgaard L, Andersen FL. Deep learning based attenuation correction of PET/MRI in pediatric brain tumor patients: evaluation in a clinical setting. Front Neuroscience. 2018;12:1005.

16. Ronneberger O, Fischer P, Brox T, editors. U-Net: convolutional networks for biomedical image segmentation2015; Cham: Springer International Publishing.

17. Rorden C, Karnath HO, Bonilha L. Improving lesion-symptom mapping. J Cogn Neurosci. 2007;19(7):1081–8.

18. Klein S, Staring M, Murphy K, Viergever MA, Pluim JP. elastix: a toolbox for intensity-based medical image registration. IEEE Trans Med Imaging. 2010; 29(1):196–205.

19. Shamonin DP, Bron EE, Lelieveldt BP, Smits M, Klein S, Staring M. Fast parallel image registration on CPU and GPU for diagnostic classification of Alzheimer's disease. Front Neuroinform. 2013;7:50.

20. Aliza Medical Imaging & DICOM Viewer [Available from: alizaviewer@web.de.

21. Della Rosa PA, Cerami C, Gallivanone F, Prestia A, Caroli A, Castiglioni I, et al. A standardized [18F]-FDG-PET template for spatial normalization in statistical parametric mapping of dementia. Neuroinformatics. 2014;12(4):575–93.

22. Perani D, Della Rosa PA, Cerami C, Gallivanone F, Fallanca F, Vanoli EG, et al. Validation of an optimized SPM procedure for FDG-PET in dementia diagnosis in a clinical setting. Neuroimage Clin. 2014;6:445–54.

23. Landis JR, Koch GG. The measurement of observer agreement for categorical data. Biometrics. 1977;33(1):159–74.

24. Hitz S, Habekost C, Furst S, Delso G, Forster S, Ziegler S, et al. Systematic comparison of the performance of integrated whole-body PET/MR imaging to conventional PET/CT for (1)(8)F-FDG brain imaging in patients examined for suspected dementia. Soc Nucl Med. 2014;55(6):923–31.

25. Yakushev I, Landvogt C, Buchholz HG, Fellgiebel A, Hammers A, Scheurich A, et al. Choice of reference area in studies of Alzheimer's disease using positron emission tomography with fluorodeoxyglucose-F18. Psychiatry Res. 2008;164(2):143–53.

26. Minoshima S, Frey KA, Foster NL, Kuhl DE. Preserved pontine glucose metabolism in Alzheimer disease: a reference region for functional brain image (PET) analysis. J Comput Assist Tomogr. 1995;19(4):541–7.

27. Ishii K, Sasaki M, Kitagaki H, Yamaji S, Sakamoto S, Matsuda K, et al. Reduction of cerebellar glucose metabolism in advanced Alzheimer's disease. J Nucl Med. 1997;38(6):925–8.

28. Chen Y, An H. Attenuation correction of PET/MR imaging. Magn Reson Imaging Clin N Am. 2017;25(2):245–55.

29. Greve DN, Salat DH, Bowen SL, Izquierdo-Garcia D, Schultz AP, Catana C, et al. Different partial volume correction methods lead to different conclusions: An 18F-FDG-PET study of aging. NeuroImage. 2016;132:334–43.

Publisher's Note

Springer Nature remains neutral with regard to jurisdictional claims in published maps and institutional affiliations.

Paper II

EJNMMI Physics

ORIGINAL RESEARCH

Open Access

Image quality and detectability in Siemens Biograph PET/MRI and PET/CT systems—a phantom study

Silje Kjærnes Øen[1*], Lars Birger Aasheim[2], Live Eikenes[1] and Anna Maria Karlberg[1,2]

* Correspondence: silje.k.oen@ntnu.
no
[1]Department of Circulation and
Medical Imaging, Norwegian
University of Science and
Technology, Postbox 8905, N-7491
Trondheim, Norway
Full list of author information is
available at the end of the article

Abstract

Background: The technology of modern positron emission tomography (PET) systems continuously improving, and with it the possibility to detect smaller lesions. Since first introduced in 2010, the number of hybrid PET/magnetic resonance imaging (MRI) systems worldwide is constantly increasing. It is therefore important to assess and compare the image quality, in terms of detectability, between the PET/MRI and the well-established PET/computed tomography (CT) systems. For this purpose, a PET image quality phantom (Esser) with hot spheres, ranging from 4 to 20 mm in diameter, was prepared with fluorodeoxyglucose and sphere-to-background activity concentrations of 8:1 and 4:1, to mimic clinical conditions. The phantom was scanned on a PET/MRI and a PET/CT system for both concentrations to obtain contrast recovery coefficients (CRCs) and contrast-to-noise ratios (CNRs), for a range of reconstruction settings. The detectability of the spheres was scored by three human observers for both systems and concentrations and all reconstructions. Furthermore, the impact of acquisition time on CNR and observer detectability was investigated.

Results: Reconstructions applying point-spread-function modeling (and time-of-flight for the PET/CT) yielded the highest CRC and CNR in general, and PET/CT demonstrated slightly higher values than PET/MRI for most sphere sizes. CNR was dependent on reconstruction settings and was maximized for 2 iterations, a pixel size of less than 2 mm and a 4 mm Gaussian filter. Acquisition times of 97 s (PET/MRI) and 150 s (PET/CT) resulted in similar total net true counts. For these acquisition times, the smallest detected spheres by the human observers in the 8:1 activity concentration was the 6-mm sphere with PET/MRI (CNR = 5.6) and the 5-mm sphere with PET/CT (CNR = 5.5). With an acquisition time of 180 s, the 5-mm sphere was also detected with PET/MRI (CNR = 5.8). The 8-mm sphere was the smallest detected sphere in the 4:1 activity concentration for both systems.

Conclusion: In this experimental study, similar detectability was found for the PET/MRI and the PET/CT, although for an increased acquisition time for the PET/MRI.

Keywords: PET/CT, PET/MRI, CNR, Detectability

Background

In combination with structural imaging modalities such as computed tomography (CT) or magnetic resonance imaging (MRI), positron emission tomography (PET) is a versatile modality, which can acquire both qualitative and quantitative functional images. The modality plays an increasing role in detection, diagnosis, and staging of

different types of cancer. With technological advances over the recent years, such as time-of-flight (TOF) capability, point spread function (PSF) modeling, better reconstruction algorithms, and improved detector design and materials, PET image quality and resolution have improved substantially, and with it the capability to detect and quantify smaller lesions [1]. The existing international standard for assessing PET image quality, National Electrical Manufacturers Association (NEMA) NU 2-2018 [2], does however not assess uptake volumes below 10 mm in diameter. Current PET systems are more than capable of detecting lesions smaller than this, and it is therefore a need for further evaluation of image quality, in terms of detectability, in current state-of-the-art systems by using uptake volumes below 10 mm in diameter [3–5]. This is especially important not only for the more recently introduced PET/MRI systems, but also for newly introduced digital PET/CT systems, where experimental setups assessing detection limits have not been previously performed. Qualitative evaluation of PET detectability is normally performed by human observers, using predefined scores to assess the detectability, while quantitative approaches most commonly measure the contrast-to-noise ratios (CNRs) [3, 4].

In clinical studies, efforts have been made comparing detection rates (in terms of number of lesions detected) between PET/MRI and PET/CT systems, and human observer studies have demonstrated equivalent detection rates in most types of cancers [6–8]. Exceptions include prostate cancer, bone metastases, and cerebrospinal lesions where PET/MRI might have advantages over PET/CT and small lung lesion detection where PET/CT with diagnostic CT has been reported superior to PET/MRI [6–8]. However, there is limited information regarding PET detection limits in terms of lesion size in the clinical studies. Furthermore, biological factors and attenuation correction issues will bias the results in clinical comparisons, making the interpretations of the results more complex than in experimental studies.

Only a few studies have investigated and optimized detectability in PET/CT systems, for sphere sizes smaller than 10 mm in an experimental setting. Hashimoto et al. [4] assessed the detectability using a NEMA body phantom with sphere diameters of 4 to 37 mm and a sphere-to-background ratio of 8:1 and detected hot spheres down to 6 mm with clinical scan times (2 min). They also found that the detectability index (similar to CNR in this study) and recovery coefficient were increased with TOF and for the smallest voxel size (2 mm), for spheres smaller than 10 mm in diameter. Other studies have also shown that reconstruction advances, such as TOF, PSF, and smaller voxel sizes can be used to improve the detectability [4, 9–21]. Using a Jaszczak phantom, Adler et al. [3] demonstrated that hot spheres down to 4–6 mm could be detected in a range of currently available PET/CT imaging systems employing clinical scan times (2–4 min). For the three clinically available PET/MRI systems, NEMA image quality results have recently been reported by Boellaard et al. [22] but does however not include detectability of small uptake volumes.

The purpose of this study was to experimentally investigate and compare the detectability of small uptake volumes (≥ 4 mm diameter) for the Biograph mMR PET/MRI system and the Biograph mCT PET/CT system, both manufactured by Siemens Healthcare (Erlangen, Germany). A PET image quality phantom (Esser PET phantom) was used for the calculation of contrast recovery coefficient (CRC) and CNR for hot spheres ranging from 4 to 20 mm diameters, for different sphere-

to-background activity concentrations and for a range of different reconstruction settings. This quantitative approach was complemented with a blinded human observer study, where three observers scored the detectability of each sphere in all reconstructed PET images.

Methods

Phantom

The phantom utilized in this study was an Esser PET phantom model PET/FL/P with lid model PET/LID/FL and additional hollow sphere models ECT/HS/SET6 and ECT/MI-HS/SET4 (Fig. 1) (Data Spectrum Corporation, Hillsborough, NC, USA). The phantom has a cylindrical shape with an inner diameter of 20 cm and an inner height of 19 cm, with a cold rod insert and a lid with seven protruding cold contrast cylinders (containing teflon, oil, air, and water) with outer diameters ranging from 8 to 25 mm. These inserts were only used for image registration purposes. Six coplanar hollow spheres with inner diameters of 4, 5, 6, 8, 12, and 20 mm were mounted in the phantom to represent the small uptake volumes of interest for this study.

Data acquisition

The phantom was scanned with two different sphere-to-background activity concentrations (8:1 and 4:1) using fluorodeoxyglucose (^{18}F-FDG) (Table 1). The activity
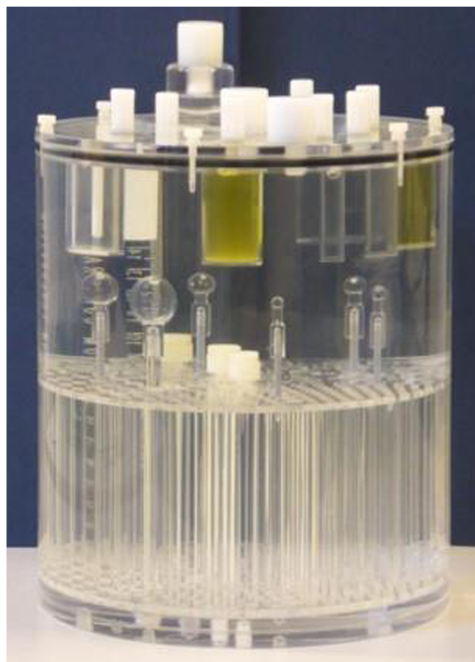
Fig. 1 Esser PET phantom with additional coplanar hot spheres of 4, 5, 6, 8, 12, and 20 mm, attached to the bottom of the phantom

Table 1 Calculated activity concentrations in background ($C_{B,0}$) and in hot spheres ($C_{H,0}$), total activity (A_0) at scan start, and time between scanning (Δt) at the PET/MRI and the PET/CT

| | Sphere to background | | | |
| | 8:1 | | 4:1 | |
	PET/MRI	PET/CT	PET/MRI	PET/CT
$C_{B,0}$ [kBq/mL]	3.5	3.1	3.9	3.4
$C_{H,0}$ [kBq/mL]	28.6	25.1	15.4	13.7
A_0 [MBq]	20.3	17.8	21.9	19.4
Δt [min]	20		19	

concentrations were selected to mimic activity ranges typically found in clinical scans. For each concentration, acquisitions were first performed on the Biograph mMR (version VE11P) (Siemens Healthcare, Erlangen, Germany) followed by acquisitions on the Biograph mCT (version syngo MI.PET/CT 2012A) (Siemens Healthcare, Erlangen, Germany).

The PET/MRI protocol included a Dixon scan (TR 4.14 ms, TE1 1.28 ms, TE2 2.51 ms, field of view (FOV) 265×500 mm^2, flip angle 10°, slice thickness 2.02 mm) and a 10-min (2 times the clinical acquisition time) listmode PET scan acquired in one bed position. The phantom was positioned in the center of the transaxial MRI FOV, in a low-attenuating foam phantom holder. The PET/CT protocol included a CT scan (reference tube current-exposure time product 200 mAs, peak tube voltage 120 kV, slice thickness 3 mm, collimation 64×0.6 mm, rotation time 1 s, pitch 0.9) along with a 5-min (2 times the clinical acquisition time) listmode PET scan acquired in one bed position. The phantom was positioned in the same holder as in the PET/MRI, in the center of the transaxial FOV. The PET/CT scans started 20 min (8:1 activity concentration) and 19 min (4:1 activity concentration) after the PET/MRI scans.

PET detectors

Both the mMR and the mCT detectors consist of lutetium oxyorthosilicate (LSO) crystals of $4 \times 4 \times 20$ mm. The mMR has an axial PET FOV of 25.8 cm, a transaxial FOV of 58.8 cm, and a detector ring diameter of 65.6 cm [23]. The integrated whole-body MR is a 3 Tesla niobium-titanium magnet. The mCT has an axial PET FOV of 22.1 cm and a transaxial FOV of 70 cm, the detector ring diameter is 84.2 cm and a 64-slice CT is integrated [24].

Phantom attenuation correction

For clinical protocols, attenuation correction maps (AC maps) are generated automatically; CT-based AC (CTAC) is based on the bilinear conversion of CT values to attenuation values for the specific photon energy 511 keV, while MR-based AC (MRAC) normally is based on the aforementioned Dixon sequence. The Dixon sequence enables separation of water and fat signal from a human body and allows segmentation of fat, soft-tissue, and air as well as lung tissue. The Dixon-based AC map is generally not suited for AC of phantoms due to the risk of artifacts in MR images at high magnetic field strengths when scanning large water-filled phantoms [22, 25]. For this reason, the CTAC map was also used for AC of PET/MRI data.

This means that uncertainties due to attenuation correction, common in clinical PET/MRI imaging, can be disregarded. To enable CTAC at the PET/MRI, a CTAC map of the phantom was first multiplied with 10,000 to get the same scale as the MRAC maps from the PET/MRI system. Then, the corresponding CTAC image was rigidly registered to the in-phase image from the Dixon sequence, and the CTAC map was transformed with the resulting transformation matrix to match the in-phase image and hence the MRAC map. The multiplication and registrations were performed with the software Aliza 1.38.2 (Aliza Medical Imaging, Bonn, Germany). To enable import of the CTAC maps to the PET/MRI system, the pixel data of the MRAC maps was replaced by the pixel data of the CTAC maps.

Table 2 Evaluated reconstruction settings for the phantom PET scans for both 8:1 and 4:1 activity concentration

System	Reconstruction algorithm	Iterations	Subsets	Matrix [pixels]	Voxel size [mm]	PET acquisition time [s]	Filter
PET/CT	OSEM	1–8	24	400 × 400	2.0 × 2.0 × 2.0	150	4 mm Gauss
	OSEM&PSF						
	OSEM&TOF		21				
	OSEM&TOF&PSF						
		3		128 × 128	6.4 × 6.4 × 2.0		
				200 × 200	4.1 × 4.1 × 2.0		
				256 × 256	3.2 × 3.2 × 2.0		
				512 × 512	1.6 × 1.6 × 2.0		
		1–8		400 × 400	2.0 × 2.0 × 2.0		2 mm Gauss
							No filter
		3				60, 120, 180, 240, 300	4 mm Gauss
PET/ MRI	OSEM	1–8	21	344 × 344	2.1 × 2.1 × 2.0	97	4 mm Gauss
	OSEM&PSF						
		3		128 × 128	5.6 × 5.6 × 2.0		
				172 × 172	4.2 × 4.2 × 2.0		
				256 × 256	2.8 × 2.8 × 2.0		
				512 × 512	1.4 × 1.4 × 2.0		
				344 × 344	2.1 × 2.1 × 2.0		2 mm Gauss
							No filter
						60, 120, 180, 240, 300, 360, 420, 480, 540, 600	4 mm Gauss

PET reconstructions

The PET data was reconstructed with a range of different reconstruction settings (Table 2). 3D iterative reconstruction algorithm was employed (ordered subset expectation maximization (OSEM)), with and without PSF modeling (both systems) as well as with and without TOF (PET/CT). The number of iterations varied from 1 to 8, and the pixel size varied from ~ 1 mm to ~ 6 mm. Furthermore, Gaussian filter of 4 mm and 2 mm was applied, in addition to reconstructions without filter (all-pass). The same number of net true counts was used for a direct comparison between the PET/CT and PET/MRI. PET/CT listmode data was reconstructed for the first 150 s, as this is the typical clinical acquisition time/bed on this system, based on guidelines for PET/CT ^{18}F-FDG examinations [26]. The same net true counts were reached at 97 s with the PET/MRI (due to the higher sensitivity of the PET/MRI system), and this time was therefore used for the direct comparisons between the systems. In order to compare CNR and detectability improvements over time, reconstructions with increasing time frames of 1 min were also performed, from 1 to 5 min for the PET/CT and from 1 to 10 min for PET/MRI. This corresponds to twice the typical acquisition times/bed for each system. On-scanner software for each system was used for the reconstructions, which included CT-based attenuation corrections for all reconstructions, as well as corrections for decay, detector normalization, randoms, and scatter.

Image analysis

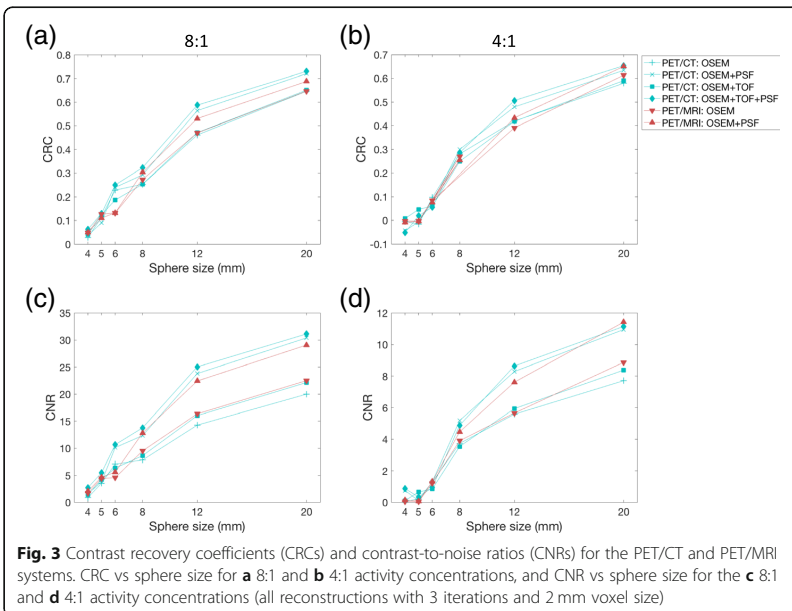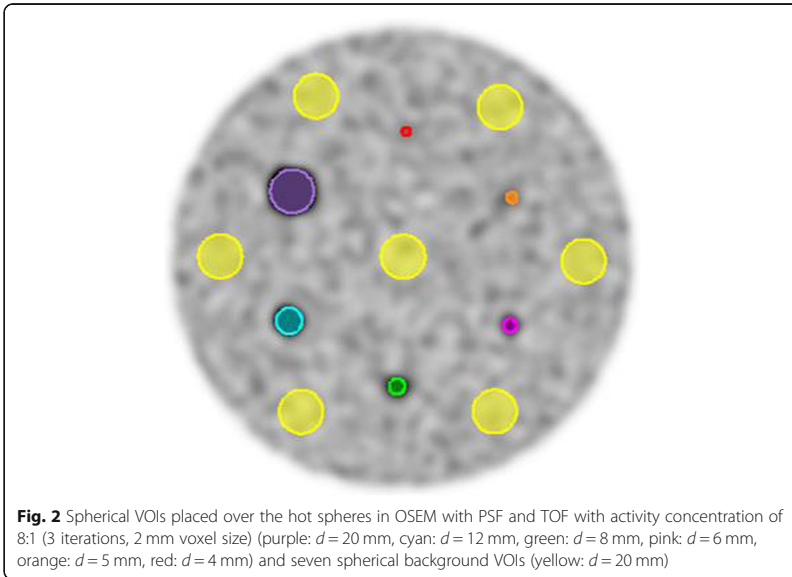#### Prompts, randoms, trues, and scatter fraction

The number of prompts, randoms, and total net trues was extracted from the sinogram headers at each system for the acquisition times that yielded the same number of total net trues, for both activity concentrations. The estimated scatter fraction was extracted from DICOM headers.

CRC and CNR

To perform quantitative analyses, spherical volumes of interest (VOIs) were placed over the hot spheres of the phantom, with the same size as the inner volume of the spheres. In addition, seven spherical background VOIs ($d = 20$ mm) were centered in the same transaxial plane as the hot spheres, one in the central part and six uniformly distributed close to the edge of the phantom (Fig. 2). The VOIs were placed on a CT image and the set of VOIs were manually adjusted to fit the activity in the PET images for each of the four scan sessions (two activity concentrations on two systems) and subsequently copied to all the remaining reconstructions of the same scan session.

CRC and CNR were calculated to quantitatively compare the detectability between the systems, for different reconstruction settings. CRC provides information of how accurately the system reproduces the true activity concentration in a specific volume, but gives little or no information about the visibility of a specific uptake volume, like CNR. CRC was calculated as defined by Kessler et al. [27] and NEMA [2]:

$$\text{CRC} = \frac{\left(C_H / C_B \right) - 1}{\left(a_H / a_B \right) - 1} \tag{1}$$

Fig. 2 Spherical VOIs placed over the hot spheres in OSEM with PSF and TOF with activity concentration of 8:1 (3 iterations, 2 mm voxel size) (purple: $d = 20$ mm, cyan: $d = 12$ mm, green: $d = 8$ mm, pink: $d = 6$ mm, orange: $d = 5$ mm, red: $d = 4$ mm) and seven spherical background VOIs (yellow: $d = 20$ mm)

Fig. 3 Contrast recovery coefficients (CRCs) and contrast-to-noise ratios (CNRs) for the PET/CT and PET/MRI systems. CRC vs sphere size for **a** 8:1 and **b** 4:1 activity concentrations, and CNR vs sphere size for the **c** 8:1 and **d** 4:1 activity concentrations (all reconstructions with 3 iterations and 2 mm voxel size)

where C^{H} is the average counts in the hot sphere VOI, and C^{B} is the average counts of the background VOIs, while a^{H} and a^{B} is the activity concentration in the hot sphere and the background, respectively. While CNR was calculated according to [28]:

$$\text{CNR} = \frac{|C_H - C_B|}{SD_B} \qquad (2)$$

where SD_B is the standard deviation of the counts in the background VOIs.

For the direct comparisons of CRC and CNR for different sphere sizes, the 344×344 matrix size was used for PET/MR images and the 400×400 matrix size for PET/CT images, as this corresponds to approximately the same pixel size. The relationship between CNR and number of iterations, pixel size, and filter was further evaluated for the smallest sphere with CNR > 5 (Rose criterion) on both systems for the acquisitions with similar number of true counts in the 8:1 concentration.

Detectability—human observer study

To qualitatively evaluate the detectability of the hot spheres, three observers (physicists experienced in the field of medical imaging) individually scored the detectability of each hot sphere in all PET reconstructions from both systems. The PET images were presented to the observers in random order, blinded for the reconstruction settings. The detectability of the spheres was scored from 0 to 2, similar to the score system used by Adler et al. [3], where 0 was not detectable, 1 was visible, but comparable to noise, and 2 was clearly visible. The images were evaluated in *syngo*.via (software version VB10/30) (Siemens Healthcare, Erlangen, Germany). A sphere was defined as detected if the sum of the scores from the three observers were 3 or higher, with the restriction that no observer gave a score of 0, and all remaining spheres were defined as non-detected.

CNR and detectability

CNR and detectability improvements with increased acquisition times were evaluated for spheres with CNR < 5 (Rose criterion) on any system in the 8:1 concentration (for the 150 s PET/CT and 97 s PET/MRI reconstructions), in order to evaluate whether spheres with CNR < 5 would improve CNR and become detectable with increasing scan time. Furthermore, the relation between CNR and detectability in the human observer study was also investigated and compared to the Rose criterion, which states that an object is detectable if CNR is above 3–5, depending on characteristics such as object size and shape, edge sharpness, viewing distance, and observer experience [29].

Statistics

To evaluate inter-reader agreement, Kappa statistics were performed (with Stata/MP 15.1, StataCorp LLC, USA). Cohen/Conger's Kappa was used in this study, calculated by the kappaetc package by Daniel Klein, based on formulas in [30]. Weighted kappa was used and the weight was 1 for perfect agreement, 0.5 for a difference in score of one, and 0 for a difference in score of two.

Results

Prompts, randoms, trues, and scatter fraction

The total number of prompts, randoms, and trues and estimated scatter fraction, for acquisition times yielding the same number of total net trues, are demonstrated in Table 3, for both activity concentrations. The number of prompts and randoms, as well as scatter fraction, were higher for the PET/MRI compared to the PET/CT.

CRC and CNR

For most of the largest spheres, PET/MRI and PET/CT yielded similar CRC and CNR for the OSEM-only reconstructions, while a slight increase for PET/CT was seen with the OSEM+PSF reconstructions (Fig. 3). The addition of TOF at the PET/CT did also cause a small increase in CRC and CNR. In the 8:1 concentration, CNR > 5 (Rose criterion) was reached for the 6-mm sphere for both systems, and this sphere was therefore used in the further evaluations of CNR.
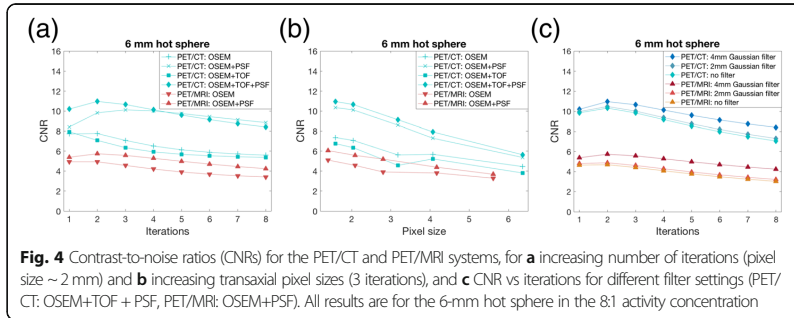
The effect of number of iterations, pixel size, and filter on CNR is shown in Fig. 4. Maximum CNR was reached with two iterations for both imaging systems, with PSF for PET/MRI and for the combination of PSF and TOF for PET/CT (Fig. 4a). For PET/CT, it was seen that reconstructions with PSF only needed more iterations to converge compared to reconstructions with both PSF and TOF. Small pixel sizes (< 2 mm) yielded the highest CNR for both systems (Fig. 4b). A Gaussian filter of 4 mm FWHM resulted in the highest CNR for both systems (Fig. 4c).

Detectability—human observer study

With similar number of true counts for the two systems, the 6-mm sphere was the smallest detected sphere with PET/MRI in the 8:1 activity concentration. The 6-mm sphere was detected in all reconstructions, except for four iterations or more, or a pixel size of 3 mm, in the reconstructions without PSF. The 5-mm sphere was detected with PET/CT in the 8:1 activity concentration (for some reconstructions including TOF, with more than two iterations, and a pixel size below 4 mm), while in the 4:1 activity concentration, the 8 mm sphere was the smallest detected sphere for both systems and in all reconstructions with a few exceptions (PET/MRI: OSEM, 1 iter, 2 mm pixel size; OSEM+PSF, 3 iter, pixel size > 4 mm; PET/CT: OSEM+TOF, 3 iter, 6 mm pixel size). Modifying the filter setting did not yield detection of smaller spheres.

Table 3 The number of prompts, randoms, total net trues, and estimated scatter fraction, for the phantom scans (PET/CT 150 s acquisition, PET/MRI 97 s acquisition), for activity concentrations of 8:1 and 4:1

	Sphere to background			
	8:1		4:1	
	PET/CT	PET/MRI	PET/CT	PET/MRI
Prompts (MCts)	20.9	22.2	22.6	24.2
Randoms (MCts)	1.8	3.1	2.0	3.5
Total net trues (MCts)	19.1	19.2	20.7	20.7
Scatter fraction (%)	30.1	31.1	29.8	30.9

Fig. 4 Contrast-to-noise ratios (CNRs) for the PET/CT and PET/MRI systems, for **a** increasing number of iterations (pixel size ~ 2 mm) and **b** increasing transaxial pixel sizes (3 iterations), and **c** CNR vs iterations for different filter settings (PET/CT: OSEM+TOF + PSF, PET/MRI: OSEM+PSF). All results are for the 6-mm hot sphere in the 8:1 activity concentration
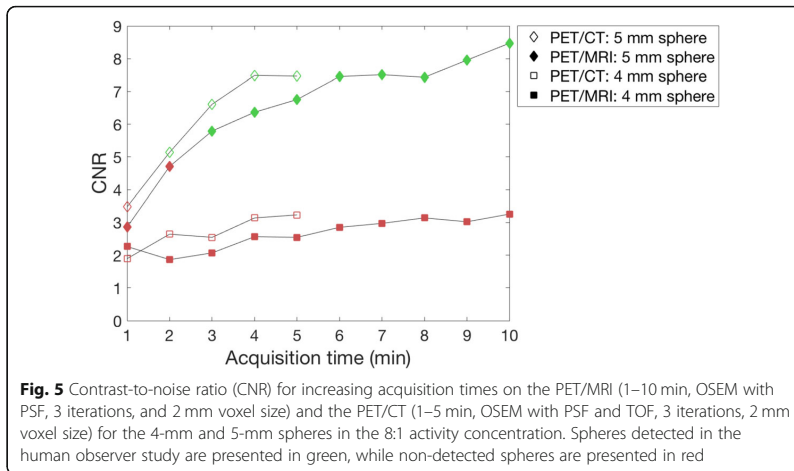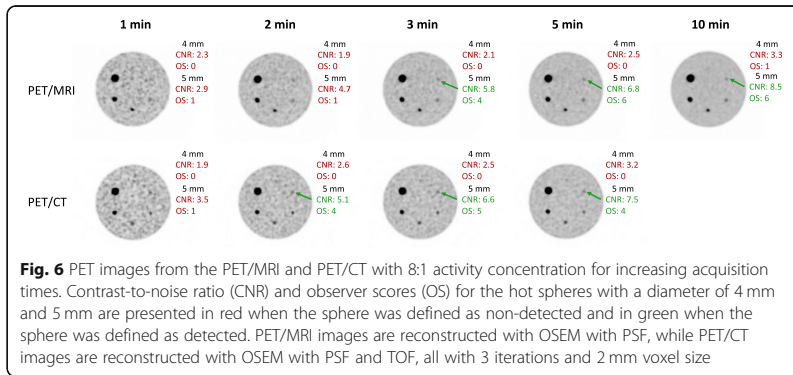
The percentage agreement between the observers for all reconstructions were 0.95% (95% C.I. 0.94–0.96) and Kappa was 0.89 (95% C.I. 0.88–0.91), which correspond to almost perfect agreement according to definitions by Landis et al. [31].

Detectability and CNR

The effect of increased acquisition times on CNR and detectability were evaluated for the 4 and 5 mm spheres, as these spheres had a CNR below 5 on the PET/MRI from the acquisitions with similar number of true counts. The results demonstrated that the 5-mm sphere was the smallest detected sphere for both systems, requiring a 3-min acquisition on the PET/MRI and a 2-min acquisition on the PET/CT (Fig. 5), which is less than the clinical acquisition times used at our hospital. Corresponding PET images for increasing acquisition times are presented in Fig. 6.

The distribution of CNR for detected and non-detected spheres is illustrated in Fig. 7, and the distribution was similar for PET/MRI and PET/CT. CNR was above 3 for all detected spheres, except for the 8-mm sphere in one PET/MRI reconstruction and seven PET/CT reconstructions which yielded CNR between 2.3–3.0. CNR was below 5
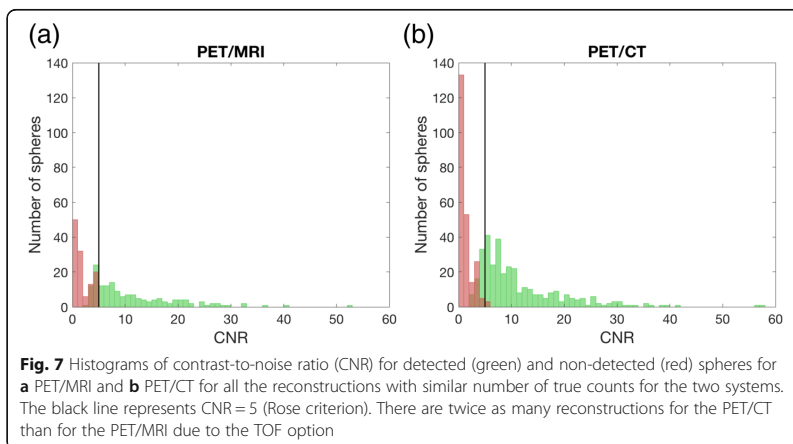

Fig. 5 Contrast-to-noise ratio (CNR) for increasing acquisition times on the PET/MRI (1–10 min, OSEM with PSF, 3 iterations, and 2 mm voxel size) and the PET/CT (1–5 min, OSEM with PSF and TOF, 3 iterations, 2 mm voxel size) for the 4-mm and 5-mm spheres in the 8:1 activity concentration. Spheres detected in the human observer study are presented in green, while non-detected spheres are presented in red

Fig. 6 PET images from the PET/MRI and PET/CT with 8:1 activity concentration for increasing acquisition times. Contrast-to-noise ratio (CNR) and observer scores (OS) for the hot spheres with a diameter of 4 mm and 5 mm are presented in red when the sphere was defined as non-detected and in green when the sphere was defined as detected. PET/MRI images are reconstructed with OSEM with PSF, while PET/CT images are reconstructed with OSEM with PSF and TOF, all with 3 iterations and 2 mm voxel size

for the non-detected spheres, except for the 5-mm sphere which had a CNR of 5.5–5.6 in three PET/CT reconstructions.

Discussion

In this study, the detectability of Siemens PET/MRI and PET/CT systems were evaluated and compared in an experimental setting, both quantitatively and by human observers. Spheres down to 5 mm were considered detected by both systems, for shorter acquisition times than normally used in clinical routine.

In general, the PET/CT showed slightly increased CRC and CNR for the OSEM+PSF(+TOF) reconstructions compared to PET/MRI. CRC and CNR increased when PSF was incorporated in the reconstruction, and a further increase was found when both PSF and TOF were included. Improvements by PSF and TOF have also been demonstrated previously [4, 13, 15–17, 19, 20], and this indicates that these algorithms should be used to increase the possibility of detecting small lesions. PSF is a geometry correction that provides higher and more uniform spatial resolution over the transaxial FOV and will therefore have the most impact at the outer edges of the FOV [32]. The inclusion of TOF increases the signal-to-

Fig. 7 Histograms of contrast-to-noise ratio (CNR) for detected (green) and non-detected (red) spheres for **a** PET/MRI and **b** PET/CT for all the reconstructions with similar number of true counts for the two systems. The black line represents CNR = 5 (Rose criterion). There are twice as many reconstructions for the PET/CT than for the PET/MRI due to the TOF option

noise ratio (SNR) in the image, and the increase is proportional to the size of the imaging object [32]. Thus, PSF and TOF will probably have a larger effect in clinical patient scans than for the phantom in this study, since the Esser phantom has a smaller diameter than a typical patient. The TOF option was only available on the PET/CT system, since the timing resolution of the avalanche photodiode (APD) detectors in the Siemens Biograph PET/MR system is too slow for TOF. It should be noted, however, that PSF may cause edge artifacts (Gibbs artifacts) and should be used with caution in quantitative analysis of sub-centimeter lesions [10, 33].

The number of iterations and post-filtration had a small effect on CNR. The maximum CNR for two iterations corresponds to previous results on image quality for the same systems [16]. More iterations improve the quantitative accuracy of the image but does also increase the background noise [34]. However, new algorithms, such as Bayesian penalized likelihood algorithms, maintain high image quality with more iterations by suppressing noise with a penalty function. The penalty function takes prior knowledge into account and warrants convergence without amplifying noise, resulting in increased activity measures and improved detection of small objects [32, 34–40]. Out of the evaluated filter settings, a Gaussian filter of 4 mm FWHM should be preferred as CNR then was maximized. The choice of pixel size had a larger impact on CNR, especially for the PET/CT. Current guidelines for whole-body ^{18}F-FDG PET recommend pixel sizes of 3.0– 4.0 mm [26]. With new technology and recent developments, modern PET systems allow pixel sizes down to 1 mm, but these are rarely used. Our study shows increased CNR and detectability of small uptake volumes for a decreased pixel size, in accordance with other studies [3, 11, 12, 21, 41]. This, in addition to the use of a 10-mm sphere as the smallest sphere in the NEMA standard for assessing PET quality, implies that there is a need for upgrading current PET imaging guidelines and standardized imaging quality phantoms to meet the performance of modern PET systems.

The human observer study revealed lower detection limits in PET/CT images (5 mm) compared to PET/MRI images (6 mm) for the 8:1 activity concentration for acquisitions with similar number of true counts, while the same detection limit of 8 mm was found for both systems for the 4:1 activity concentration. For an increased acquisition time on the PET/MRI, the detectability was however comparable between the systems, indicating that longer scan times are required on the Siemens PET/MRI to obtain the same detectability as the Siemens PET/CT. In clinical PET/MR imaging, the acquisition times should probably be exceeded even further, since more factors will influence image quality and detectability, such as the slightly increased scatter fraction of PET/MRI that will be further increased for a patient that is larger than the phantom, increased attenuation as the patient's arms are positioned alongside the body, and smaller bed overlap in multi-bed scans on PET/MRI compared to PET/CT.

As TOF slightly increased CRC and CNR, it was also required to detect the 5 mm sphere in the human observer study. Despite quantitative improvements also with the use of PSF, the detectability was in general not improved with PSF in the observer study. The use of a relatively large filter, such as the 4 mm Gaussian filter, could explain why the 4-mm sphere was not detected. However, the sphere was not detected with a 2-mm Gaussian filter or when the filter was omitted.

There are several factors that limit the spatial resolution in PET, but one of the main limitations is the size of the detector element (crystal) [42]. Other factors include positron range and acollinearity factors (which cannot be reduced), decoding errors, crystal penetration, and reconstruction algorithm. Both the PET/MRI and PET/CT systems have lutetium oxyorthosilicate (LSO) crystals with a dimension of $4 \times 4 \times 20$ mm. The theoretical spatial resolution can be estimated for a given system [42], and with the effective positron range for ^{18}F in water [43], this yields 4.5 and 4.7 mm full width at half maximum (FWHM) in isocenter for the PET/MRI and PET/CT, respectively. The detection limits found in this study therefore seem to approach the actual spatial resolution limits of the systems, also for clinical scan times.

The correlation between the detectability in the human observer study and CNR showed a similar distribution for PET/MRI and PET/CT, and most of the detected spheres had a CNR above 3 and most of the non-detected spheres had a CNR below 5, which is in concordance with the Rose criterion. These results indicate that the scoring system utilized in this study seems functional for this type of experimental setting. Adler et al. [3] used a more conservative limit for detected spheres (score = 5), which also agreed with the Rose criterion. However, they defined some spheres as "neither observed nor not observed" and excluded these spheres from the analysis, which might have influenced the result. The Rose criterion will change with the sphere size and matrix size, but was not adjusted for in this study.

Several technical factors influence the quantitative measurements in clinical PET/MRI data, but could be neglected in this study by using a phantom with CT-based AC for both systems. For clinical scans at the Siemens PET/MRI system, AC is based on segmentation of tissue, providing predefined attenuation coefficients for soft tissue, fat, lung tissue, and air, and bone is included by co-registration with a bone atlas. This can cause quantification and registrations errors, influencing the PET images [44, 45]. In addition, the flexible body surface coils are not accounted for in clinical AC PET images and may lead to a regionally dependent bias [46]. Furthermore, respiratory motion can lead to PET image blurring, artifacts, and tracer uptake quantification errors in general [47], but this affects both PET/MRI and PET/CT data, and motion correction methods are improving [47–50]. A review study by Spick et al. [6] summarized 46 studies (including 2340 patients) and found that the PET/MRI and PET/CT provide comparable diagnostic information for most types of cancer despite both technical and operational issues.

The results of this study are not directly transferable to clinical practice due to the use of a phantom with spheres in fixed positions; hence, the observers know where to look for the spheres. Furthermore, the observers were physicists and not physicians, but the kappa statistics showed almost perfect agreement between the readers. A total score of 3 was considered detected in this study, since we wanted to investigate detectability, and not if the spheres were clearly visible.

Another limitation of this study is the size of the Esser phantom, which is more representative for brain imaging, than for whole body imaging. More noise would have been present with a larger phantom, which for instance could have increased the benefit of PSF and TOF. Furthermore, the limited number of sphere sizes utilized in this study could have an impact on the results, as lower detection limits could have been obtained for the 4:1 activity concentration with a 7-mm sphere size. Another limitation

Øen *et al. EJNMMI Physics*   (2019) 6:16

Page 14 of 16

is that only one scan per activity concentration was analyzed for each system. To reduce the possible statistical errors this could have caused, the mean values of the activity in the hot spheres were used in the analyses.

Conclusion

Similar detectability performance was found for PET/CT and PET/MRI, although for an increased acquisition time on the PET/MRI. Hot spheres as small as 5 mm were detected with a 2-min PET/CT acquisition and a 3-min PET/MRI acquisition, corresponding to a CNR of 5.1 and 5.8, respectively. Reconstruction improvements, such as TOF and/or PSF, should be used to increase the possibility of detecting small lesions. Furthermore, smaller pixel sizes than recommended by current guidelines should be considered for oncological ^{18}F-FDG scans.

Author details
^{1}Department of Circulation and Medical Imaging, Norwegian University of Science and Technology, Postbox 8905, N-7491 Trondheim, Norway. ^{2}Department of Radiology and Nuclear Medicine, St. Olavs University Hospital, Olav Kyrres gt 17, N-7006 Trondheim, Norway.

References
1. Vandenberghe S, Mikhaylova E, D'Hoe E, Mollet P, Karp JS. Recent developments in time-of-flight PET. EJNMMI Phys. 2016;3(1):3.
2. National Electrical Manufacturers Association. Performance measurements of positron emission tomographs (PET) NEMA standards publication NU 2–2018. 2018.
3. Adler S, Seidel J, Choyke P, Knopp MV, Binzel K, Zhang J, et al. Minimum lesion detectability as a measure of PET system performance. EJNMMI physics. 2017;4(1):13.
4. Hashimoto N, Morita K, Tsutsui Y, Himuro K, Baba S, Sasaki M. Time-of-flight information improved the detectability of subcentimeter spheres using a clinical PET/CT scanner. J Nucl Med Technol. 2018;46(3):268–73.
5. Erdi YE. Limits of tumor detectability in nuclear medicine and PET. Mol Imaging Radionucl Ther. 2012;21(1):23–8.
6. Spick C, Herrmann K, Czernin J. 18F-FDG PET/CT and PET/MRI perform equally well in cancer: evidence from studies on more than 2,300 patients. J Nucl Med. 2016;57(3):420–30.
7. Rauscher I, Eiber M, Furst S, Souvatzoglou M, Nekolla SG, Ziegler SI, et al. PET/MR imaging in the detection and characterization of pulmonary lesions: technical and diagnostic evaluation in comparison to PET/CT. J Nucl Med. 2014;55(5):724–9.

8. Sawicki LM, Grueneisen J, Buchbender C, Schaarschmidt BM, Gomez B, Ruhlmann V, et al. Comparative performance of F-18-FDG PET/MRI and F-18-FDG PET/CT in detection and characterization of pulmonary lesions in 121 oncologic patients. J Nucl Med. 2016;57(4):582–6.

9. Surti S. Update on time-of-flight PET imaging. J Nucl Med. 2015;56(1):98–105.

10. Munk OL, Tolbod LP, Hansen SB, Bogsrud TV. Point-spread function reconstructed PET images of sub-centimeter lesions are not quantitative. EJNMMI Phys. 2017;4(1):5.

11. Koopman D, van Dalen JA, Lagerweij MC, Arkies H, de Boer J, Oostdijk AH, et al. Improving the detection of small lesions using a state-of-the-art time-of-flight PET/CT system and small-voxel reconstructions. J Nucl Med Technol. 2015;43(1):21–7.

12. Morey AM, Noo F, Kadrmas DJ. Effect of using 2mm voxels on observer performance for PET lesion detection. IEEE Trans Nucl Sci. 2016;63(3):1359–66.

13. Akamatsu G, Ishikawa K, Mitsumoto K, Taniguchi T, Ohya N, Baba S, et al. Improvement in PET/CT image quality with a combination of point-spread function and time-of-flight in relation to reconstruction parameters. J Nucl Med. 2012;53(11):1716–22.

14. Bal H, Guerin L, Casey ME, Conti M, Eriksson L, Michel C, et al. Improving PET spatial resolution and detectability for prostate cancer imaging. Phys Med Biol. 2014;59(15):4411–26.

15. Jakoby BW, Bercier Y, Conti M, Casey ME, Bendriem B, Townsend DW. Physical and clinical performance of the mCT time-of-flight PET/CT scanner. Phys Med Biol. 2011;56(8):2375–89.

16. Karlberg AM, Saether O, Eikenes L, Goa PE. Quantitative comparison of PET performance-Siemens Biograph mCT and mMR. EJNMMI Phys. 2016;3(1):5.

17. Lois C, Jakoby BW, Long MJ, Hubner KF, Barker DW, Casey ME, et al. An assessment of the impact of incorporating time-of-flight information into clinical PET/CT imaging. J Nucl Med. 2010;51(2):237–45.

18. Mehranian A, Zaidi H. Impact of time-of-flight PET on quantification errors in MR imaging-based attenuation correction. J Nucl Med. 2015;56(4):635–41.

19. Petibon Y, Huang C, Ouyang J, Reese TG, Li Q, Syrkina A, et al. Relative role of motion and PSF compensation in whole-body oncologic PET-MR imaging. Med Phys. 2014;41(4):042503.

20. Shang K, Cui B, Ma J, Shuai D, Liang Z, Jansen F, et al. Clinical evaluation of whole-body oncologic PET with time-of-flight and point-spread function for the hybrid PET/MR system. Eur J Radiol. 2017;93:70–5.

21. Thoen H, Keereman V, Mollet P, Van Holen R, Vandenberghe S. Influence of detector pixel size, TOF resolution and DOI on image quality in MR-compatible whole-body PET. Phys Med Biol. 2013;58(18):6459–79.

22. Boellaard R, Rausch I, Beyer T, Delso G, Yaqub M, Quick HH, et al. Quality control for quantitative multicenter whole-body PET/MR studies: a NEMA image quality phantom study with three current PET/MR systems. Med Phys. 2015;42(10):5961–9.

23. Siemens Healthcare GmbH, Biograph mMR Datasheet based on syngo MR E11P. 2017.

24. Siemens Healthcare, Biograph mCT system specifications. 2014.

25. Ziegler S, Braun H, Ritt P, Hocke C, Kuwert T, Quick HH. Systematic evaluation of phantom fluids for simultaneous PET/MR hybrid imaging. J Nucl Med. 2013;54(8):1464–71.

26. Boellaard R, Delgado-Bolton R, Oyen WJ, Giammarile F, Tatsch K, Eschner W, et al. FDG PET/CT: EANM procedure guidelines for tumour imaging: version 2.0. Eur J Nucl Med Mol Imaging. 2015;42(2):328–54.

27. Kessler RM, Ellis JR Jr, Eden M. Analysis of emission tomographic scan data: limitations imposed by resolution and background. J Comput Assist Tomogr. 1984;8(3):514–22.

28. Cherry SR, Sorenson JA, Phelps ME. Chapter 15 - Image Quality in Nuclear Medicine. In: Cherry SR, Sorenson JA, Phelps ME, editors. Physics in nuclear medicine. 4th ed. Philadelphia: W.B. Saunders; 2012. p. 233–51.

29. Rose A. The Visual Process. In: Vision: human and electronic. Boston: Springer US; 1973. p. 1-27.

30. Gwet KL. Handbook of inter-rater reliability: the definitive guide to measuring the extent of agreement among raters. 3rd ed. ed. Gaithersburg, MD: Advanced Analytics, LLC; 2012.

31. Landis JR, Koch GG. The measurement of observer agreement for categorical data. Biometrics. 1977;33(1):159–74.

32. van der Vos CS, Koopman D, Rijnsdorp S, Arends AJ, Boellaard R, van Dalen JA, et al. Quantification, improvement, and harmonization of small lesion detection with state-of-the-art PET. Eur J Nucl Med Mol Imaging. 2017;44(Suppl 1):4–16.

33. Tsutsui Y, Awamoto S, Himuro K, Umezu Y, Baba S, Sasaki M. Edge artifacts in point spread function-based PET reconstruction in relation to object size and reconstruction parameters. Asia Oceania J Nucl Med Biol. 2017;5(2):134–43.

34. Johnson GB, Peller PJ, Kemp BJ, Ryu JH. Future of thoracic PET scanning. Chest. 2015;147(1):25–30.

35. Howard BA, Morgan R, Thorpe MP, Turkington TG, Oldan J, James OG, et al. Comparison of Bayesian penalized likelihood reconstruction versus OS-EM for characterization of small pulmonary nodules in oncologic PET/CT. Ann Nucl Med. 2017;31(8):623–8.

36. Messerli M, Stolzmann P, Egger-Sigg M, Trinckauf J, D'Aguanno S, Burger IA, et al. Impact of a Bayesian penalized likelihood reconstruction algorithm on image quality in novel digital PET/CT: clinical implications for the assessment of lung tumors. EJNMMI Phys. 2018;5(1):27.

37. Parvizi N, Franklin JM, McGowan DR, Teoh EJ, Bradley KM, Gleeson FV. Does a novel penalized likelihood reconstruction of 18F-FDG PET-CT improve signal-to-background in colorectal liver metastases? Eur J Radiol. 2015;84(10):1873–8.

38. Teoh EJ, McGowan DR, Macpherson RE, Bradley KM, Gleeson FV. Phantom and clinical evaluation of the Bayesian penalized likelihood reconstruction algorithm Q. clear on an LYSO PET/CT system. J Nucl Med. 2015;56(9):1447–52.

39. Vallot D, Caselles O, Chaltiel L, Fernandez A, Gabiache E, Dierickx L, et al. A clinical evaluation of the impact of the Bayesian penalized likelihood reconstruction algorithm on PET FDG metrics. Nucl Med Commun. 2017;38(11):979–84.

40. Lindstrom E, Sundin A, Trampal C, Lindsjo L, Ilan E, Danfors T, et al. Evaluation of penalized-likelihood estimation reconstruction on a digital time-of-flight PET/CT scanner for (18) F-FDG whole-body examinations. J Nucl Med. 2018;59(7):1152–8.

41. Li CY, Klohr S, Sadick H, Weiss C, Hoermann K, Schoenberg SO, et al. Effect of time-of-flight technique on the diagnostic performance of 18F-FDG PET/CT for assessment of lymph node metastases in head and neck squamous cell carcinoma. J Nucl Med Technol. 2014;42(3):181–7.

42. Moses WW. Fundamental limits of spatial resolution in PET. Nucl Inst Methods Phys Res A. 2011;648(Supplement 1):S236–S40.

43. Saha GB. Basics of PET imaging: physics, chemistry, and regulations: Springer International Publishing Switzerland; 2015.

44. Paulus DH, Quick HH, Geppert C, Fenchel M, Zhan Y, Hermosillo G, et al. Whole-body PET/MR imaging: quantitative evaluation of a novel model-based MR attenuation correction method including bone. J Nucl Med. 2015;56(7):1061–6.

Øen *et al. EJNMMI Physics*   (2019) 6:16

Page 16 of 16

45. Elschot M, Selnaes KM, Johansen H, Kruger-Stokke B, Bertilsson H, Bathen TF. The effect of including bone in DIXON-based attenuation correction for (18) F-fluciclovine PET/MRI of prostate cancer. J Nucl Med. 2018;59(12):1913–7.
46. Paulus DH, Braun H, Aklan B, Quick HH. Simultaneous PET/MR imaging: MR-based attenuation correction of local radiofrequency surface coils. Med Phys. 2012;39(7):4306–15.
47. Manber R, Thielemans K, Hutton BF, Wan S, McClelland J, Barnes A, et al. Joint PET-MR respiratory motion models for clinical PET motion correction. Phys Med Biol. 2016;61(17):6515–30.
48. Grootjans W, de Geus-Oei LF, Meeuwis AP, van der Vos CS, Gotthardt M, Oyen WJ, et al. Amplitude-based optimal respiratory gating in positron emission tomography in patients with primary lung cancer. Eur Radiol. 2014;24(12):3242–50.
49. Minamimoto R, Mitsumoto T, Miyata Y, Sunaoka F, Morooka M, Okasaki M, et al. Evaluation of a new motion correction algorithm in PET/CT: combining the entire acquired PET data to create a single three-dimensional motion-corrected PET/CT image. Nucl Med Commun. 2016;37(2):162–70.
50. van Elmpt W, Hamill J, Jones J, De Ruysscher D, Lambin P, Ollers M. Optimal gating compared to 3D and 4D PET reconstruction for characterization of lung tumours. Eur J Nucl Med Mol Imaging. 2011;38(5):843–55.

Publisher's Note

Paper III

This paper is awaiting publication and is not included in NTNU Open

NTNU
Norwegian University of
Science and Technology